Government of **Western Australia**
Department of **Mines and Petroleum**

RECORD 2016/5

MICROSTRUCTURAL EVOLUTION OF THE YALGOO DOME (WESTERN AUSTRALIA)

by
M Schiller

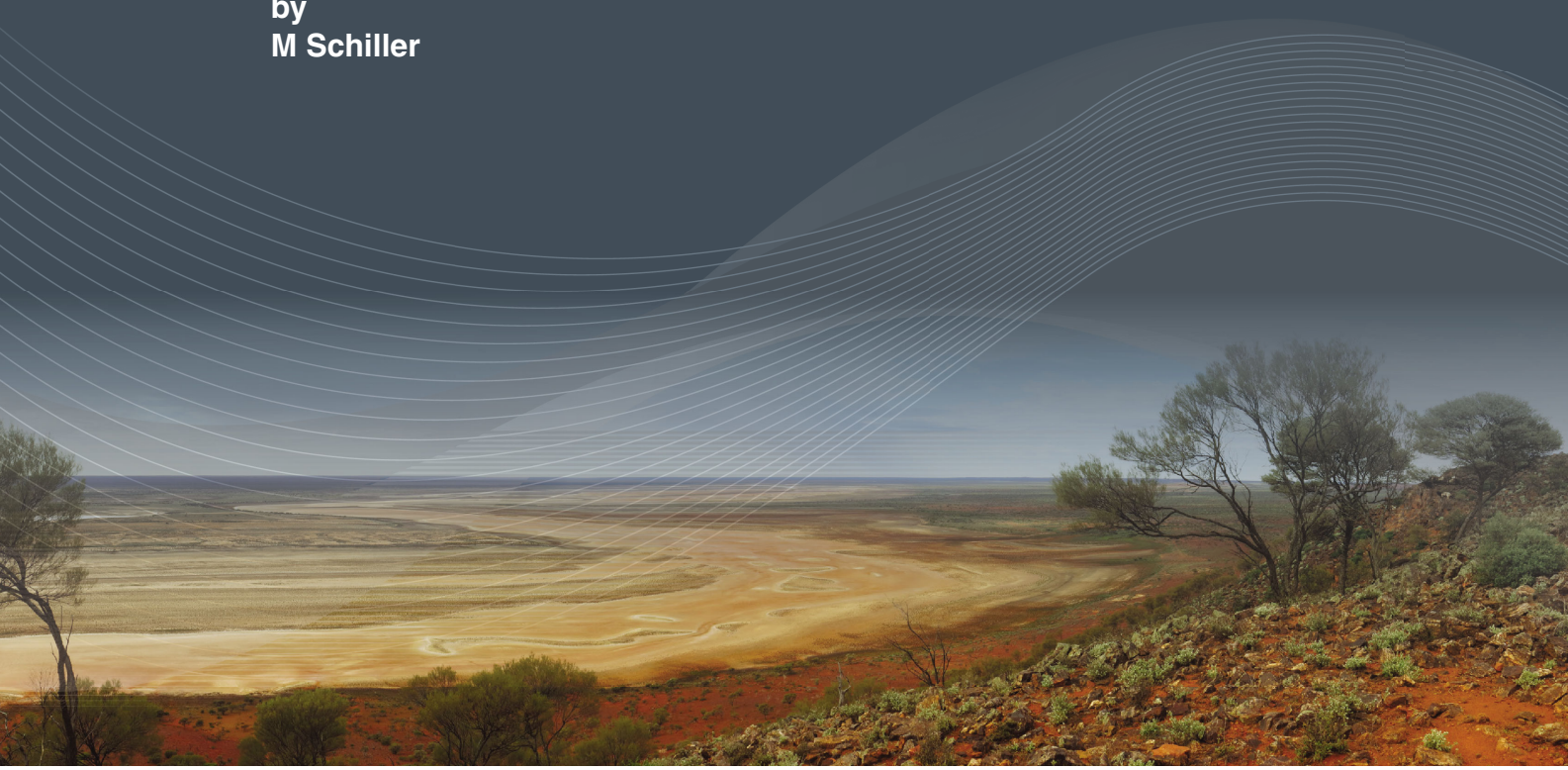

Geological Survey of Western Australia

JOHANNES GUTENBERG UNIVERSITÄT MAINZ

Government of **Western Australia**
Department of **Mines and Petroleum**

Record 2016/5

MICROSTRUCTURAL EVOLUTION OF THE YALGOO DOME (WESTERN AUSTRALIA)

by
M Schiller

Perth 2016

Geological Survey of Western Australia

MINISTER FOR MINES AND PETROLEUM
Hon. Bill Marmion MLA

DIRECTOR GENERAL, DEPARTMENT OF MINES AND PETROLEUM
Richard Sellers

EXECUTIVE DIRECTOR, GEOLOGICAL SURVEY OF WESTERN AUSTRALIA
Rick Rogerson

REFERENCE
The recommended reference for this publication is:
Schiller, M 2016, Microstructural evolution of the Yalgoo Dome (Western Australia): Geological Survey of Western Australia, Record 2016/5, 87p.

National Library of Australia Card Number and ISBN 978-1-74168-673-9

About this publication
This Record is a Bachelor thesis researched, written and compiled as part of an ongoing collaborative project between the Geological Survey of Western Australia (GSWA) and Johannes Gutenberg University, Mainz. Although GSWA has provided field support for this project, the scientific content of the Record, and the drafting of figures, was the responsibility of the author. No editing has been undertaken by GSWA.

Published 2016 by Geological Survey of Western Australia
This Record is published in digital format (PDF) and is available online at <www.dmp.wa.gov.au/GSWApublications>.

Further details of geological products and maps produced by the Geological Survey of Western Australia are available from:
Information Centre
Department of Mines and Petroleum
100 Plain Street
EAST PERTH WESTERN AUSTRALIA 6004
Telephone: +61 8 9222 3459 Facsimile: +61 8 9222 3444
www.dmp.wa.gov.au/GSWApublications

Cover image: Elongate salt lake on the Yilgarn Craton — part of the Moore–Monger paleovalley — here viewed from the top of Wownaminya Hill, 20 km southeast of Yalgoo, Murchison Goldfields. Photograph taken by I Zibra for the Geological Survey of Western Australia

Johannes Gutenberg-Universität Mainz

Faculty 09: Chemistry, Pharmacy and Geosciences

Institute for Geosciences

B. Sc.

BACHELOR THESIS

Microstructural evolution of the Yalgoo Dome (Western Australia)

Presented by: Mona Schiller

Matr. Nr. 2681003

Email: mschille@students-uni-mainz.de

1st Supervisor: Dr. Mark Peternell (JGU Mainz)

2nd Supervisor: Prof. Dr. Cees W. Passchier (JGU Mainz)

Submission Date: 18th January 2016

Abstract

This thesis deals with the microstructural evolution of the Yalgoo Dome, which is a roundish archaic structure in the Murchison Domain of the Yilgarn Craton (Western Australia) and consists of a marginal greenstone belt, a monzogranite mantle and a tonalite core. Thus, it forms a granite-greenstone-complex typically found in Archean cratons and which might be a key for understanding Precambrian tectonics. Established theories about the Yalgoo Dome development and similar structures comprise fold interference and diapirism (Geological Survey of Western Australia; Myers & Watkins, 1985; Foley, 1997; Van Kranendonk et al., 2004; Fenwick, 2014). For the microstructural analysis, samples were collected from mainly granitoid gneisses of different sites of the dome. Subsequently, microstructures were analyzed with a polarization microscope, c-axes orientations were determined with the Fabric Analyser, and a Grain-Size-Analysis was done for eight representative thin sections. Finally, ranges for temperature and strain intensity were estimated due to the grade of dynamic recrystallization, grain shape and grain size. Results reveal a margin-center trend with higher temperatures and lower strain rates in the dome center, combined with slightly lower temperatures and higher strain rates at marginal sites. Nevertheless, the peak metamorphic temperature conditions of all samples are high (400-800°C), and combined with dominating dome-up/greenstone-down shear sense, high-temperature vertical tectonics are suggested. Diapirism of less dense felsic crust and sagduction of denser greenstones would cause such a thermal anomaly (Thébaud & Rey, 2013) and hence this interaction is the most probable explanation for these results. However, crystallographic preferred orientations mainly show Z-maxima (greenschist facies), although X-maxima (upper amphibolite to granulite facies) would be expected in such a setting, underlining that mechanisms like strain partitioning and a younger low-temperature deformation overprint, such as folding, should be considered.

German Abstract

Diese Bachelorarbeit befasst sich mit der mikrostruktuellen Entwicklung des Yalgoo Domes, eine rundliche, archaische Struktur in der Murchison Domain des Yilgarn Kratons (Westaustralien). Sie besteht aus einem Tonalit-Kernbereich, umgeben von Monzogranit und wird im Randbereich begrenzt durch einen Greenstone-Gürtel. Damit repräsentiert es einen für archaische Kratone typischen Granit-Greenstone-Komplex, dessen Entstehungsgeschichte vielleicht ein Schlüssel für das Verständnis Präkambrischer Tektonik ist. Bereits bestehende Theorien zur Entstehung des Yalgoo Domes und ähnlicher Strukturen umfassen Falteninterferenz und Diapirismus (Geological Survey of Western Australia; Myers & Watkins, 1985; Foley, 1997; Van Kranendonk et al., 2004; Fenwick, 2014). Für die Analyse der Mikrostrukturen wurden vor allem Proben von granitoiden Gneissen an verschiedenen Stellen des Domes genommen. Anschließend wurden die Mikrostruturen mittels eines Polarisationsmikroskops analysiert, die Orientierung der c-Achsen wurde mit einem Fabric Analyser bestimmt, und für acht repräsentative Dünnschliffe wurde eine Korngrößenanalyse gemacht. Anhand dieser Daten wurden schließlich der Temperaturbereich und die Deformationsrate abgeschätzt. Die Ergebnisse zeigen, dass Kernbereiche des Yalgoo Domes unter höheren Temperaturen und niedrigeren Verformungsraten deformiert wurden als Randbereiche, deren Proben etwas niedrigere Temperaturen und höhere Verformungsraten anzeigen. Nichtsdestotrotz waren die Temperaturen für alle Gesteine des Domes während der Metamorphose hoch (400-800°C), was zusammen mit dominierendem Dome-aufwärts/Greenstone-abwärts-Schersinn darauf hindeutet, dass hoch-Temperatur-Tektonik in vertikaler Richtung den Yalgoo Dome formte. Diese thermische Anomalie und vertikale Tektonik wären durch eine Kombination aus Diapirismus granitischer Kruste mit geringerer Dichte und Absenkung dichterer Greenstone-Lagen, entstehen (Thébaud & Rey, 2013). Allerdings zeigen die kristallographischen Orientierungen Z-Maxima(Grünschiefer-Fazies) in einem Stereonetz an, obwohl in diesem geologischen Kontext X-Maxima (Amphibo-Granulit-Fazies) zu erwarten wären. Dies weist darauf hin, dass neben Prozessen wie Strain Partitioning auch eine jüngere niedrig-Temperatur-Deformation, wie zum Beispiel Faltung, bedacht werden sollten.

Table of Contents

1 Introduction 1

1.1 Archean Tectonics & Crustal Evolution 1

1.2 Regional Geology of the Yilgarn Craton, Western Australia 3

2 Methodology 6

2.1 Microstructures in thin sections 6

2.1.1 Internal deformation without recrystallization 6

2.1.2 Dynamic Recrystallization & Recovery – a function of temperature 8

2.2 Grain-Size-Analysis 13

2.2.1 Digitalization of grains with ArcGIS 13

2.2.2 Analysis with Matlab (polyLX) 14

2.3 Crystallographic preferred orientation data 19

2.3.1 The Fabric Analyser techniques 19

2.3.2 CPO data analysis 22

2.3.3 Interpretation of CPO plots 23

3 Results 26

3.1 Microscope Observations & Field Data 26

3.2 Grain Size Analysis 37

3.3 Crystallographic Preferred Orientation (CPO) 48

4 Discussion 52

4.1 Interpretation of microstructures and field data 52

4.2 Interpretation of the Grain-Size-Analysis 53

4.3 Interpretation of Crystallographic Preferred Orientations 56

4.4 Theory for the Yalgoo Dome evolution 59

5 Conclusions 62

Acknowledgment 63

Bibliography 63

Appendix 70

1 Introduction

This thesis is focused on the 30 x 90 km large archaic Yalgoo Dome located about 400 km north-easterly of Perth in Western Australia. This structure is situated in the Murchison Domain, which is part of the Youanmi Terrane of the Yilgarn Craton and consists of a 2.96 Ga migmatic tonalite core surrounded by 2.65 Ga monzogranite and 2.95 Ga greenstones at the outer margin (Fig. 1). (Geological Survey of Western Australia; Fenwick, 2014).

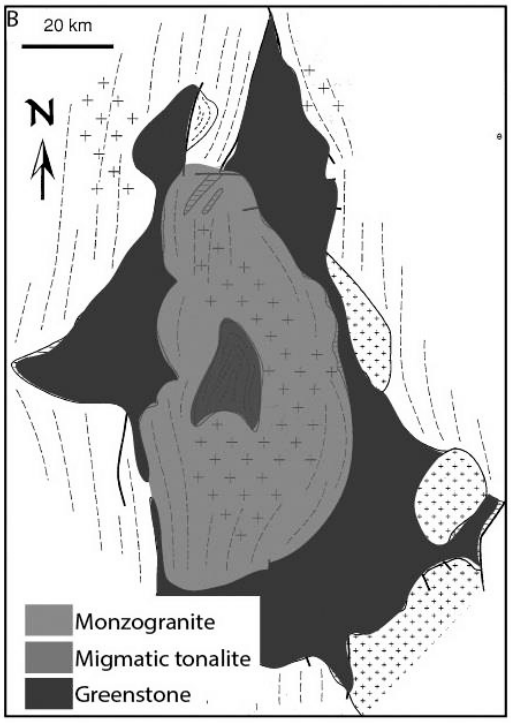

Fig. 1: Different geological entities of the Yalgoo Dome (modified after Watkins & Hickman, 1990 (Fenwick, 2014)).

1.1 Archean Tectonics & Crustal Evolution

At present, many unknown details remain about the formation of the proto-crust and its characteristics concerning geodynamic behavior. Relicts of archaic crust, preserved as large cratons, are part of all continents. Throughout time, many small terranes and cratonic nuclei have been sutured to larger cratons, then continents and supercontinents (Johnson, 2013).

Basic characteristics such as temperature and chemical composition of the earth's early mantle and crust are important to understand the ancient geodynamics. The mantle potential temperature T_p was about 150-250 °C hotter in the Archean compared to present time; also the MgO content of primary magmas was much higher. Intensive melting of dry ambient mantle-peridotite, via combined decompression and mantle plumes, produced mafic oceanic crust of nearly 25-35 km thickness. Continuing rigorous magma production has led to dry, Mg-rich and thickened volcanic plateaus (Korenaga, 2008; Herzberg et al., 2010). The high T_p decreased throughout time by increasing secular cooling, caused by surface heat loss exceeding internal heating. The internal heat production might have been an important factor controlling ancient geodynamics (Korenaga, 2006). It is still discussed, if the mantle was homogeneously hotter and convected more inertial (Korenaga, 2008; Herzberg et al., 2010), or if it contained very hot material upwelling from the lower mantle and moderate-T areas in the upper mantle (Kamber, 2015). The latter would probably induce intensive mantle plume activity, which is assumed to contribute to the evolution of the Yilgarn Craton, as described further below.

Continental crust formation has started around 4.4 Ga at the latest and hence before the Archean, as evident from detrital zircons (Wilde et al., 2001). It is not clear how the first formation of felsic crust has been initiated and thus, which processes generated the rocks outcropped in the Yalgoo Dome area. In this context, two main mechanisms should be considered: drip tectonics and proto-subduction.

Drip tectonics

Independently of the water-content of a thickened and thus negatively buoyant crust, the base would gravitationally destabilize at T_p greater than 1500 °C, which is assumed for archaic mantle, and drip down. This process would induce an upwelling mantle-flow responsible for magma production from Mg-rich mantle and oceanic crust, which possibly generates Mg-poor crust via fractionation mechanisms (Johnson et al., 2014). This Mg-depleted crust is the foundation of tonalite-trondhjemite-granodiorite (TTG) formation representing typical rocks found in archaic crust (Moyen & Martin, 2012). Throughout time, drip-tectonics of the crustal basis led to an intense recycling and internal differentiation of the initial lower crust, as well as the formation of more felsic crust on top of oceanic plateaus (Johnson et al., 2014).

Proto-Subduction

The progressing hydration of the mantle and crust could be connected with deep ocean basins and proto-subduction (Korenaga, 2013). Also trace-element-analysis of archaic continental crust suggests arc-forming-processes associated with convergent plate boundaries (Kusky & Polat, 1998). Furthermore, initial felsic material must have derived from mafic material and the subduction process would be able to produce these voluminous granites (Champion & Sheraton, 1997). Present-day-subduction leads to the melting of the mantle wedge based on the liquid input originated from a subducted slab. However, mantle wedge melting was not involved in archaic subduction regimes, which could be explained by a thickened oceanic lithosphere causing a very shallow dip of the subducted slab (Roberts et al., 2015 and references therein). In the Archean, dehydration melting of a warm basic slab probably produced felsic Na-rich and Mg-poor granitoids with a composition similar to those of TTG's (Martin, 1986; Arculus & Ruff, 1990). The migration of the melt-producing location from the subducted slab to the mantle wedge might be a consequence of a progressive earth-cooling (Martin, 1986).

The two ideas of drip tectonics and proto-subduction forming continental crust complement one another (Van Kranendonk et al., 2015). According to Korenaga (2008) the episodes of global isochronic orogenic events can be related to variations of plate velocity. Stein &

Hofmann (1994) emphasize that episodic mantle-plume activities would well explain the global phases of orogeny, komatiite-tholeiite-volcanic sequences and crustal growth.

Granite-Gneiss-Complexes and Greenstone Belts are typical structures found in archaic cratons and might be a key to the understanding of Precambrian tectonics. Dense greenstones of sedimentary and volcanic origin overlying less dense granitoid crust, would cause a density inversion. The felsic crust would rise via solid-state diapirism, which is controlled by the parameters density, thickness and viscosity of both layers. High heat flow at deeper crustal levels and load of mafic volcanic rocks destabilize the felsic crust (Gee, 1979 and references therein). Simultaneously, sagduction processes should be considered: the dense greenstones would subside due to gravity mechanisms displacing the granitoid crust (Fig. 2). This combined advection into basins and domes leads to a large thermal anomaly about 500°C (Thébaud & Rey, 2013).

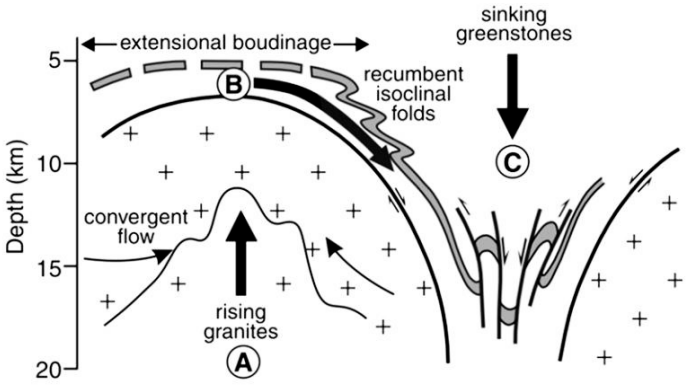

Fig. 2: Diapirism and sagduction within granite-greenstone-complexes, accompanied by extensional boudinage & isoclinal folds within dome and subvertical shearzones at contact to greenstones (Van Kranendonk et al., 2015).

1.2 Regional Geology of the Yilgarn Craton, Western Australia

The western part of Australia is an assemblage of old cratons like the Western Australian Craton and the Northern Australian Craton. The former is itself an arrangement of the smaller Pilbara Craton, Yilgarn Craton and the Glenburgh Terrane, which have been sutured during the Proterozoic (Johnson, 2013).

The Yilgarn Craton mainly consists of metavolcanic and metasedimentary rocks, mostly preserved as greenstone-belts, and metagranitoids. It is divided into four areas: the Eastern Goldfields Superterrane, the Narryer Terrane, the South-West Terrane and the Youanmi Terrane (Fig. 3). These terranes correlate with different geological entities, as described by Dentith et al. (2000), based on Myers (1993): The Narryer Terrane mainly consists of granitic gneisses with an age of 3.2 to 4.2 Ga and may thus represent the oldest cratonic nucleus preserved in the Yilgarn Craton, while the remaining parts of the craton have an age of 3.3 to 2.6 Ga.

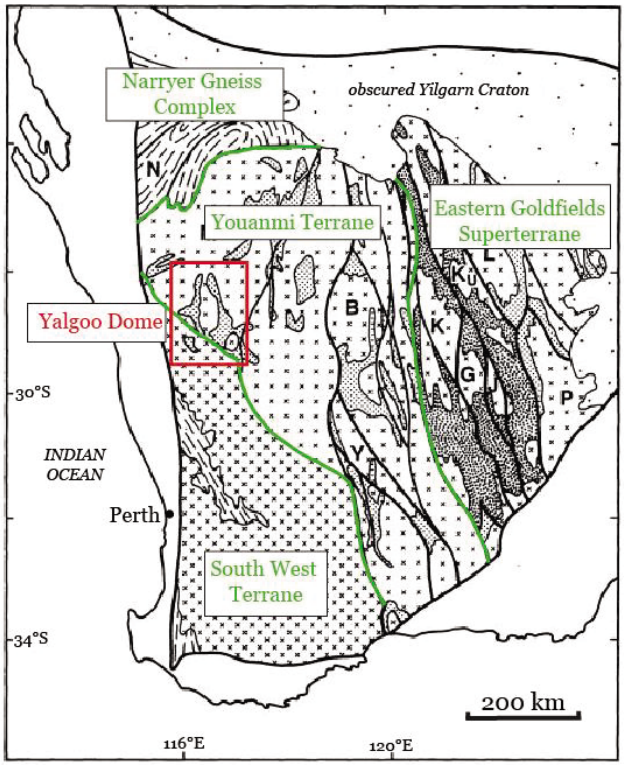

The South-West Terrane is primarily composed of high-grade granitic gneisses, whereas the largest unit of lower-grade granitoid-greenstone-systems is represented by the Youanmi Terrane and Eastern Goldfields Superterrane. The latter is dissected by many north-trending shear zones and is famous for its large gold deposits. The ages are given by Champion & Cassidy (2007) (Czarnota et al., 2010) and Pidgeon & Wilde (1990). The Yilgarn Craton is bordered by the Darling Fault and Perth Basin in the East, the Capricorn Orogen in the North and the Albany-Fraser-Orogen in the Southeast.

Fig. 3: Geological Map of the Yilgarn Craton (after Myers, 1993).

Three evolution-models have been proposed for different domains and episodes of the Yilgarn Craton: a) a plume model (Archibald et al., 1978; Campbell & Hill, 1988), b) a rift-model (Swager, 1997), and c) arc-accretion models (e.g., Barley et al., 1989; Myers, 1990). The plume model focusses on the crust formation of the Youanmi Terrane and explains well the occurrence of five layered mafic-ultramafic intrusive sequences in the northern Murchison Domain. These heating events probably accompanied a period of crustal extension, which was postdated by collision and accretion tectonics (Ivanic et al., 2010). Considering isotopic data, the Murchison Domain developed between 2820 and 2600 Ma through autochtonous processes, probably including multiple mantel plumes generating mafic mantle-melt and partial melt of the crust, and thus contributed to its recrystallization (Ivanic et al, 2012). This time span of crustal reworking is consistent with the above mentioned ages of the Yalgoo Dome-granitoids and -greenstones. Most of the granitoid rocks in the Murchison Domain were produced by partial melting of the crust. This is proved by the presence of pegmatite-banded gneisses and recrystallized monzogranites, which in turn derived from melt of mafic crustal rocks, e.g. initial lower crust representing relicts of oceanic lithosphere. Emerging felsic intrusions metamorphosed the surrounding greenstones to amphibolite facies and the granitoids themselves were later regionally overprinted by greenschist to amphibolite-facies metamorphic conditions, except from the post-folding granitoids intruded at ~ 2.6 Ga (Watkins et al., 1991). This epoch of intense magmatic activity and crustal reworking is mostly contemporaneous with the formation of thick greenstone

deposits on top of the felsic crust in the Yilgarn Craton, which derive from mantle melt. The separated, narrow-formed, north-trending distribution of these greenstones indicates a ribbon-style rifting that has been introduced by mantle plumes and crustal extension (Gee, 1978; Ivanic et al., 2010; Van Kranendonk et al., 2013). Moreover, the restriction of granitic plutons to greenstone belts also indicates a tectonic control. There could be a correlation between deep-reaching shear zones as pathways and the emplacement of granite intrusions (Watkins et al., 1991). Gee et al. (1986) proposed three models that may explain the correlation between the high-grade gneisses in the South-West Terrane and the adjacent lower-grade granitoid-greenstone systems of the Youanmi Terrane: a) the cratonic basinal mode, b) the continental marginal model and c) plate collision suturing independent terranes. These three theories take into account that there is no geological unit in the craton representing old island arcs or high-pressure metamorphism, which would point at subduction processes. The plate collision model corresponds to seismologically determined changes in the lateral crustal velocities near the suture zone separating the South-West Terrane and the Youanmi Terrane. A terrane boundary would also explain a nearby area of intraplate seismic activity (Dentith et al., 2000). In summary, the granite-greenstone systems of the Yilgarn Craton represent an interaction of tectonic deformation, large intruding plutons and the formation of long deep-reaching, north-trending shear zones. The intense magmatic activity caused an almost complete recrystallization of the continental crust and the ongoing deformation led to the elongation of large granitic plutons (Zibra et al., 2013).

The Yalgoo Dome is located close to the boundary between the Youanmi Terrane and the South-West Terrane (Fig. 3). Concerning its evolution, Myers & Watkins (1985) propose horizontal tectonics causing a recrystallization and deformation of a greenstone-over-tonalite-sequence, followed by younger monzogranite intrusions reaching the base of the greenstone layer. Subsequently, they prefer dome-and basin fold interferences being responsible for the outcrop shapes of the roundish granite-greenstone complexes with a tonalitic core, a monzogranite mantle and greenstone flanks. In contrast, diapirism models dominating the evolution of the Yalgoo Dome have been proposed by Foley (1997), based on detailed structural observations revealing subvertical tectonic processes. Nevertheless, aeromagnetic images of the migmatic core, which probably formed through fluid-induced partial melting of a tonalite protolith, show a fold-like bended large-scale structure indicating a compressional regime from the east and west (Fenwick, 2014). Thus, diapirism and tectonic deformation might have interacted, forming a roundish but N-S elongated surface structure.

This study aims at understanding the microstructural development of the Yalgoo Dome. In the following chapters, the results of initial microstructural investigations are presented and discussed, with regard to the ideas of diapirism, sagduction, syntectonic plutonism and folding.

2 Methodology

The field work has been done by Ivan Zibra (Geological Survey of Western Australia) gaining information on macroscopic petrological and structural features that were noted in the Warox database. 36 samples were analyzed, which represent three main sites of the Yalgoo Dome (Fig. A1, appendix): the core, the mantle and mantle areas close to the greenstone belt. Thin sections of these samples were prepared, minding an ideal offcut orientation perpendicular to the foliation and parallel to the lineation.

In order to obtain microstructural information concerning the evolution of the Yalgoo Dome, different analytical methods were used. Basic microscope observations were done with a common polarization microscope and information about the lattice preferred orientation (LPO) or rather crystallographic preferred orientation (CPO) of quartz crystals were collected with the Fabric Analyser. Additionally, eight thin sections were digitized and the subsequent grain size analysis was done using Ondrej Lexa's polyLX-Toolbox for Matlab.

2.1 Microstructures in thin sections

2.1.1 Internal deformation without recrystallization

If a rock is deformed at low temperatures, evolving space problems can be solved through lattice bending or deformation twinning, but these modifications can just compensate a small amount of strain. With increasing strain, also the density of lattice defects within the minerals increases and thus the internal free energy augments. The system would always react and try to minimize this energy. In Quartz, this is done by the already mentioned process of dislocation creep acting on distinct slip systems. The dislocation tangles would start to rearrange systematically based on the idea of forming several small defect-free grains instead of one large grain containing many lattice defects. Heat would be a catalyzing factor here. This progressing recovery can be seen under the microscope as undulose extinction and with time, subgrain-stripes are formed, framed by aligned dislocations (Passchier & Trouw, 1998, p.31-33). Feldspar would be affected in a slightly different manner by solid-state deformation. Exsolution lamellae (i.e. flame perthites with albite lamellae), twinning and myrmekite are typical features (Vernon, 2004, p.250-252). According to Tribe & D'Lemos (1996), myrmekite is a retrograde feature growing at 450-500°C and after Wirth & Voll (1987), 500-670°C would be the adequate temperature range.

Quartz chessboard pattern as geothermobarometer

This method is based on a special case of subgrain formation. Chessboard pattern in quartz indicates the transition from the low-quartz (α) to the high-quartz (β) field. The former is characterized by prismatic subgrain boundaries (SGB) derived from a dominant basal<a> slip system whithin a trigonal crystal, whereas the transition to the high quartz field with a hexagonal crystallography is marked by a combination of alleviating basal<a> slip and incipient prism<c> slip causing prismatic and basal SGB (Fig. 4). This rectangular pattern is a sign of high-grade metamorphic conditions (i.e. granulite facies conditions) that might be related with syntectonic plutonism, for instance (Kruhl, 1996). This SGB-pattern, which can simply be observed by XPL - polarization microscopy, should just be applied to natural rock samples deformed at low strain rates and maximum pressures of 10kbar (Kruhl, 1998). The temperatures of the low-high-quartz transition range from ~573 °C at 1 bar to ~825 °C at 10 kbar (Van Groos & Heege, 1973).

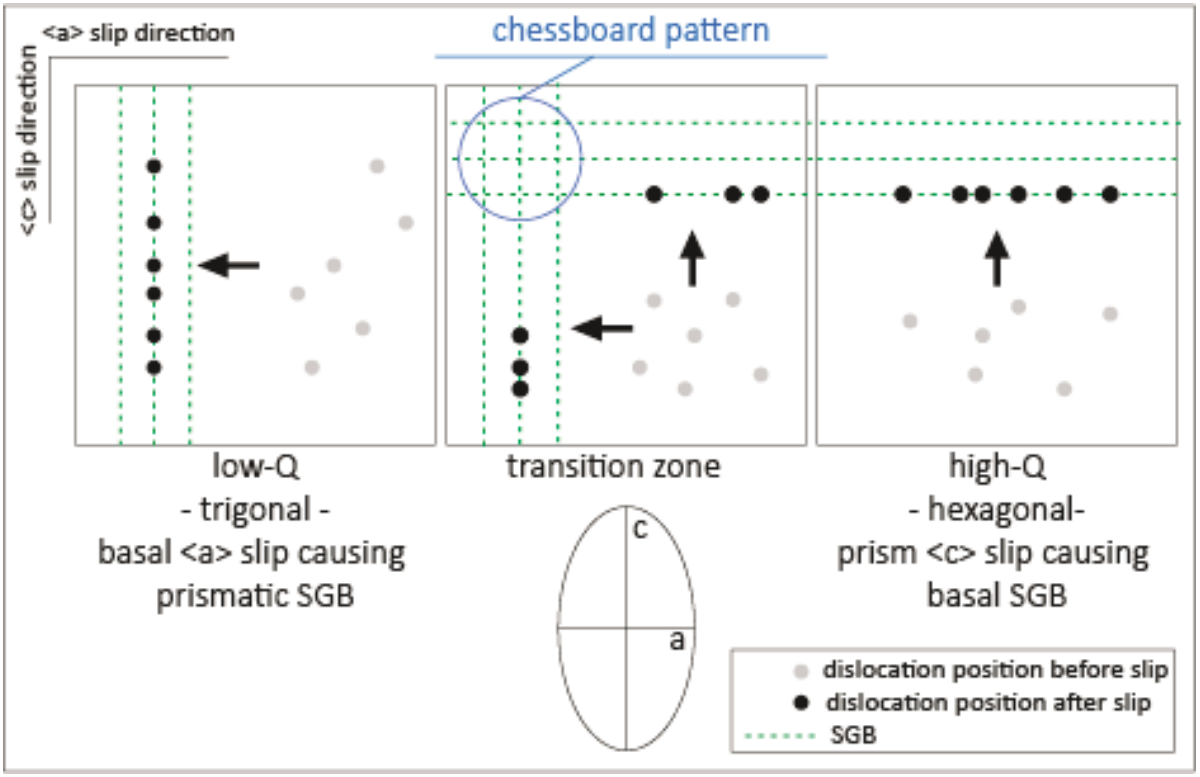

Fig. 4: The formation of chessboard pattern during the transition from low-Quartz to high-Quartz.

2.1.2 Dynamic Recrystallization & Recovery – a function of temperature

At medium to high temperatures and progressing deformation, the above mentioned reordering process would result in the formation of totally new grains via dynamic recrystallization, which occurs at the grain boundaries. Thus, also the shape of the quartz crystal is changed without bending or kinking the lattice. The four main energetic driving forces for dynamic recrystallization are lattice defect energy, grain boundary energy, chemical free energy and external elastic strain energy, which all seek a minimum (Urai et al., 1986). The recovery and dynamic recrystallization processes become increasingly important at higher temperatures and lower strain rates. In consideration of the rates of dislocation production, dislocation creep and grain boundary migration, three systems have been described, with grain boundary migration recrystallization representing the most intense state of dislocation creep (Hirth & Tullis, 1992).

Subgrain Rotation Recrystallization (SGR)

This mechanism is the consequence of progressing deformation and associated subgrain formation, as mentioned above. The more dislocations are part of a subgrain boundary, the higher becomes the crystallographic angle between two grains and their relative misorientation. If it is high enough, the subgrain boundary will turn into a real grain boundary (Fig. 5). This can only happen if the dislocation movement within a crystal is relatively unrestricted (Passchier & Trouw, 1998, p. 36- 37). Thus, SGR is probably an appropriate recrystallization mechanism at medium to high temperatures, which possibly facilitate the movement of dislocations. Subsequent grain boundary migration might stabilize the originated provisional microstructure of a rotated subgrain (Lloyd & Freeman, 1991).

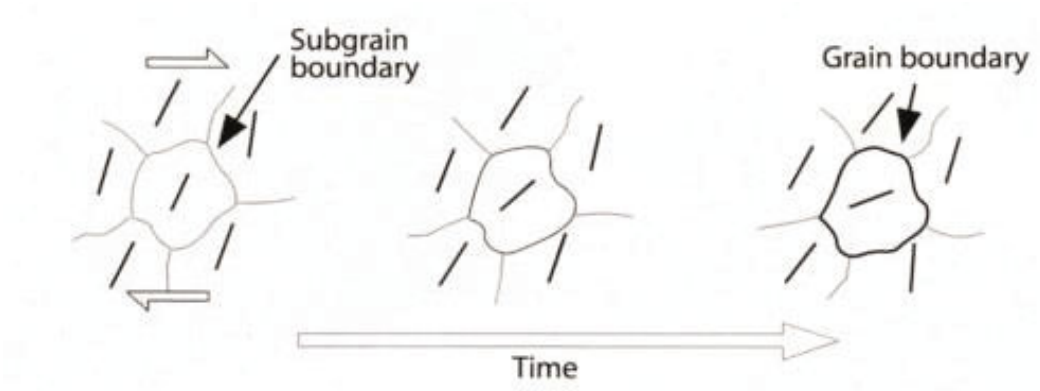

Fig. 5: Progressing Subgrain Rotation (Passchier & Trouw, 1998, p. 36).

Grain Boundary Migration Recrystallization (GBM)

This term describes the intense rearrangement of a crystal lattice with a higher dislocation density, especially close to its grain boundary, until a subarea crystallographically depends to the energetically favoured adjacent grain with a lower dislocation density (Passchier & Trouw, 1998, p. 36). During dynamic recrystallization at high temperatures, grain boundaries would continuously move away from their center of curvature, leading to lobate boundaries and amoeboid-like grain shapes replacing primary straight or wavy grain boundaries (Fig. 6). (Urai et al., 1986 and references therein).

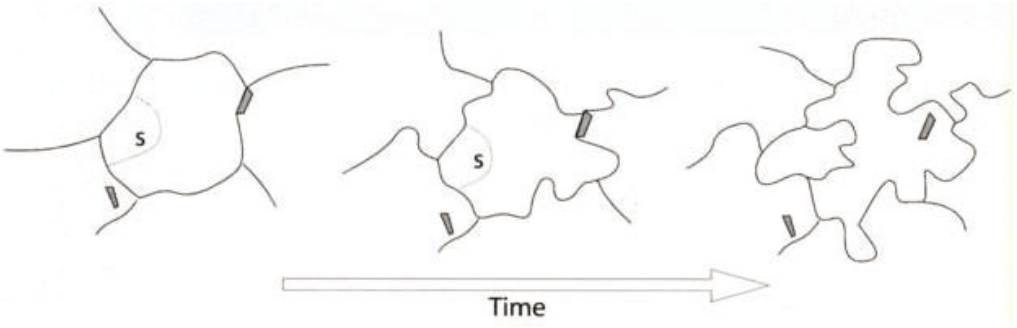

Fig. 6: Progressing Grain Boundary Migration, causing amoeboid grain shapes (Passchier & Trouw, 1998).

Bulging Recrystallization (BLG)

As shown in figure 7, bulging recrystallization probably is a consequence of local grain boundary migration and subgrain rotation. The grain with lower dislocation density bulges into a grain with higher dislocation density and the formation of a local subgrain boundary and its rotation would finally lead to a small new grain (Urai et al., 1986; Stipp et al., 2002; Stipp & Kunze, 2008). Bailey and Hirsch (1962) proposed that the separation of a small new grain from the large host grain is related to microfracturing during progressive deformation (Urai et al., 1986). GBM would always start with initial bulges and it depends on the temperature conditions, if these bulges rotate creating new small grains or if they enlarge and form amoeboid grain shapes.

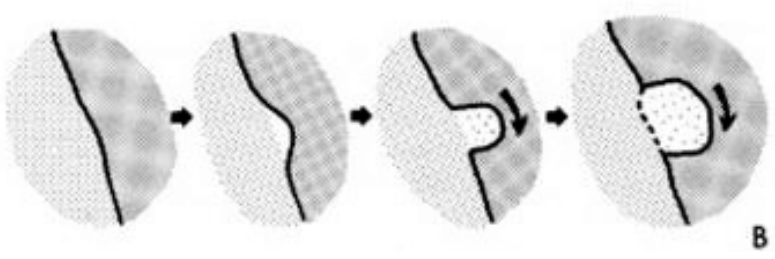

Fig. 7: Bulging Recrystallization combining Grain Boundary Migration & Subgrain Rotation (Urai et al., 1986).

Quartz recrystallization thermometer

Stipp et al. (2002) suggest distinct deformation temperature ranges being responsible for the different quartz microstructures described so far (Table 1).

Table 1: Different dynamic recrystallization mechanisms at different temperature ranges

Temperature range [°]	**Dominant dynamic recrystallization mechanism**
280 - 400	Bulging (BLG)
400 - 500	Subgrain Rotation (SGR)
>500	Grain Boundary Migration (GBM)

This thermometry method is just valid for strain rates and water contents associated with these particular fault rocks sampled by Stipp et al. (2002). Composite BLG & SGR are dominant close to a fault zone at lower temperatures & higher strain rates & lower water contents and GBM becomes dominant at higher temperatures & lower strain rates & higher water contents far away from the fault zone (Law, 2014, and references therein). Hydrolytic weakening influences the deformation mechanism of quartz: with increasing temperature, water diffusion into the crystal lattice is facilitated, where it enhances dynamic recrystallization. Along grain boundaries, water would reduce cohesion. Nevertheless, the critical weakening temperature increases with increasing strain rate (Griggs, 1967; Blacic, 1975).

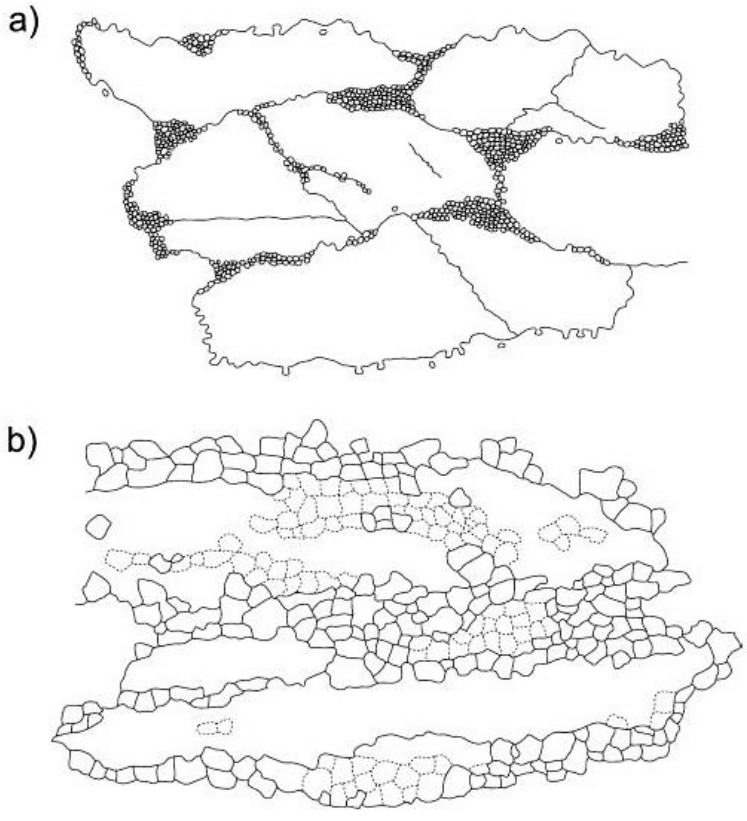

Fig. 8: Grain size reduction, a) Bulging Recrystalliazation texture, b) Subgrain Rotation Recrystallization texture (Stipp et al., 2002).

The dynamic recrystalliazation processes BLG and SGR cause an overall grain size reduction, with large initial grains, surrounded by smaller grains of the same size as evolving bulges or subgrains; core-mantle structures are formed in this way (Fig. 8). This principle would result in the establishment of a bimodale crystal size distribution (Passchier & Trouw, 1998, p.37; Stipp et al., 2002). With increasing strain, porphyroclasts are progressively elongated and consumed by dynamic recrystallization (Stipp & Kunze, 2008). Nevertheless, heterogeneous textures might also develop through competency contrasts in polymineralic rocks, for instance between weaker quartz and more rigid feldspar. These material contrasts arise as consequence of quartz becoming ductile at 300°C and feldspar at 500°C, which is responsible for the establishment of larger pure quartz aggregates & ribbons and finer grained areas containing rigid minerals like feldspar and mica, the latter being more influenced by imposed strain. Quartz ribbons are typical of high-grade-metamorphic rocks and they probably form by intense plastic deformation causing a flow-behavior of quartz combined with its recrystallization (Vernon, 2004, p. 348-352).

The GBM mechanism at higher temperatures would not lead to a continuous grain size reduction, but it causes a more 'homogeneous' optic on the microscopic scale with dominant irregular grain sizes and lobate grain boundaries (Fig. 9) (Stipp et al., 2002). With the onset of GBM above ~500°C (table 1), also feldspar starts behaving ductile and recrystallizing via dislocation creep mechanisms (Tullis & Yund, 1985), which reduce the above mentioned competency contrasts.

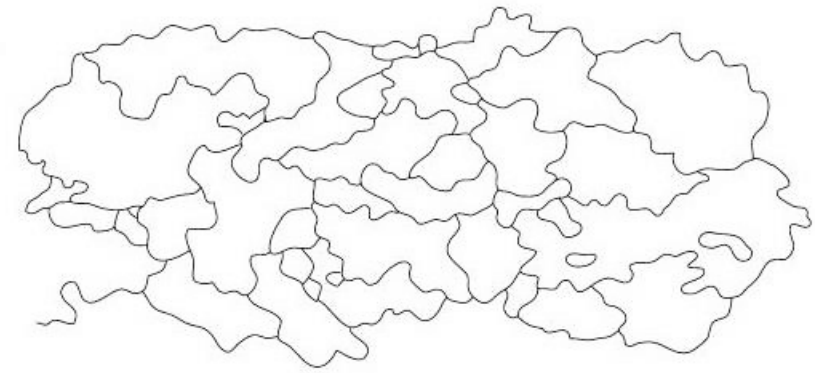

Fig. 9: Grain Boundary Migration texture with large amoeboid grains (Stipp et al., 2002).

At higher temperatures and higher strain rates, solid-state diffusion creep becomes an important factor. It is characterized by the movement of vacancies through the lattice or along the grain boundaries in answer to imposed heat and deformation and it provokes a superplastic behavior of crystals. Quartz grains, for instance, may start to slide past each other, adapting perfectly to the boundaries of the surrounding grains. Thus they are able to follow the strain induced moving direction without creating voids (Passchier & Trouw, 1998, p.40-42). This process is described as Grain Boundary Sliding (GBS) and it mainly occurs in

fine-grained materials (Boullier & Gueguen, 1975). In fine-grained rocks, diffusion paths for vacancies are relatively short and thus, GBS would be easier than in coarser materials. It should be noted that this high-strain process does not affect the lattice preferred orientation. (Passchier & Trouw, 1998, p.41)

Ultra-high-T deformation

Melt will be present in rocks if the 'wet solidus line' in a p-T diagram is crossed. It lies between 640°C and 800°C, depending on the pressure conditions. Vernon (2004, p.458-463) mentions some features that might help to recognize melt-present deformation in case of lower melt-percentage, which is expected to have occurred in the high-grade metamorphic rocks and migmatites of the central parts within the Yalgoo Dome:

Intracrystalline plastic deformation
GBM assisted contact melting & melt-assisted GBS
Melt enhanced embrittlement
Strain partitioning into melt-rich zones

However, a kind of 'magmatic optic' mostly is the only indicator for melt-present deformation and might be associated with a nearly complete recrystallization of the rock. In few cases, magmatic microfractures can be determined in thin sections, due to their acute dihedral angle with the surrounding grain. Progressive partial melting would lead to Schlieren layering and pegmatitic veins, which would be visible on the macroscopic scale.

Annealing effects

In addition to dynamic recrystallization, which has produced highly irregular grain boundaries, steady-state -recrystallization may occur after high-T deformation has finished and the rock is still heated and hydrated. The high temperature and water would enhance the recovery processes to continue until the energy within the system is minimized. This process is accompanied by grain boundary area reduction (GBAR), which leads to an overall coarsening associated with decreasing surface energy. Some large grains would grow consuming smaller grains. Nevertheless, crystal growth might be restricted due to the presence of other minerals 'pinning' the grain boundaries (Passchier & Trouw, 1998, p.43-47). Grain boundaries would migrate towards their centers of curvature during this secondary recrystallization, causing energetically favoured straight boundaries and polygonal shapes (Urai et al., 1986).

2.2 Grain-Size-Analysis

2.2.1 Digitalization of grains with ArcGIS

In order to collect grain size and grain shape data of Quartz and Feldspar, eight samples were chosen representing core-, mantle- and marginal sites of the Yalgoo Dome: 155806, 155827, 155850, 155867, 155870, 1557876, 210277 and 210297. These samples are comparative due to their petrography, as all are modifications of granitic gneisses. Additionally, they represent the CPO patterns dominating the associated location within the dome. It should be noted that this is a quite small number of thin sections representing the dome structure, and further analysis of more samples is necessary. The grain shape information is manually gained via systematic digitalization of thin section photos in ArcGIS, comprising the workflow described below. To ensure the comparability of the results, all eight photos were prepared using the same zoom of 1:10000. Due to a camera with a high resolution of 1.725 µm / pixel, the grain boundaries defining the grain shapes have been sufficiently recognizable despite a highly zoomed view. For this thesis, a minimum number of respectively 100 grains of quartz and feldspar is presumed to be required for a useful grain size analysis.

Workflow:

1) Creation of new Geodatabase in ArcCatalog.
2) Loading photo of thin section in ArcGIS as new project and applying the *Georeferencing* point tool to define the coordinates of three corners based on the known photo-dimensions and the above mentioned resolution of the picture.
3) Generating a *Grid-Feature Class (1200 x 1200 µm spacing)* with an appropriate Data Management Tool, covering the photo with about 500-600 points.
4) Adding an empty Feature Class to the database and subsequently to the digitalisation project as basis for *polygons sketched with the Editor-Streaming-Tool, framing grains along their grain boundaries*; only grains marked with a grid point are considered. Simultaneously, the appropriate ID and phase name are manually assigned to the table of attributes, describing each polygon within the Feature Class.
5) Converting the Feature Class into a *Shapefile* which can be handled in Matlab.

Finally, the size of all polygons is exactly defined in microns due to the previous spatial referencing. It should be noted, that we are just dealing with two-dimensional crystal size values and that the sample offcut also decides on the grain area visible in the thin section plane (Higgins, 2006). In few cases, the grid points also marked other minerals than Quartz and Feldspar and thus, also grains of Micas, Titanite and Chlorite were digitized, but their quantity is not statistically useful; only the Mica could be assistant concerning the determination of a foliation orientation.

2.2.2 Analysis with Matlab (polyLX)

Subsequently, the shapefiles containing grain size information were imported in Matlab and handled with the polyLX toolbox developed by Lexa (2003a,b). The Matlab code is attached in the appendix. The analysis has been focused on information about the grain area, grain shape, grain orientation and grain size distribution. For all these features, the mean values were calculated and plotted against the sample indexes ordered by their locality within the Yalgoo Dome (Table 2: marginal = close to the greenstone belt; mantle = monzogranite mantle between greenstones and center; center= tonalitic migmatite in the center of the Yalgoo Dome & the center of a nearby small emerging dome on the other side of the greenstones in the southeast).

Table 2: List of digitized samples and their localities within the Yalgoo Dome

Sample Index	Sample	Locality
1	155806	*marginal (NE)*
2	155870	*marginal (SE)*
3	210277	*marginal (NW)*
4	210297	*marginal (W)*
5	155867	*mantle (SE)*
6	155850	*mantle (NE)*
7	155827	*Core*
8	155876	*core (SE)*

Grain size

The grain area is given as Equal Area Diameter (EAD), which describes the diameter of a perfect sphere that has the same area as the original grain (Fig. 10). Lexa (2003b) uses the term Feret diameter (F) and gives the formula as follows, with A as grain area:

$$F = 2 \cdot \sqrt{\frac{A}{\pi}}$$

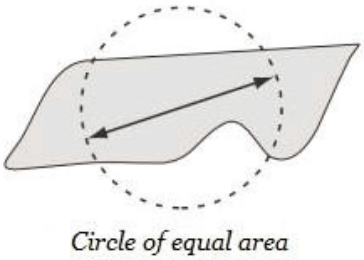

Fig. 10: EAD (Higgins, 2006, p. 77).

Additionally, general grain size frequency histograms with equal size bins were prepared and they reveal unimodal or bimodal size distributions. In chapter 2.1.2, processes influencing the grain size have already been mentioned. Finally, competing grain size reduction and coarsening mechanisms lead to an 'equilibrium' crystal size distribution, which is distinct

from the original magmatic or sedimentary CSD, depending on the protolith (Higgins, 2006, p. 59-60). According to Stipp & Tullis (2003), a correlation exists between the grain size of recrystallized crystals and the flow stress within diffusion creep regimes. They developed the Paleopiezometer method, which, however, has not been applied here.

Crystal Size Distribution (CSD)

The crystal size distribution has been determined using the 'pcsd' command of Lexa (2003b), which is based on the methods described by Peterson (1996). The exponential crystal size distribution within magmatic rocks depends on the initial nucleation density (n_o), the constant growth rate (G) and the residence time (t) in the magma chamber (Marsh, 1988; Peterson, 1996). However, for metamorphic rocks, recrystallization processes must be considered and thus, the time span of deformation and heating should be the one of interest (Cashman & Ferry, 1988). The CSD is presented in a diagram with the logarithm of the population density ln(n) as y axis and the crystal length L as x axis (Fig. 11). Generally, the population density of small crystals is higher than the population density of large crystals. Thus, the correlation is inverse and the slope is negative. The CSD line can be exactly defined based on the following features (Marsh, 1988; Peterson, 1996):

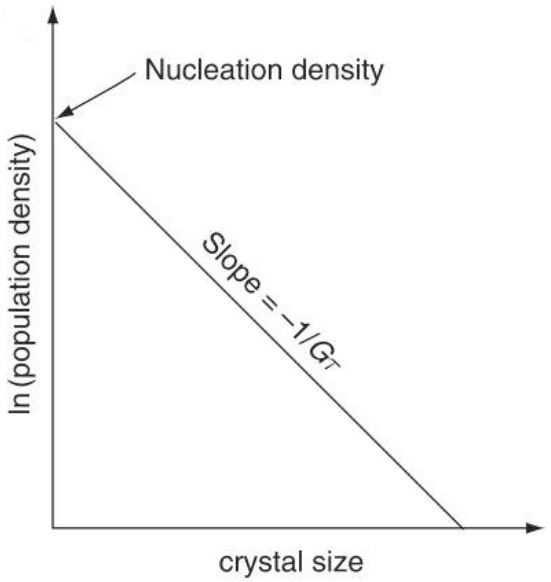

Fig. 11: Linear CSD plot (Higgins, 2006, p. 49).

Slope of linear CSD plot	**y-Intercept of linear CSD plot**
$-\frac{1}{\alpha}$ with $\alpha = G \cdot t$	$n_0 = \frac{dN}{dL}\ [\frac{1}{\mu m^4}];\ \ L = 0$

L: length of longest diameter [µm]
N: number of grains per unit volume with length ≥ L

The population density is than given as follows (Marsh, 1988):

$$n = n_0 \cdot e^{-L/\alpha} \quad .$$

A linear CSD is typical of contact-metamorphic rocks with constant nucleation and growth rate. In contrast, regional metamorphism would cause bell-shaped CSD plots. This can be explained due to annealing-/ coarsening processes following previous nucleation and crystal growth during dynamic recrystallization: The dissolution of smaller high-surface-energy grains and simultaneous growth of originally larger grains would bend the linear CSD plot in the small-grain-size/high population density field in figure 11, leading to lower population densities of small crystals .

In this context, Lexa (2003a) mentions the term 'annealing attractor'. He plotted n_o versus α, which together form a curved distribution (Fig. 12). He explains that metamorphic rocks with different deformation histories would plot in different fields. On the one hand, this can be due to solid-state annealing, during which very small and very large n_o- and α- values would trend towards an equilibrium state comprising a relatively homogeneous grain size distribution (Cashman & Ferry, 1988). In this case, high-grade metamorphic rocks would plot close to the center of the n_o/α plot representing textural equilibrium. On the other hand, the different positions in the n_o/α plot could be caused by grain sizes being dependent on temperature and strain conditions during dynamic recrystallization. With increasing temperature and decreasing strain rate, grain size increases causing lower n_o/α ratios. With decreasing temperature and increasing strain rate, grain size is reduced, causing higher n_o/α ratios (Bell & Hickey, 1999).

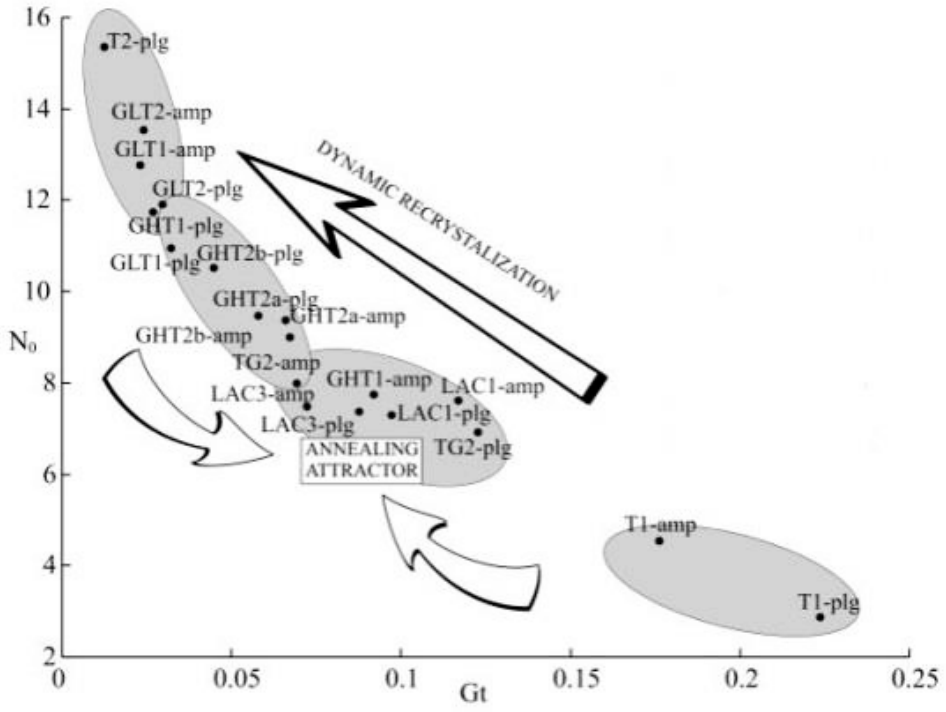

Fig. 12: n_o/α plot of Lexa (2003a), with the annealing attractor in the center of the curve and the progressing dynamic recrystallization path leading to an overall grain-size reduction (higher n_o/α ratios).

Grain shape

Just as the grain size, also the grain shape is influenced by deformation mechanisms and the subsequent annealing. The shape of the grain boundaries (lobate, straight, bulges) has been determined via thin section microscopy, as described in chapter 2.1.2. Other useful attributes representing the grain shape are the axial ratio and elongation of a fitting ellipse (Fig. 13), as well as the degree of roundness or circularity (Higgins, 2006, p. 136).

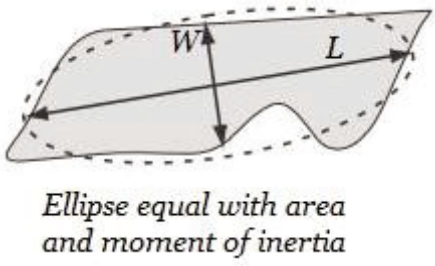

Fig. 13: Ellipse fitting (after Higgins, 2006, p.

The formulae used in the polyLX toolbox were given as follows by Lexa (2003b):

Axial Ratio (AR)	**Elongation (E)**
$AR = \frac{L}{W}$	$E = \frac{\pi L^2}{2A} = \frac{1}{R}$
Roundness (R)	**Circularity (C)**
$R = \frac{4A}{\pi L^2} = \frac{1}{E}$	$C = \frac{4A}{PL}$

A:	Area of grain [µm²]
L:	Length of longest diameter [µm]
W:	Width (perpendicular to L) [µm]
P:	Perimeter of grain [µm]

All these attributes are dimensionless. The factor roundness is the reciprocal value of the elongation and describes the relation between the grain area and the area of a sphere with the diameter equal to L. The factor circularity represents the relation between area and perimeter. Both values vary between one for a perfect sphere and zero for an infinitely elongated and angular grain. The elongation values may vary between 1 for a perfect sphere and infinitely large values for an infinitely elongated grain.

Grain orientation

The grain orientation depends on deformation related directional strain and temperature conditions that may cause grain elongation and special arrangement in a certain direction during dynamic recrystallization. If new grains nucleate and grow from solid material or old grains are transformed, they would take the 'easiest path' and develop an orientation for which the crystal growth energy is minimized (Higgins, 2006, p. 167). This is known as shape preferred orientation (SPO) or long axes orientation (LAO). It describes the orientation of the longest diameter L in [°] clockwise from the vertical direction (Lexa, 2003b). Recovery mechanisms postdating the deformation may destroy the established foliation/ lineation orientation via progressing coarsening (Higgins, 2006, p. 170).

The polyLX instructions 'aorten' and 'prose' were used to calculate the mean LAO of grains and to graph the LAO distributions as rose chart (Lexa, 2003b). As mentioned in chapter 2.3.2, the reference foliation and lineation lie in the XY plane of a stereonet or rosechart, which is located 90° from the vertical (Z) direction. Thus, the rotation angles, derived from the oblique foliation and lineation in thin sections, were used to rotate the calculated LAO's (Table A2 & Fig. A2, appendix). In ideal case, the LAO distribution in the rose charts should finally trend towards 90° from the vertical direction. The mean LAO is marked as red line within the rose chart. Moreover, the width of the standard deviation, marked as red bows at the margin of a rose chart, might indicate the intensity of strain that has been imposed on the rock. High strain would induce a better defined alignment of minerals than low strain.

2.3 Crystallographic preferred orientation data

2.3.1 The Fabric Analyser techniques

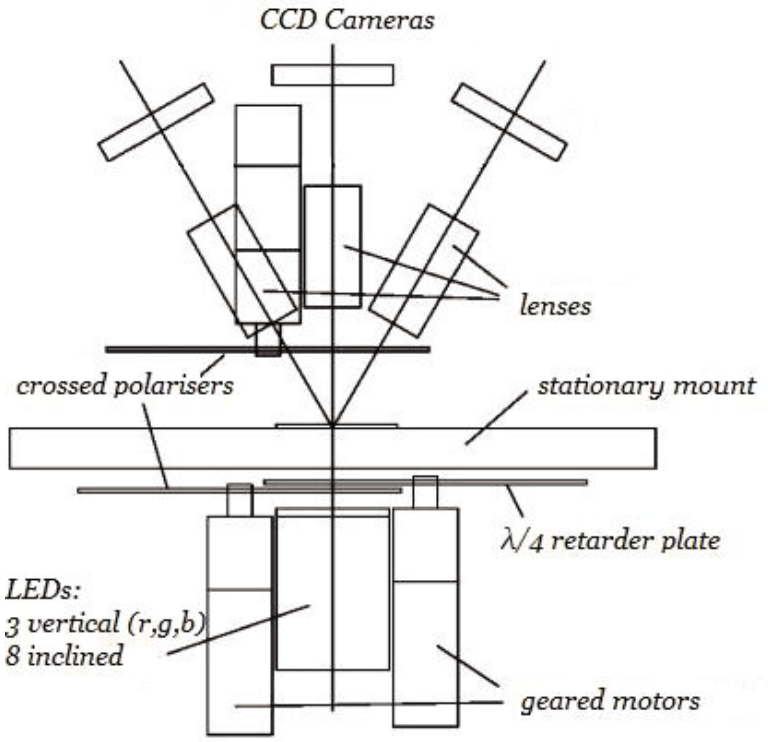

Fig. 14: Fabric Analyser setting – Front View, modified after Wilson et al. (2003) and Peternell et al. (2009).

The Fabric Analyser techniques work in two steps: the c-axis-data acquisition with the Fabric Analyser instrument, followed by the individual selective analysis using the INVESTIGATOR software (Wilson et al., 2003). The construction of the instrument (Fig. 14) resembles a polarization microscope, but due to an automated process including many different inclined light sources, rotatable polarizer- / retarder-plates and theoretical Discrete Fourier Transform methods, the c-axis orientations within uniaxial crystals can be measured (Peternell et al., 2009).

In summary, the extinction plane, which contains the c-axis, is determined from each of the 9 light source positions (Fig. 15). Combining these planes, they intersect in one point, in ideal case, and thus define the exact orientation of the c-axis, including azimuth and plunge. This determination of c-axis-orientation is done for each pixel within a scanned tile and enables the creation of axial-distribution diagrams (in german: AVA, 'Achsenverteilungsanalyse'), which basically are images of the scanned tile with colored grains, based on a stereonet-like color code, representing different azimuths and dipping angles (Fig. 15).

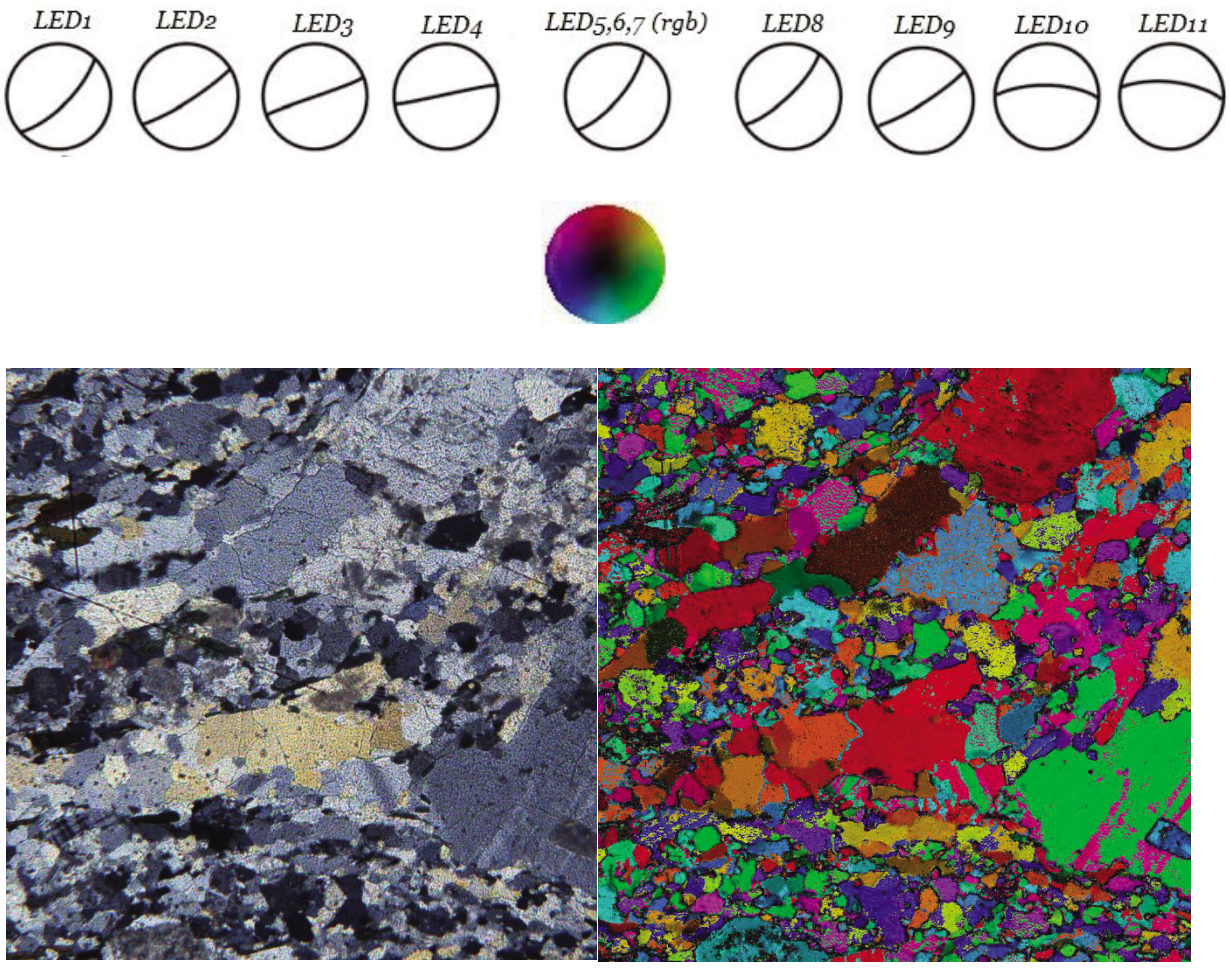

Fig. 15: above: extinction planes from all 9 light source positions; central: circular color-code; down: photo + AVA from thin section tile (5x5 mm).

The precision of 9 extinction planes intersecting defines the geometric quality, also considering the high sensitivity of steeply dipping c-axis to azimuthal errors. The value 100 represents one exactly definded intersection point (Fig. 16). The optical path difference and interference pattern of the three red, blue and green LED - phases compared to the ideal Newton interference colours is described by the retardation quality. Both dimensionless qualities depend on technical components of the FA and especially on heterogeneous material like grain boundaries, chemical impurities or fractures, which reduce the retardation quality and impede the exact tracing of c-axes compared to an ideal homogeneous and uniaxial material. Thus, they are useful to determine grain boundaries and to differentiate between relatively pure and uniaxial quartz grains and more heterogenous, biaxial feldspars that may be a solid solution or may contain zoning and twinning.

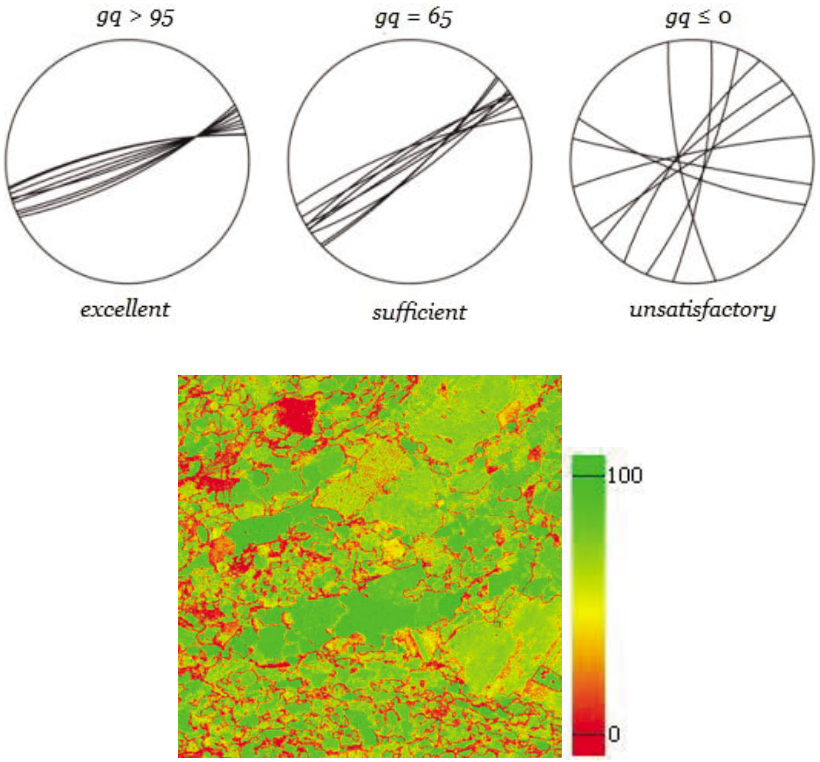

Fig. 16: Above: different geometric qualities (gq); down: geometric quality map of thin section tile (5x5 mm) and connected color-code.

Finally, the FA has produced a set of photos and maps based on the above described measurements, using different color codes: simple lambda- & crossed polarizer- images and maps for the c-axis orientation, the geometric quality and retardation quality.

In this case, the Fabric Analyser instrument G60 ('crystal instrument') was used to determine the c-axis orientations of quartz grains, employing a spatial resolution of 5 µm. In order to collect CPO data from minimum 300 quartz grains per thin section, ensuring a statistically usable dataset, 6 to 15 tiles with a size of 5 x 5 mm (1000 x 1000 pixel) were collected from all 36 thin sections respectively, depending on the average grain size. The tile position within each thin section was selected manually with regard to a relatively equal distribution. Applying top view, 30 thin sections with a foliation nearly parallel to the long side were scanned horizontally with the label on the right side and those six with a foliation nearly parallel to the short side were scanned vertically with the label down (155831, 155842, 155861, 155870, 155880, 209689) (Fig. 17).

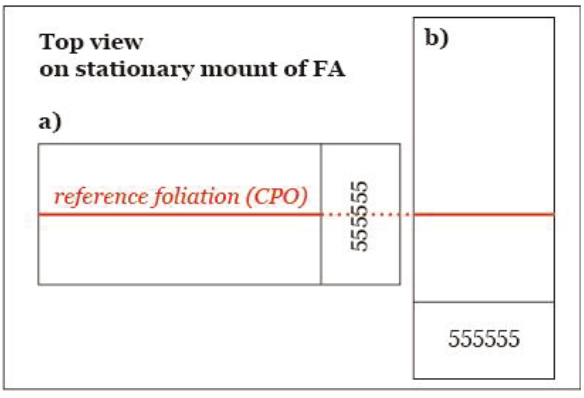

Fig. 17: Position of thin sections on stationary mount of FA: tile-orientation.

2.3.2 CPO data analysis

The INVESTIGATOR G50 v5.11 software

The further analysis of the measured tiles comprises the selection of one point respectively within many quartz grains, minding relatively high qualities, as described above. For this purpose, all tiles of a thin section are successively loaded into the INVESTIGATOR software and a new point set is created for each, in order to finally obtain the c-axis orientations of several hundreds of grains per section, which altogether reveal a distinct pattern of c-axis distribution representing distinct deformation mechanisms and metamorphic grades (Passchier & Trouw,1998). The individual AVA diagrams and quality maps of each tile may assist with the quartz grain selection. The acquired data tables of all point sets contain the coordinates within the tile, the azimuth and plunge, such as the geometric quality and retardation quality of any point. These CPO data tables of each tile were compiled in an excel file representing the results of the whole thin section. The datasets were limited to measurements providing qualities > 75% for c-axis with plunges < 60°, to sharpen the CPO distribution of relevant high-quality axis (Peternell et al., 2009). In case of c-axis dipping angles > 60°, which induce lower qualities due to higher azimuthal errors, qualities > 30% are supposed here as sufficient, in order to avoid a lack of steep axis in a distribution diagram. Applying these limits, the datasets are just rarely reduced, as the point selection was done carefully.

Graphical Presentation with Stereo32

The most descriptive presentation of the gained CPO data is a classical stereographic projection, in which the different c-axis-orientations form distinct point clouds. Therefore, the two columns of each edited excel file comprising azimuth and plunge values were stored in additional text files and subsequently loaded into the Stereo32 software. The data are plotted with a density projection as a kind of interpolated point-cloud-distribution, which is based on an equal angle projection of points in the lower hemisphere. The density projection options have been modified using 'scale to multiples of uniform distribution (MUD)' and adjusting color-filled contours with high quality, as well as a scale bar (Fig. 18).

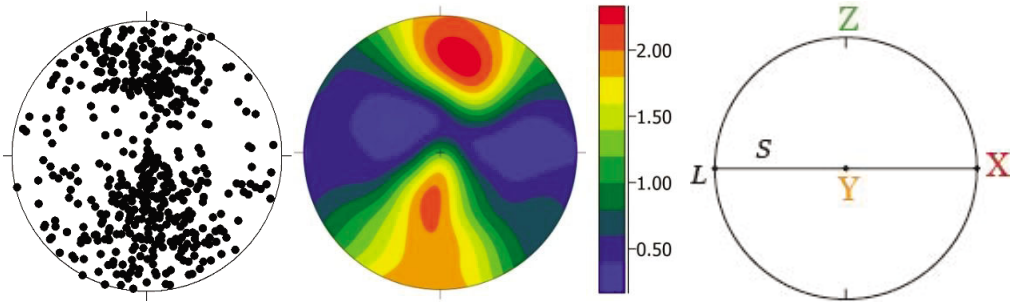

Fig. 18: Left: point cloud of c-axis in stero32; central: density projection of c-axis (mud); right: reference frame.

Additionally, 28 of 36 datasets had to be rotated using Stero32, as the identified foliations are inclined and thus not parallel to the long side or short side of the thin section. In few cases even the whole offcut is oblique. The foliation orientation has been determined on the basis of the arrangement of elongated quartz, feldspar and mica grains. The rotation has been done specifying the rotation axis in Clar-Notation and the rotation angle, with positive values inducing a clockwise rotation and negative values in case of a counterclockwise rotation (Fig. 19, Fig. A2 & Table A2 in appendix).

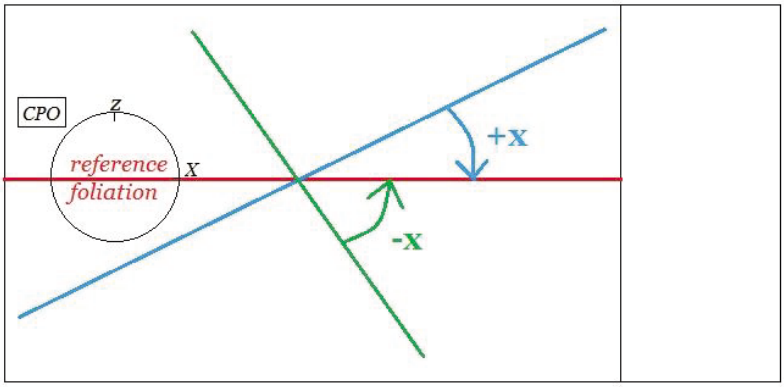

Fig. 19: Schema of Rotation around Y-axis.

2.3.3 Interpretation of CPO plots

The main deformation mechanism of quartz grains forming a CPO is dislocation creep (Passchier & Trouw, 1998, and references therein): depending on the crystallographic slip plane and slip direction on which the lattice defects move, the c-axes simultaneously rotate in a distinct direction and thus a crystallographic preferred orientation is generated (Fig. 20). In table 3, the ideal correlation between slip system and CPO pattern as a function of temperature is described (Passchier & Trouw (1998, p. 48-53 & p.90-95 and references therein), based on the reference system shown in figure 18. The activation of certain slip systems at distinct T-ranges approximately correlates with the transition temperatures between dominant dynamic recrystallization mechanisms (Gleason & Tullis, 1993), as described further below.

Table 3: The ideal correlation between slip system and CPO pattern as a function of temperature

Metamorphic grade	T-range [°]	Slip system	Position in Stereonet
low - medium	300 - 400	basal <a> slip	Z max
medium-high	400 - 650	rhomb <a> slip prism <a> slip	Intermediate max Y max
very high	>650	prism <c> slip	X max

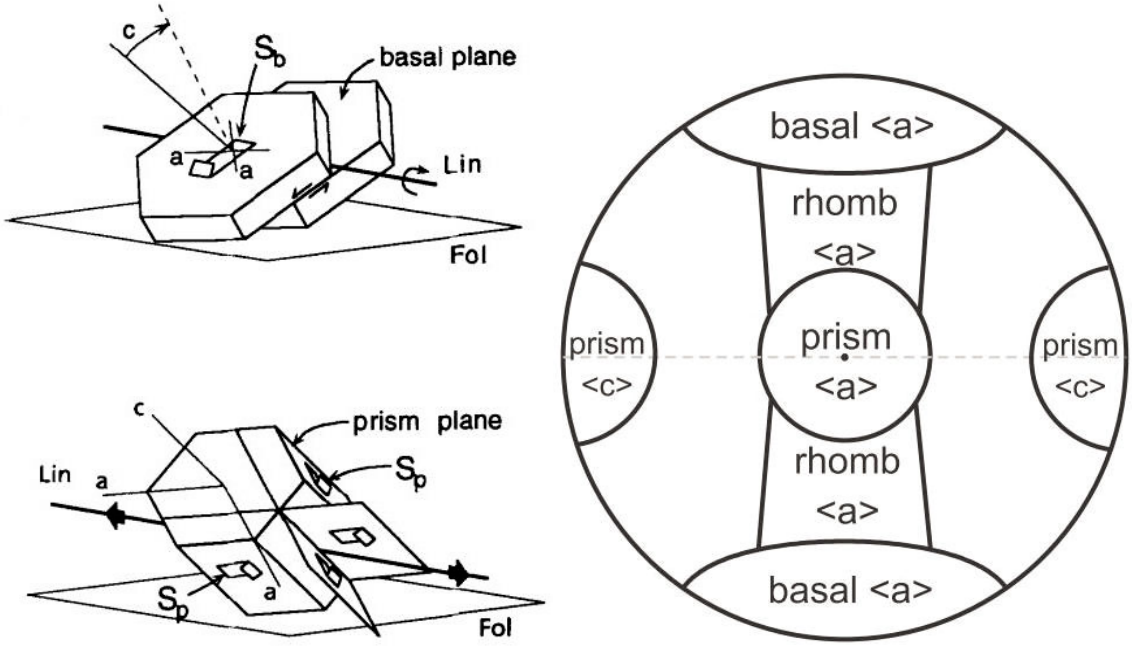

Fig. 20: Left: basal and prism slip plane (Pauli et al., 1996); right: CPO for different slip systems (Toy et al., 2008).

However, also higher differential stress caused by cohesion between grains should be taken into account, leading to the establishment of several slip systems and the formation of single or crossed girdles at lower temperatures (Lister, 1977) (Passchier & Trouw, 1998). Small circle girdles, for instance, derive from combined basal<a> and rhomb<a> slip (Tullis, 1977). Crossed girdles would combine basal-rhomb-prism<a> slip. A single active slip system would cause point maxima in X, Y, Z or intermediate position. The point maxima in Y and X direction are rather typical of higher temperatures, which enable the activation of just one dominant slip system due to possibly more hydrous conditions leading to a plastic softening and decrease of differential stress (Mainprice et al., 1986).

These patterns commonly show an external asymmetry, which is typical of non-coaxial deformation involving simple shear and might help determining the sense of shear. In case of plane strain, with a constrictional and flattening component of pure shear, symmetric CPO distributions evolve, as described by Lister & Hobbs (1980), who present their data within a Flinn diagram. Considering the main patterns deriving from different deformation conditions, one can distinguish between single girdles, point maxima, Type I & II crossed girdles and small circle girdles (Schmid & Casey, 1986).

Quartz c-axis opening angle thermometer

Figure 21 shows opening angles of two different CPO patterns. A correlation exists between small opening angles close to a fault zone and large opening angles away from the fault. The former is related to lower temperatures & higher strain rates & lower water contents and the latter is connected with higher temperatures & lower strain rates & higher water contents. Thus, regarding temperature, the general conclusion can be drawn that the opening angles increases with increasing temperature. However, Caledonian mylonites of studies reviewed by Law (2014), revealed extremely high opening angles related with extraordinary high water contents and emphasizes that the effect of strain and water weakening should not be ignored. Nevertheless, the opening angles thermometry model proposed by Kruhl (1998) comprises supposable strain rates and water contents involved in natural deformation (Law, 2014 and references therein).

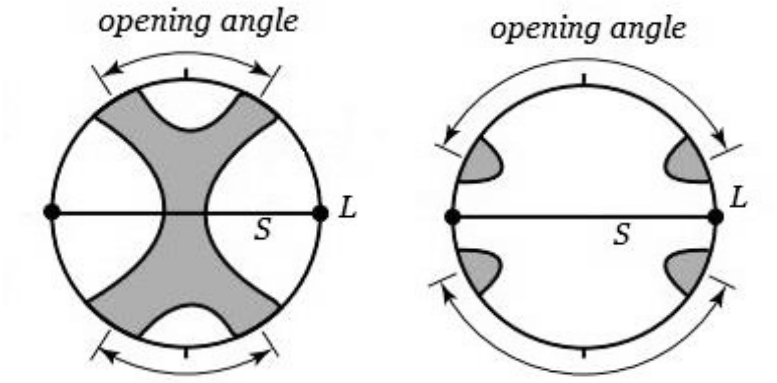

Fig. 21: Opening angles in a crossed girdle pattern or a point maxima pattern (Law, 2014).

3 Results

3.1 Microscope Observations & Field Data

The 36 rock samples of the Yalgoo Dome represent modifications of granite in most cases, representing original gneisses or enclosed veins. Thus, typical minerals are quartz and feldspar (alkali feldspar and plagioclase), yet in most samples additional biotite and titanite occur. A few rocks representing greenstones are metapsammites, which are mainly quartz-dominated, or metapelites (155819, 155883, 210280, 210282, 210284). The lack of typical minerals representing distinct metamorphic facies impedes the reconstruction of a chronologic metamorphic pressure-temperature path and thus, the reconstruction of the deformation history is difficult. Only mantle - thin section 155850 contains garnet combined with a large amount of sillimanite, indicating temperatures higher than 540°C and hence amphibolite to granulite facies conditions. Some of the migmatic tonalite samples from the core contain more mafic components in form of amphibole and orthopyroxene. Amphibole as mafic mineral in central samples indicates high temperatures during amphibolite facies conditions. Additionally, chlorite mainly occurs as retrograde mineral in most thin sections replacing biotite; sericite often occurs as alteration product of feldspar. Epidote can mainly be determined within the thin sections of marginal samples (210275, 210276, 210297, 155806 and 155822), which is typical of upper-greenschist to mid amphibolite facies. Nevertheless it may also grow during retrograde metamorphism; in this context, samples 210275 and 210276 show garnet relics surrounded by epidote (Fig. 30h).

The field-measurements of Ivan Zibra indicate a subvertical orientation for nearly all foliations (Fig. 22). They mainly strike subparallel to the adjacent greenstone belt. Considering the outcrop shape of the north-south elongated Yalgoo Dome, most of the foliations strike subparallel to a north-south-profile, yet the foliations of samples 155831 (1a), 155850 (2a), 155876 (1b) and 210297 (4d) are subparallel to an east-west-profile. The dip direction of marginal samples mainly point towards the greenstone belt. The outcrops of sample 155869 (2b), 210276 (4b), 210280 & 210284 (4a) show boudinaged components. In the mantle and core areas, schlieren layering and magmatic veins are particularly common. Moreover, shear band structures close to the greenstone belts were determined on macroscopic scale, indicating an up- or down-movement of the dome structure: at both the western and the eastern marginal site, dome-up and greenstone-down shear sense has been identified, only in the Northeastern area one examined shear sense indicates dome-down and greenstone-up movement (Fig. 23). In the core area, a large dextral strike-slip fault has been observed. It has been difficult to verify these shearing directions via thin section microscopy, as just in few cases, the foliation and wing-shaped core-mantle structures are developed well

enough to determine the shear sense. For instance, sample 210280 and 210284 has a strong mylonitic foliation and thus, shear bands and winged porphyroclasts are well developed showing sinistral sense of shear (Fig. 31). Considering the steeply dipping foliation and lineation orientation, together with the northwestern marginal position of the sample, this shearing direction is compatible with the dome-up shear sense determined by I. Zibra.

Three categories for temperature and strain intensity have been established in this thesis on the basis of information in chapter 2.1.2, in order to reveal a local dependence of rocks which belong to different categories (Table 4 and 5). The results are presented in figure 24, yet it should be noted that this only is a rough classification of rocks concerning distinct strain and temperature ranges. In most cases, it is difficult to draw an accurate conclusion, as more than one possibility exists to interpret the established microstructures. Table A1 showing the associated peak metamorphic facies and strain intensities of all samples is attached in the appendix.

Despite the peak-metamorphic-conditions, most of the very-high-grade granitoid rocks that possibly metamorphosed during melt-present deformation or during primary crystallization, also show moderate-temperature and solid-state deformation signs. For instance, nearly all recrystallized microcline grains show tartan twinning and partly exsolution lamellae (Fig. 29c,d). Very low temperature and high-strain indicators like brittle fracturing or cataclastic flow, have not been determined within the thin sections during microscopic work.

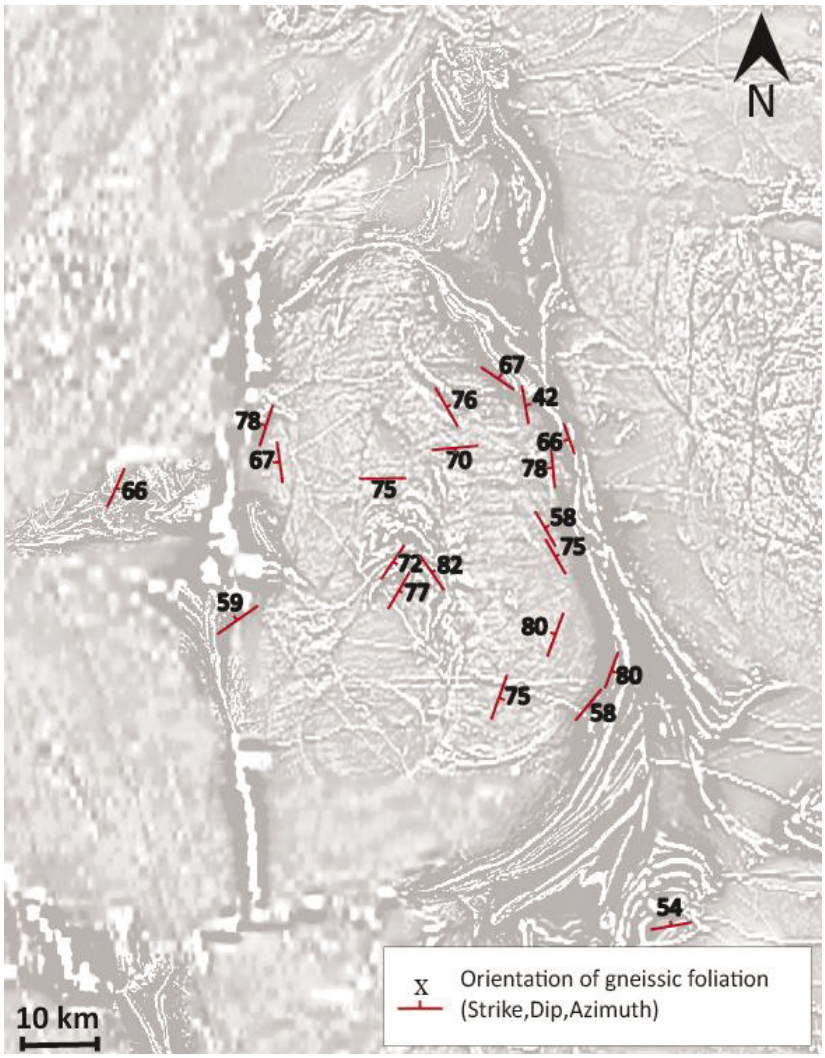

Fig. 22: Foliation orientations determined by I. Zibra in the field.

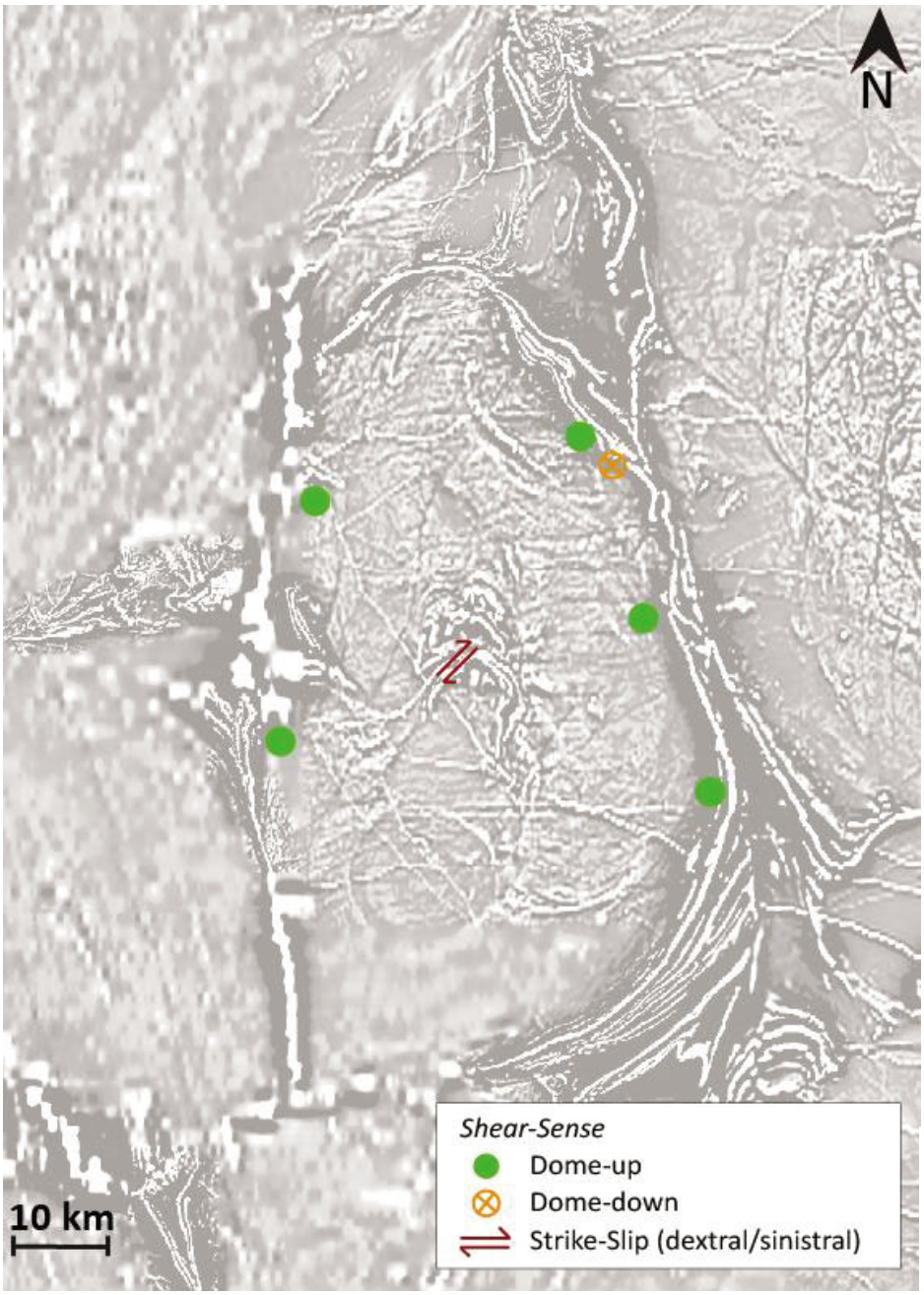

Fig. 23: Shear sense direction, determined by I. Zibra in the field.

Table 4: Strain-categories defined for this thesis

Low strain	No foliation/grain elongation visible and micas not well aligned. The grain size might be coarse.
Moderate strain	A weak foliation is visible due to moderate mica alignment and grain elongation. Orientated ribbons and competency contrast – layers may evolve, causing a bimodale grain sizes.
High strain	Mylonitic-looking and strongly foliated rocks would represent high strain, including highly aligned mica layers (fine grained, blackish striae), sigmoidal porphyroclasts, shear bands. The overall grain size would be quite small.

Temperature-categories

gF: Greenschist Facies (300-450°C)
AF: Amphibolite Facies (450-650°C)
GF: Granulite Facies (>650°C)

Table 5: Three Temperature-categories defined for this thesis describing the textures observed within the thin sections of Yalgoo-Dome-granitoids

medium - high T (upper gF-low AF)	These moderate temperature conditions are characterized by small grain sizes, generated by BLG and beginning SGR of quartz; also the competency contrasts between quartz and feldspar are quite high. Feldspar is still rigid and might be fractured (no real fractures visible in thin sections), develop twinning and exsolution lamellae: myrmekite, flame perthite and tartan twinning in microcline develop. The shape of the feldspar grains might look original magmatic with straight grain boundaries, as no recrystallization modifies the shape. Quartz grains may show deformation lamellae (Fig. 27b). Mylonites develop at very high strain sites. However, these features could also occur during retrograde metamorphism.
high T (mid AF)	These high temperature conditions are characterized by both small and enlarged grains, generated by combined SGR and GBM of quartz grains. Quartz grains show lobate boundaries. Possibly, annealing and coarsening (GBAR) processes caused polygonal grain shapes. Quartz ribbons are common. Feldspar starts to recrystallize and thus, the grain boundaries of feldspar become more sutured. Myrmekite is common.
very high T (upper AF -lower GF)	Intensive and progressing GBM generates very large amoeboid grains (Fig. 28b). Chessboard pattern develops (Fig. 25). Diffusion creep might be initiated, which enables grain flow via GBS. However, this process would not affect the habit of microstructures. Annealing processes like GBAR (coarsening) form partly polygonal grain sizes which seem to be 'strain free' (Fig. 28d). Melt-presence is probable; in this case, the rock looks 'magmatic' and magmatic micro-fractures (acute dihedral angle) are visible (Fig. 29a,b). No mylonites, but gneisses develop at high strain-sites.

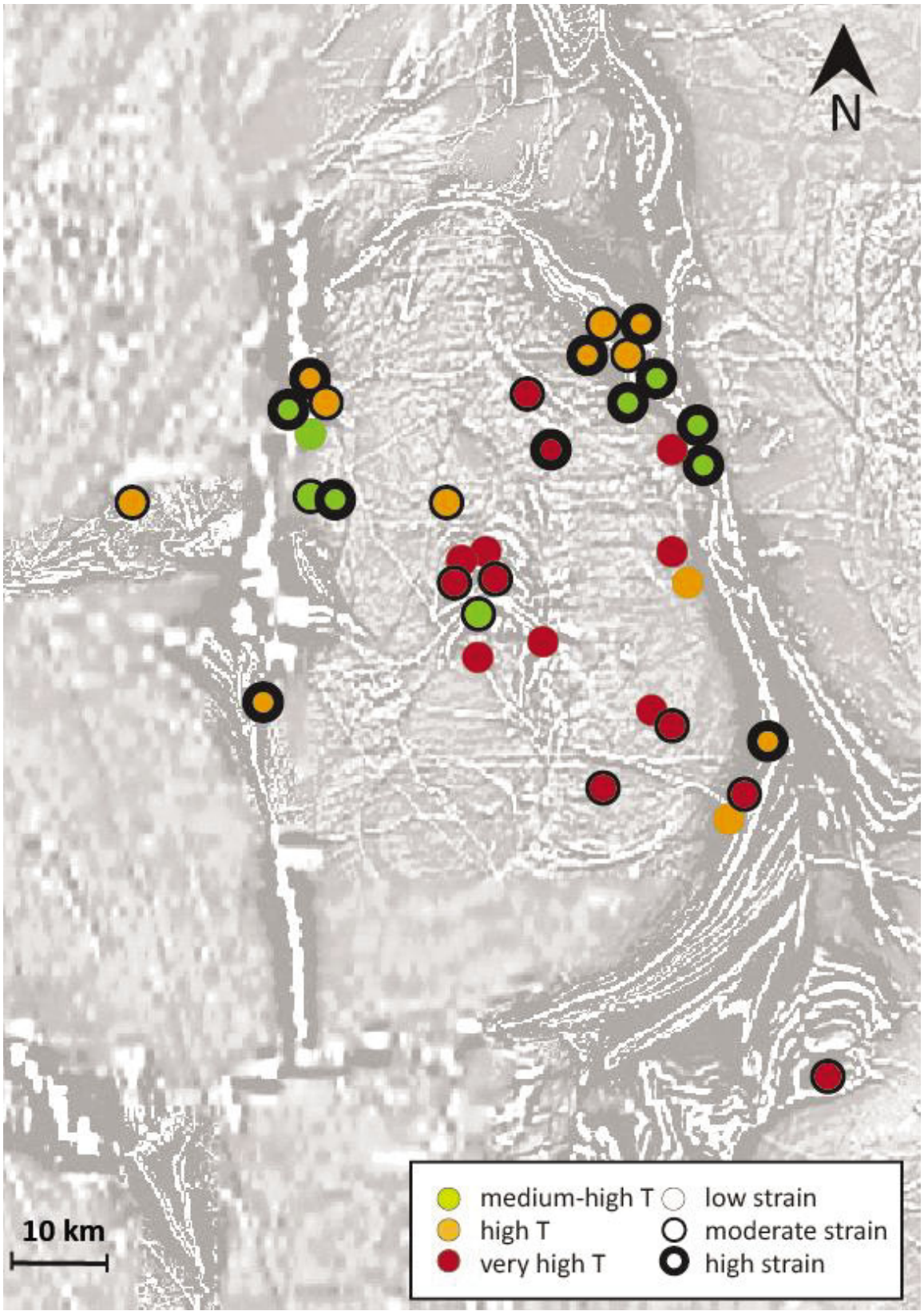

Fig. 24: Results of microscope observations with three categories of temperature and strain.

Nearly all high-strain rocks come from marginal sites close to the greenstone belt framing the dome structure (Fig. 24); 6 of these 12 high-strain samples are related to moderate temperature conditions and 5 are related to high temperatures. Only sample 155850 is categorized as high-strain/very high-T-granite and represents the northern mantle-area. At the northeastern marginal site, 6 of 9 samples represent high-strain granitoids; at the northwestern marginal site, 3 of 6; and at southwestern marginal sites, 1 of 3 samples shows a high-strain fabric. Considering low strain as the other endmember of strain intensity, associated samples occur at all sites of the Yalgoo Dome. Nevertheless, the density of low-strain rocks is highest for the core area with 4 of 8 samples. In the eastern to southeastern mantle- and marginal area, also 4 of 8 samples represent low-strain-conditions. In contrast, the northeastern, northwestern and western sites, which are represented by altogether 19 samples, contain only two samples that are categorized as low-strain; 11 of these 19 samples are high-strain-overprinted. Summarized, High-strain rocks mainly occur at northern and marginal sites, whereas low-strain samples mostly represent southern and central areas of the dome structure.

Regarding temperature conditions, a similar trend can be observed: very high-temperature rocks (>500°C) dominate the central and southern sites, whereas medium to high temperature conditions (300-500°C) mainly represent northern and marginal sites. Within the core-area (also the external southeastern core), 7 of 9 thin sections are very-high-temperature granitoids; only one moderate-temperature-sample occurs within the core, representing a piece of Banded-Iron-Formations (BIF) as greenstone-xenolith. Also all five mantle granitoids were deformed at very high temperatures. At the eastern and southeastern marginal site, 2 of 5 samples comprise very-high-temperature conditions, whereas at northeastern, northwestern and western marginal sites, only one of 17 granitoids reflects very-high-temperature conditions, and 8 samples respectively are categorized as moderate and high-temperature-rocks. Rocks of the northern, southern and southwestern marginal sites have not been sampled.

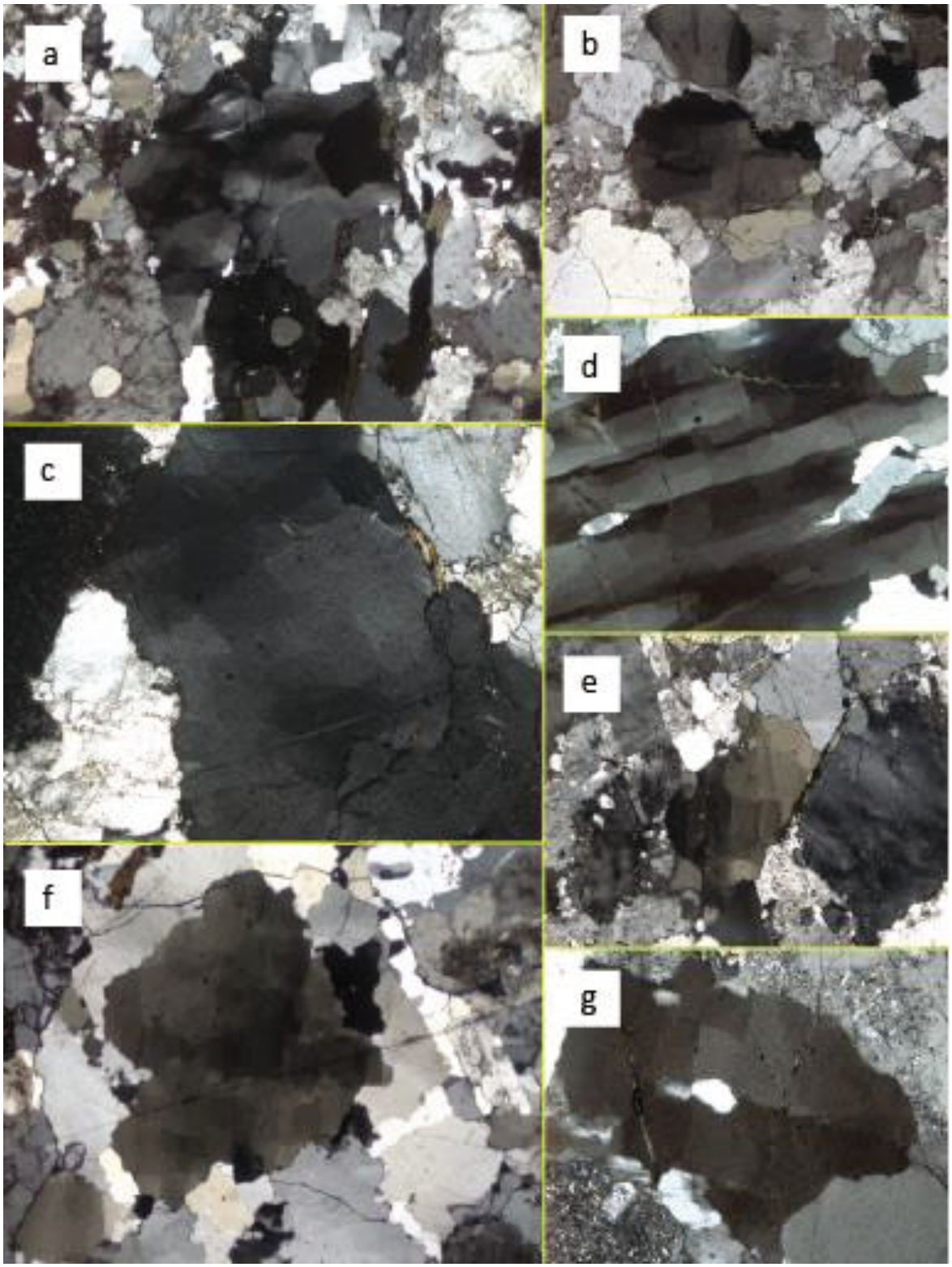

Fig. 25: Quartz chessboard pattern within different very-high-temperature granitoids; a) 155842 (1.44 x 1.08 mm), b) 155827 (0.72 x 0.54 mm), c) 155861 (1.44 x 1.08 mm), d) 155838 (0.72 x 0.54 mm), e) 155861 (1.44 x 1.08 mm), f) 155820 (2.88 x 2.16 mm), g) 155876 (1.44 x 1.08 mm); all tiles in XPL.

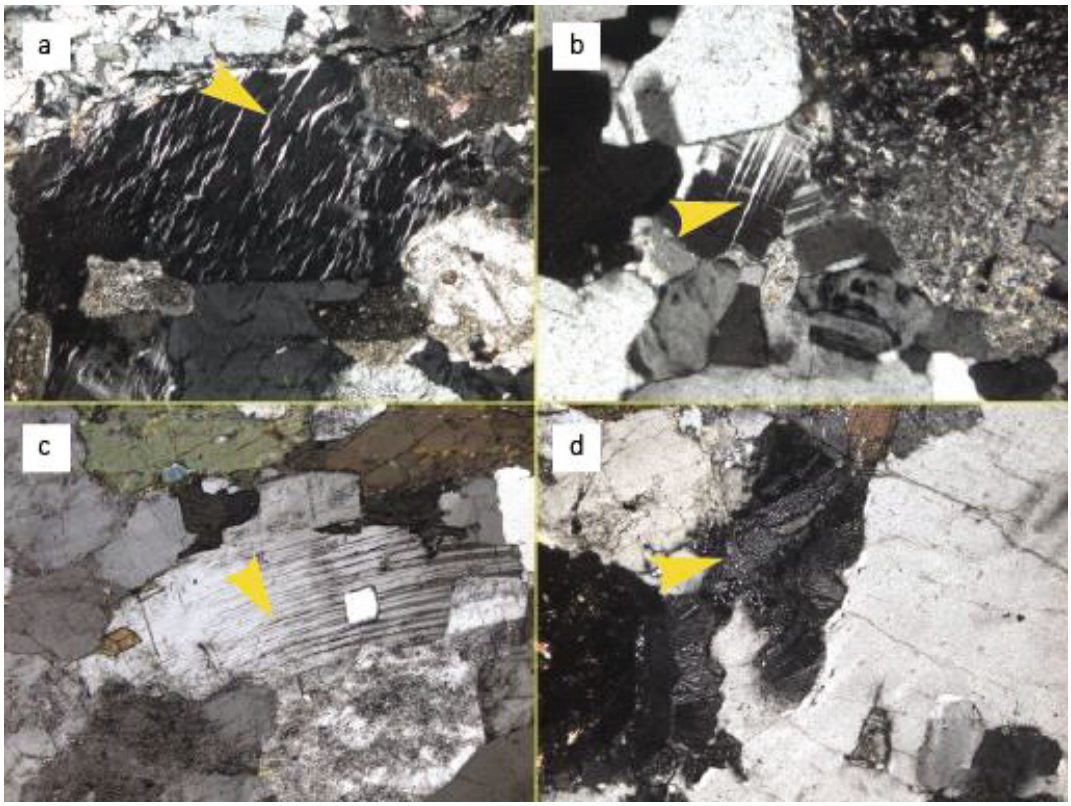

Fig. 26: Solid-state deformation of Feldspar: a) flame perthite (155820, 1.44 x 1.08 mm), b) tapering deformation twinning (155806, 0.49 x 0.39 mm), c) bent twins (155885, 0.72 x 0.54 mm), d) myrmekite (155820, 1.44 x 1.08 mm); all tiles in XPL.

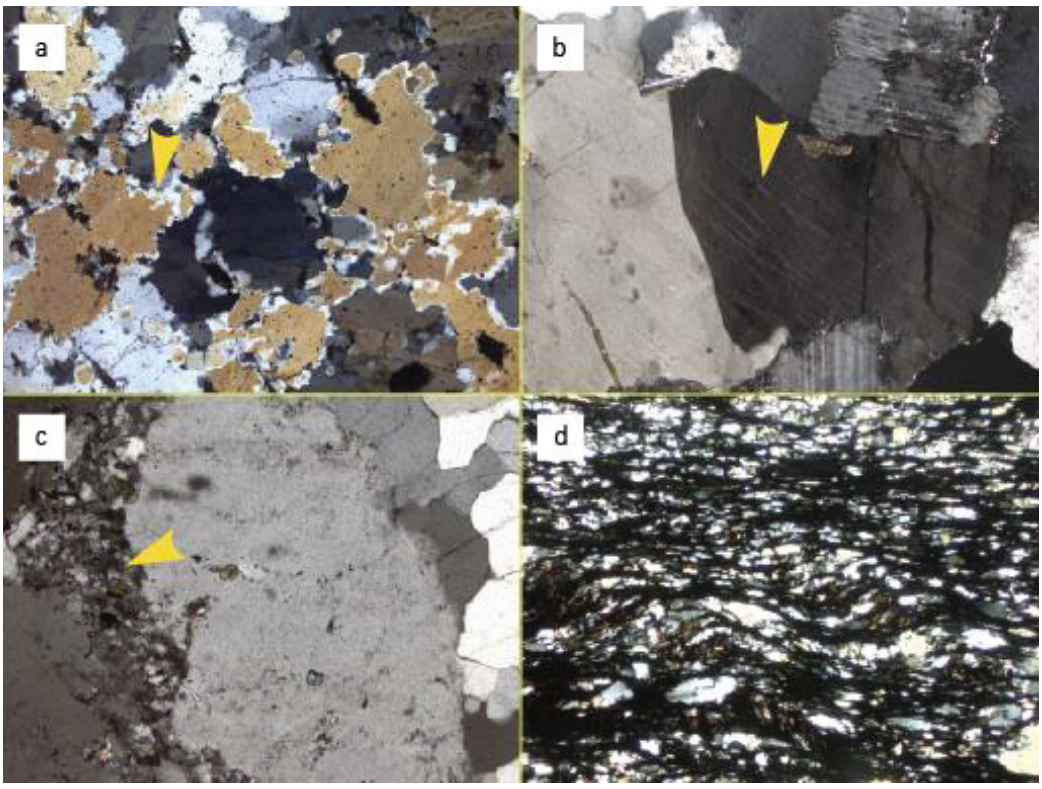

Fig. 27: Quartz deformation signs during relatively low temperature conditions; a) Bulges (210282, XPL, 1.44 x 1.08 mm), b) deformation lamellae (155879, XPL, 1.44 x 1.08 mm), c) small sheared quartz sites, solid-state overprint on magmatic fabric (210275, XPL, 0.47 x 0,36 mm), d) grain size reduction in a lower-T mylonite (210280, PPL, 1.44 x 1.08 mm).

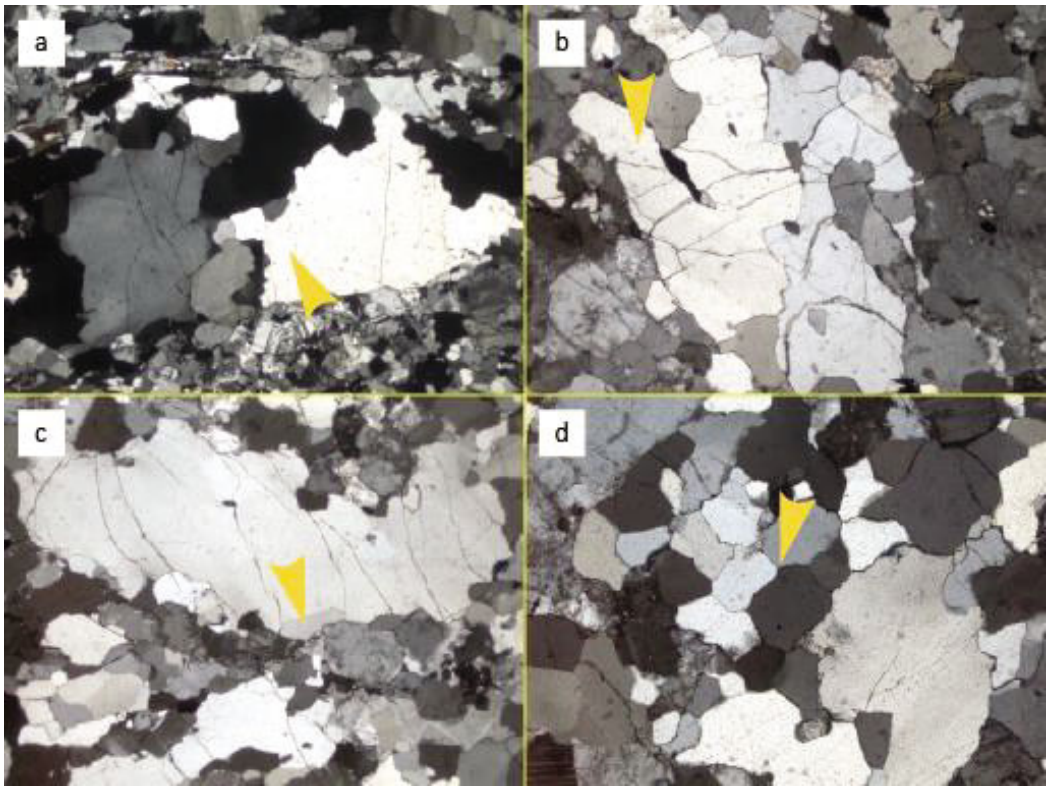

Fig. 28: High-temperature quartz microstructures: a) quartz ribbon with GBM structures (155806, 2.88 x 2.16 mm), b) amoeboid quartz grain (155827, 1.44 x 1.08 mm), c) elongated quartz with sutured boundaries and small recrystallized grains at rim that initially belonged to large central grain (155838, 2.88 x 2.16 mm), d) polygonal grain shape with low-energy dihedral angles of 120°, probably a result of GBAR or initial magmatic fabric (155838, 1.44 x 1.08 mm); all tiles in XPL.

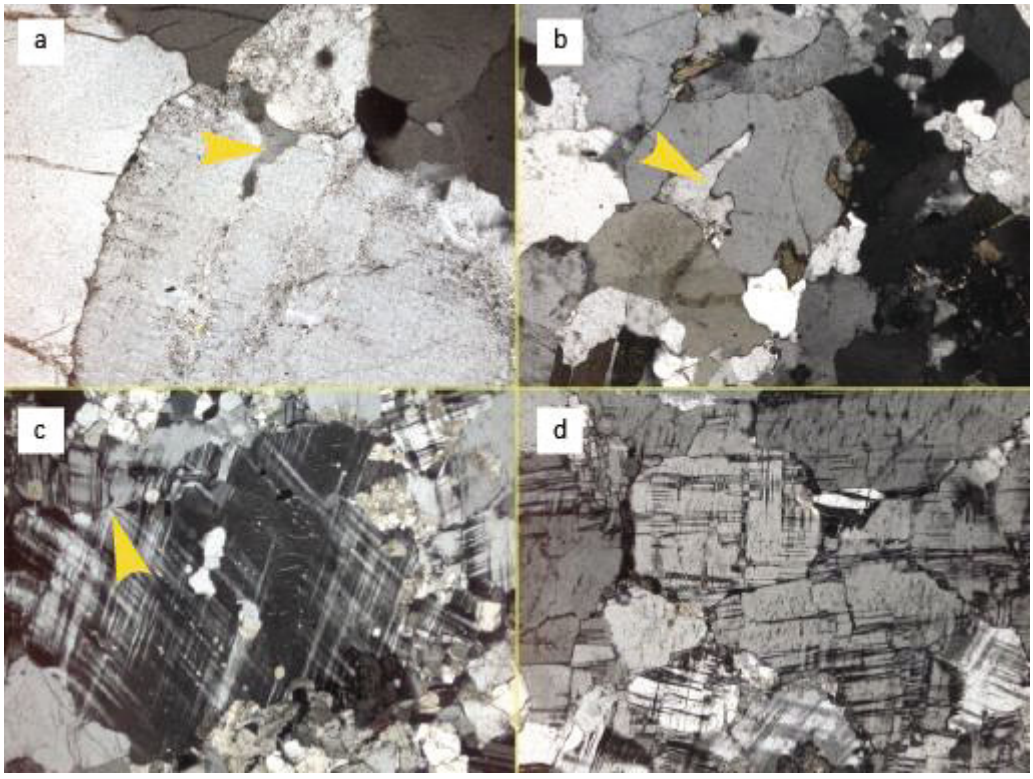

Fig. 29: a) possibly magmatic microfracture (155838, 0.72 x 0.54 mm), b) acute dihedral angle (155879, 1.44 x 1.08 mm), c) c/d) recrystallized microcline grains with tartan twinning and sutured grain boundaries (155871, c: 2.88 x 2.16 mm, d: 1.44 x 1.08 mm); all tiles in XPL.

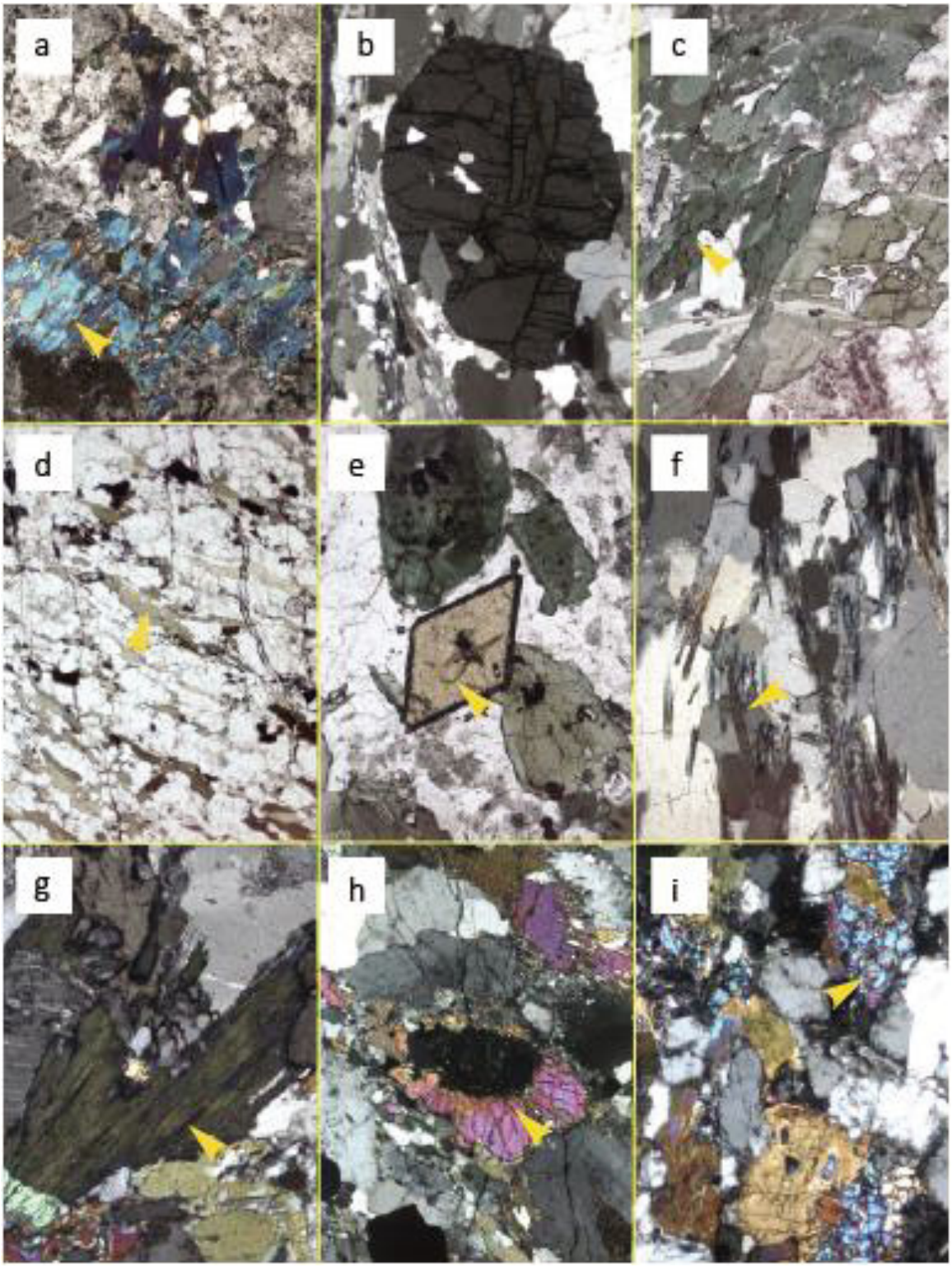

Fig. 30: a) amphibole (155880, XPL, 0.54 x 0.72 mm), b) garnet (155850, XPL, 1.08 x 1.44 mm), c) amphibole with 120°/60° cleavage (155880, PPL, 0.54 x 0.72 mm), d) aligned biotite (210276, PPL, 2.16 x 2.40 mm), e) euhedral titanite (210292, PPL, 1.08 x 1.44 mm), f) fine-grained sillimanite needles (155850, XPL, 0.54 x 0.72 mm), g) abnormal interference color of chlorite (155880, XPL, 0.35 x 0.43 mm), h) epidote with high interference color is fractured by garnet in center (210276, XPL, 1.08 x 1.44 mm), i) amphibole and orthopyroxene (155884, XPL, 0.71 x 0.95 mm).

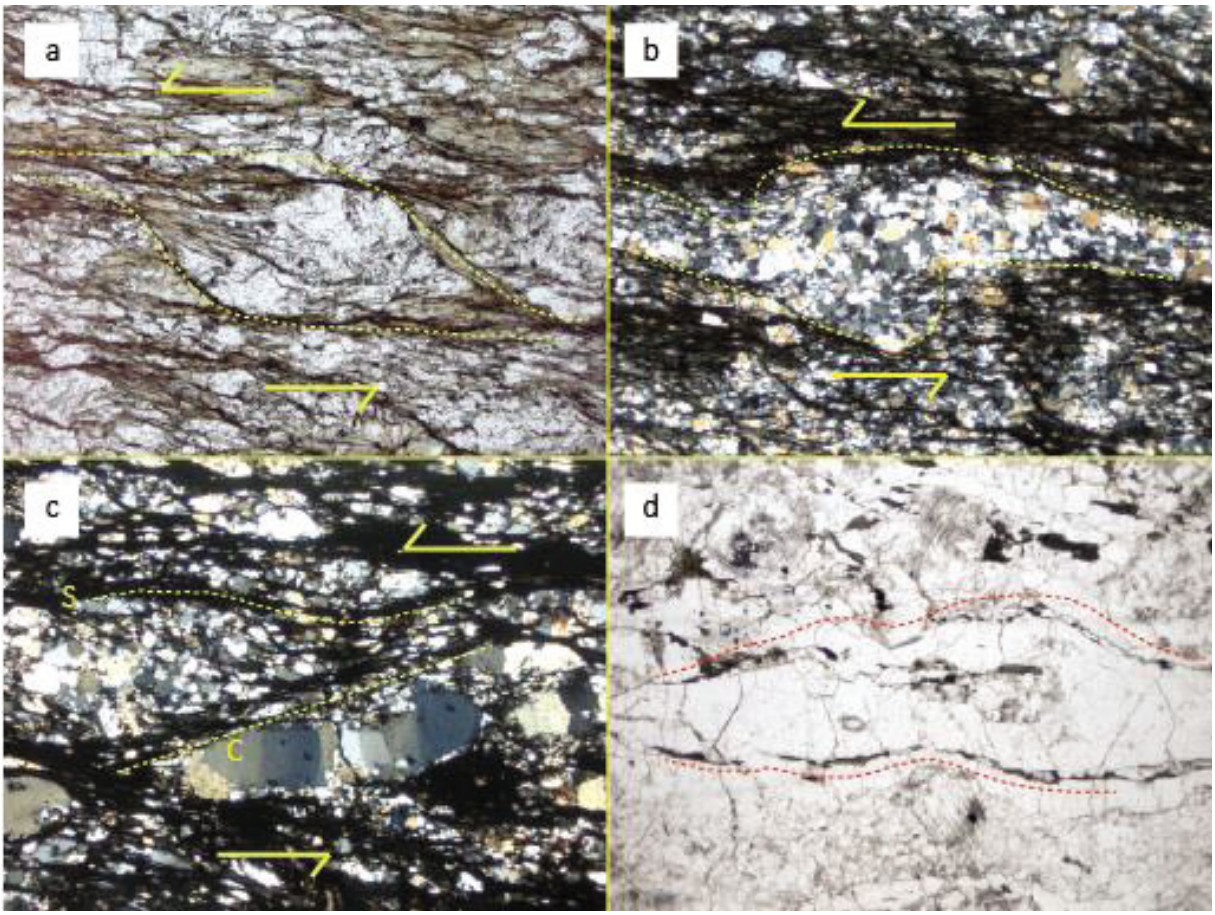

Fig. 31: a) sinistral sigma-porphyroclast (210284, PPL), b) sinistral recrystallized delta-prophyroclast (210284, XPL), c) sinistral shear band (210280, XPL), d) possibly boudinaged quartz ribbon (210297, PPL);
Size of all four images = 1.44 x 1.08 mm.

3.2 Grain Size Analysis

This chapter presents the results derived from the polyLX-Grain-Size-Analysis. Figure 32 shows details of the thin sections, ordered by an approximate Margin-Center-Profile (Table 6), and gives an impression of the textures and grain sizes that have led to the results described below. The overview statistics is attached in the appendix, comprising mean values and the standard deviations for all 8 digitized thin sections (Table A3).

Table 6: Overview table for the localities and the petrography of eight digitized thin sections

Sample Index	**Sample**	**Locality**	**Petrography** (by Ivan Zibra)
1	155806	*marginal (NE)*	granitic gneiss (sheared porphyritic granite)
2	155870	*marginal (SE)*	granitic gneiss (sheared microgranite vein in porphyritic granite)
3	210277	*marginal (NW)*	mylonitized metasiliciclastic rock (fine-grained tonalite)
4	210297	*marginal (SW)*	granitic gneiss (sheared porphyritic granite)
5	155867	*mantle (SE)*	tonalite xenolith (within monzogranite gneiss)
6	155850	*mantle (NE)*	metapegmatite (sheared granitic vein, g-sill-qtz-pl-gneiss)
7	155827	*Core (Yalgoo)*	tonalitic monzogranite-gneiss
8	155876	*core (SE)*	kfsp-granitic-gneiss

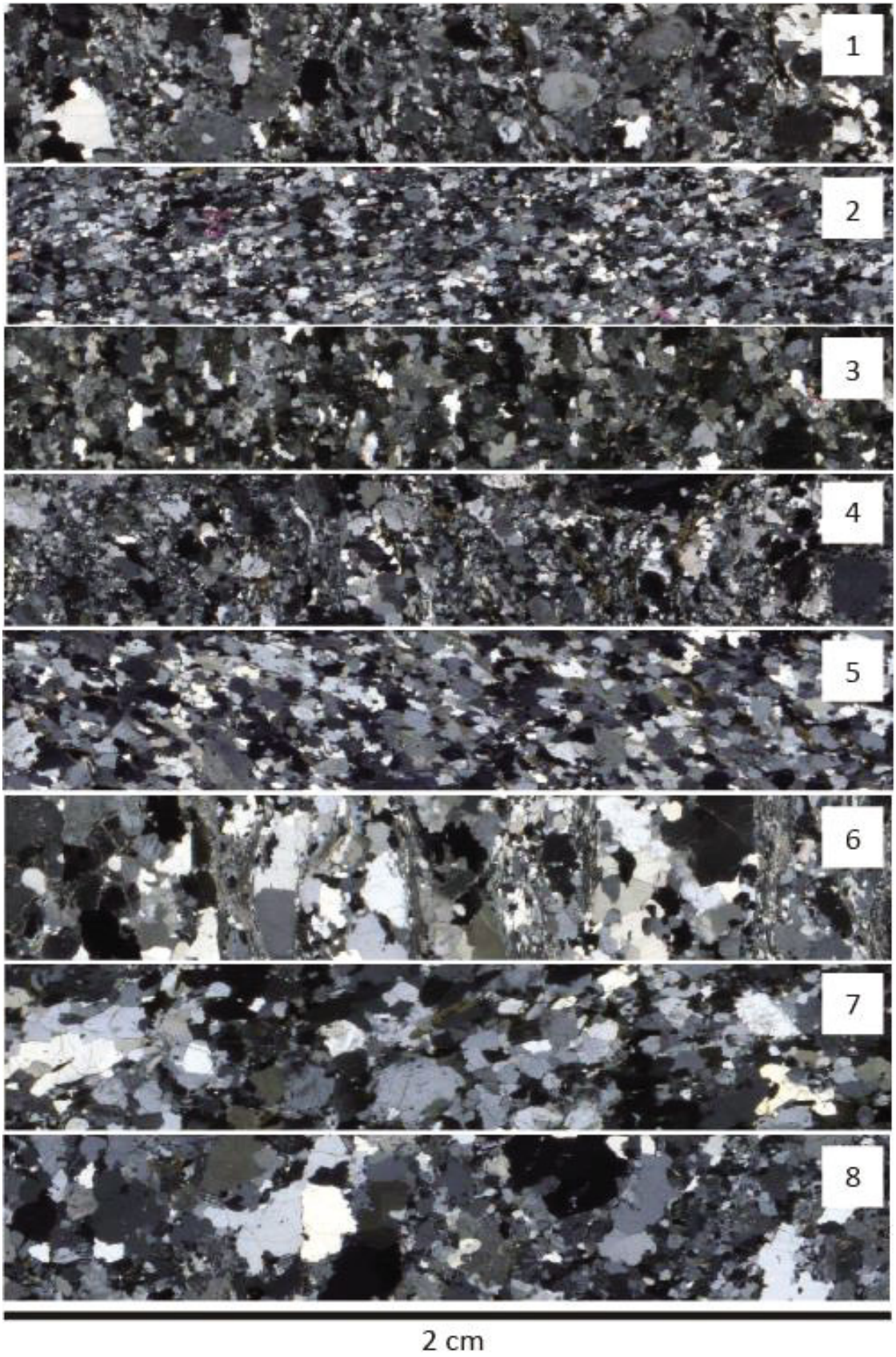

Fig. 32: Details of all eight thin-section scans.

Grain size - Area fraction of Quartz and Feldspar

The area fraction of feldspar mostly exceeds the one of quartz, only for mantle-sample 6 and core-sample 8 the area fraction of both minerals is nearly equal (Fig. 33). The quartz/feldspar ratio is smallest for sample 4 with just 9%, and medium for center-sample 7 with about 60%. All the margin-samples and mante sample 5 show an average area-fraction-ratio of 27%. Thus a weak positive correlation along a margin-center-profile can be determined. The exact mean values of resprectively quartz and feldspar area-fractions can be seen in table A3 (appendix).

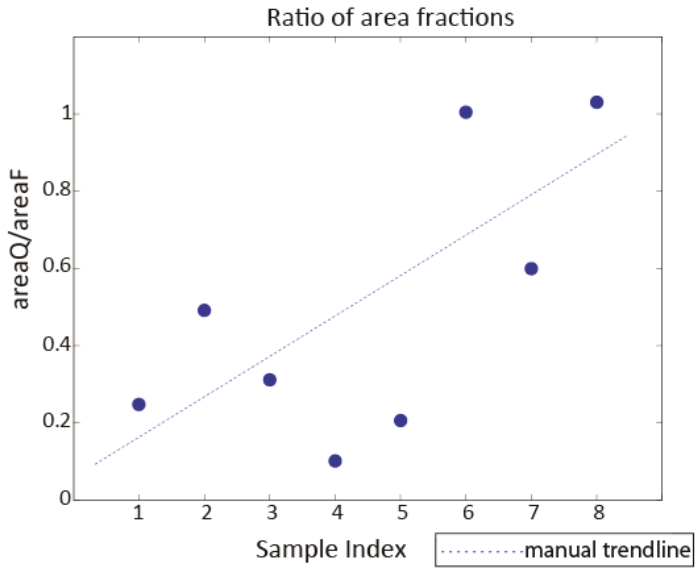

Fig. 33: Quartz/Feldspar - Ratios of area fractions.

Grain size – Equal Area Diameter

The mean Equal Area Diameter (EAD) values of quartz show a clear positive trend: marginal samples show generally smaller grain sizes compared with samples of the dome-center. All marginal samples (1-4) and the SE-mantle sample (5) have an average mean EAD of 339 µm. Within this marginal sector, samples 1 (NE), 2 (SE), 4 (SW) and 5 (SE) also show a weak positive trend comprising slightly larger grain sizes in the south of the dome compared to the north. In contrast, the samples of the NE-mantle (6) and the dome-center (7-8) have an average mean EAD of 790 µm. The core- sample of the small dome (SE) represents the most coarse-grained granite due to quartz grains with a mean EAD of 956 µm, followed by 758 µm and 655 µm for samples 6 and 7 (Fig. 34).

Compared with quartz, the mean EAD values of feldspar show a slightly weaker positive trend from the Margin to the Center. The marginal samples (1-4) range around 426 µm, whereas the mantle and core- samples (5-8) vary around 680 µm. Sample 6 as metapegmatite represents the most coarse-grained rock due to feldspar, with a mean EAD of 876 µm; samples 5, 7 and 8 all range around 600 µm (Fig. 34).

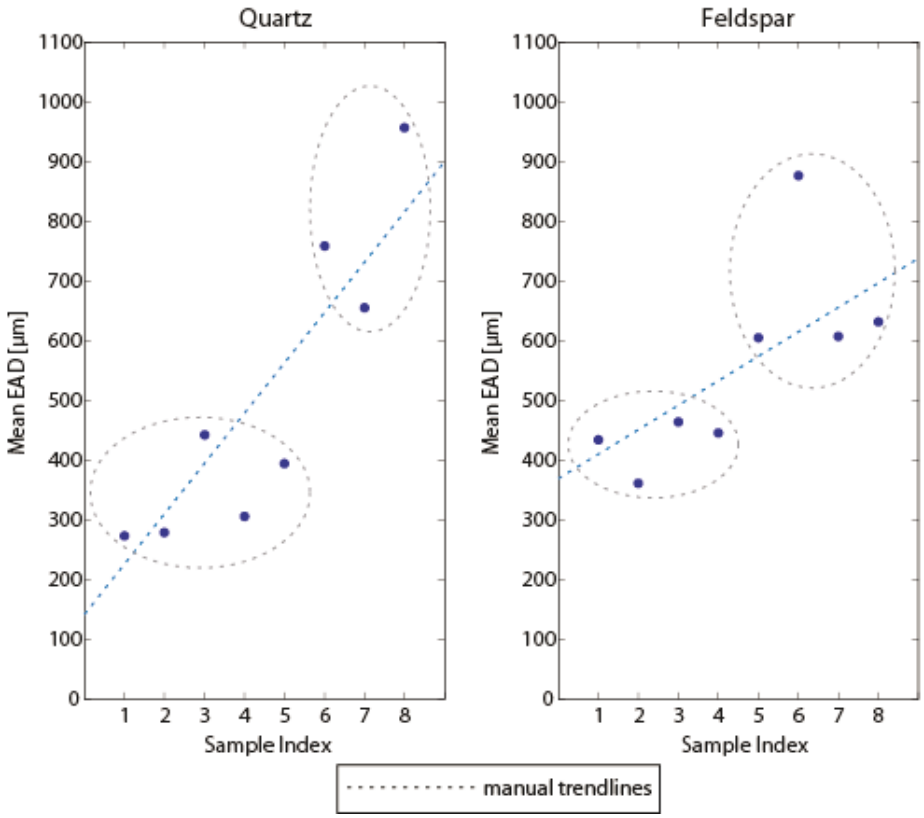

Fig. 34: Mean EAD-values of 8 samples along Margin-Center-Profile.

Overview map "EAD – Equal Area Diameter of Quartz & Feldspar" shows the EAD histograms for quartz and feldspar of all eight samples. Related minimal, maximal, mean values and standard deviations are noted in an excel file; mean and standard deviation are attached in the appendix.

Considering quartz, the marginal samples 1, 2, 4 and mantle-sample 5 show unimodale distributions, with quartz EAD's approximately ranging between 1 and 1200 µm. Sample 3 has a similar range of grain sizes, yet it indicates a weakly pronounced bimodale grain size distribution, with two similar peaks at about 250 and 520 µm. Sample 1 to 5 have relatively small standard deviations of 214 µm in average. The peak of sample 1 (second bin) is especially well defined and enlarged compared to the surrounding bin heights, leading to a positive kurtosis and positive skewness. Mantle sample 6 and the two samples 7 and 8 representing the core form equally widespread EAD distributions with very large standard deviations of 592 µm in average and hence represent a negative kurtosis compared to normal distributions. Their equal size bins comprise EADs between 1 and 1900 µm for sample 7 and between 1 and 3000 µm for samples 8. Sample 6 shows a weakly pronounced bimodale grain size distribution for quartz, with two peaks at about 400 and 1200 µm within a distribution ranging between 2 and 3600 µm.

The feldspar EAD distributions are similar to quartz. Nevertheless the grain size distribution within samples 3 and 6 are unimodale and not bimodale, and the kurtosis of sample 4 and 8 is more positive compared to the associated quartz histograms. In general, feldspar EAD distributions comprise smaller percentages of grain sizes that are coarser than the largest quartz grains of the same thin section. Comparing the mean EAD values of both minerals (red lines in EAD-overview map), the mean EAD for feldspar grains is mostly higher, apart from the two core samples 7 and 8, which show higher mean values for quartz. Moreover, regarding mantle sample 6 and the two core-samples (7, 8), the first equal size bin comprising the smallest group of feldspar-grain sizes is remarkably small compared with the adjacent bin height. This leads to a highly positive skewness characterizing these three samples.

Crystal Size Distribution (CSD)

The α and n_o values gained from the slope and intercept of the CSD-plots are shown in figure 35. The CSD plots of all eight samples were linear. The n_o-differences between all samples are very small.

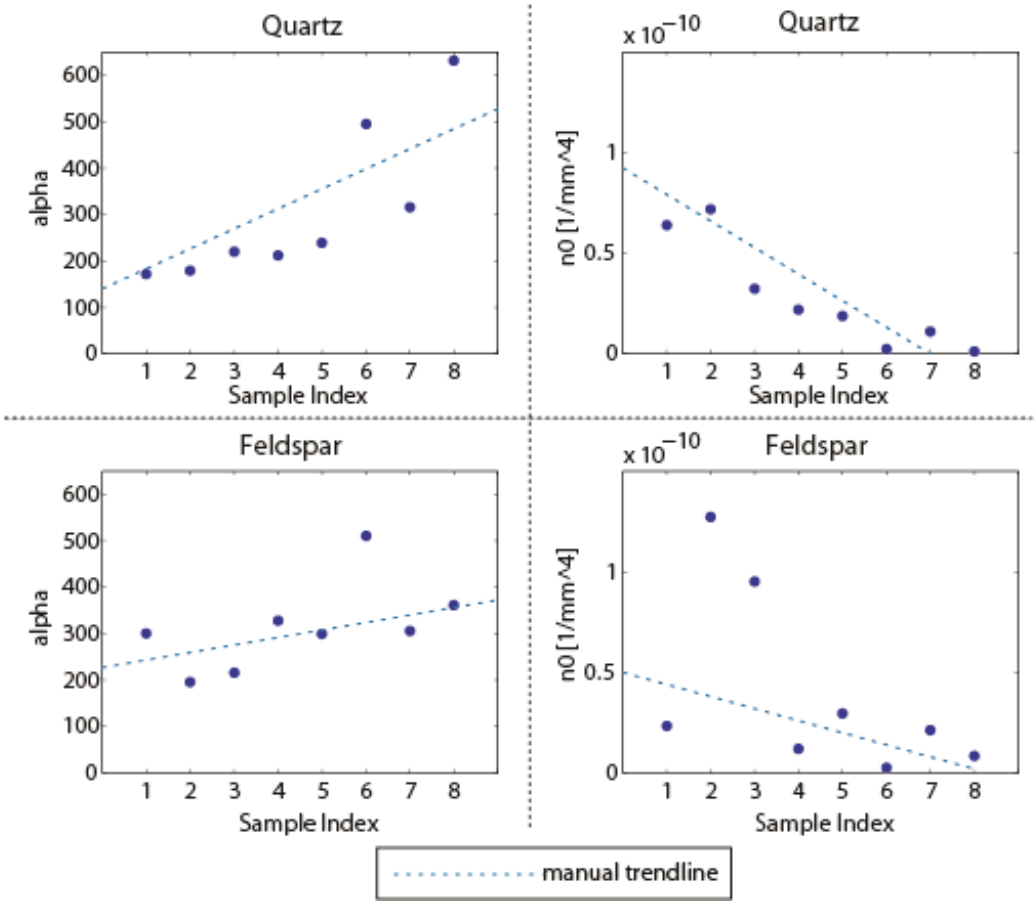

Fig. 35: n_o- and α-values of 8 samples along Margin-Center-Profile; n_o values are given in [10^{-10} mm^{-4}]; α is dimensionless.

It can be seen, that α and n_o correlations with the locality of the rock samples along a margin-center-profile are inverse: the α values increase towards the center, whereas the n_o values decrease. In case of quartz, a well visible positive trend exists for α. Samples 6 and 8 represent the highest α values with 495 and 631, followed by 315 for sample 7. The remaining mantle-/margin-samples have an average α of 204, with a slight internal positive trend. Also for the n_o values, the trend can be well defined and is clearly negative. Minimum values of 0.02 and 0.01 are given for samples 6 and 8, followed by 0.11 for sample 7 and approximately 0.24 for samples 3, 4 and 5, up to maximum values of 0.64 and 0.72 for sample 1 and 2.

Feldspar shows slightly weaker correlations compared to quartz. Sample 6 represents the highest α value of 510, whereas the other samples range around 287 in average. Apart from sample 2 and 3 with n_o values of 1.27 and 0.95, all other n_o values range around 0.16.

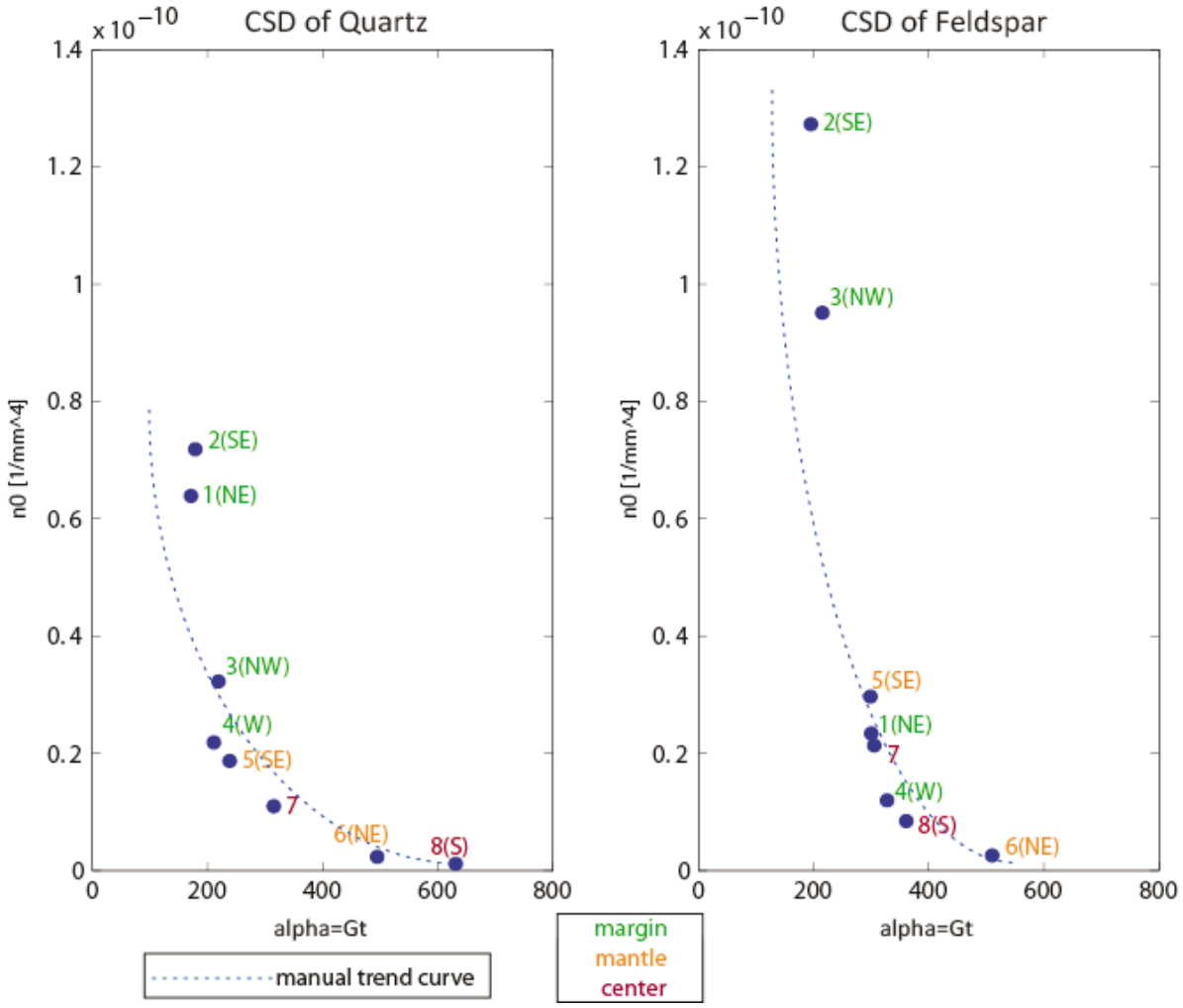

Fig. 36: n_o/α – plot (Lexa, 2003a), based on the CSD results of all 8 samples.

Figure 36 shows the n_o/α- plot as proposed by Lexa (2003a) and which shows the correlation between n_o and α values for respectively quartz and feldspar of all eigth samples. It should be noted that n_o values of Lexa (2003a) range between 2 and 16, and α values range between 0 and 0.25 (Fig. 12). These varieties are distinct from the ranges shown in figure 36.

In case of quartz, a well trend curve is formed by the n_o/α ratios, with marginal samples 1 to 4 comprising higher n_o values and lower α values, and with mantle-/core-samples 5 to 8 representing lower n_o values and higher α values. Sample 6 and 8 both plot in the low n_o/ high α field with an average value of 0.015/563, and thus represent one end of the curved distribution. Sample 1 and 2 plot in the high n_o/ low α field with an average value of 0.679/175, and thus represent the other endmember of the trend curve. Considering only mantle-localities, sample 6 (NE) has a lower n_o/α ratio than sample 5 (SE). Marginal locality-samples 3 (NW) and 4 (W) have lower n_o/α ratios compared to samples 1 (NE) and 2 (SE). Considering only dome-centers, sample 8 (small dome) has a lower n_o/α ratio than sample 7 (Yalgoo Dome).

A similar trend can be observed for feldspar, yet the marginal-, mantle- and core-samples are not as well arranged, compared to quartz. One endmember of the trend curve is represented by sample 6, which plots in the low n_o/ high α field with a value of 0.026/510. Sample 2 and 3 plot in the high n_o/ low α field with an average value of 1.112/206, and thus signify the other end of the curved distribution. The n_o-difference between samples 2 & 3 and the rest auf the point plot is relatively high. Considering only mantle-localities, sample 6 (NE) has a lower n_o/α ratio than sample 5 (SE), similar to quartz. In view of only marginal localities, samples 1 (NE) and 4 (W) have lower n_o/α ratios compared to samples 2 (SE) and 3 (NW). Also for feldspar, the dome-center of sample 8 (small dome) has a lower n_o/α ratio than the one of sample 7 (Yalgoo Dome).

Grain shape –Elongation

The elongation of quartz crystals (Fig. 37) shows no clear positive or negative trend along a margin-center-profile. On the first view, the long axes of quartz and feldspar grains are generally twice as long as the short axes. Sample 1 and 6 have the highest mean elongation values of approximately 2.57, sample 2 and 5 have the lowest mean elongation of about 2.00 and the remaining samples range around 2.27. Regarding feldspar, all mean elongation values closely range around 2.11, apart from sample 5, which shows a slightly lower value of 1.96. The average elongation of quartz is slightly higher than the one of feldspar.

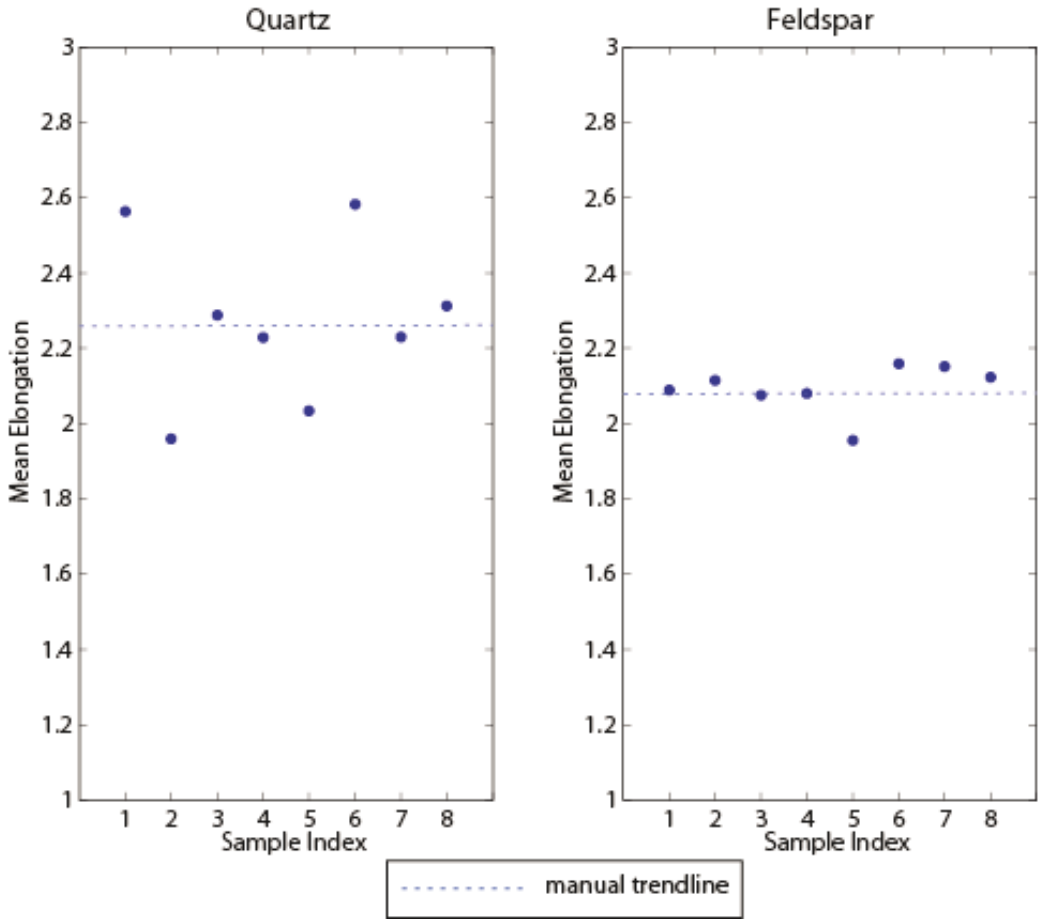

Fig. 37: Mean Elongation-values of 8 samples along Margin-Center-Profile.

Grain shape – Roundness

Due to the mathematically inverse correlation between elongation and roundness, the point distribution is also quite similar, but inverse (Fig. 38). Regarding quartz, sample 1 and 6 show the lowest mean roundness values of about 0.46, sample 2 and 5 represent the highest mean roundness of approximately 0.52 and the remaining samples range around 0.50. The circularity values plot with a comparable systematic between 0.50 and 0.60. The mean feldspar values all range around 0.53.

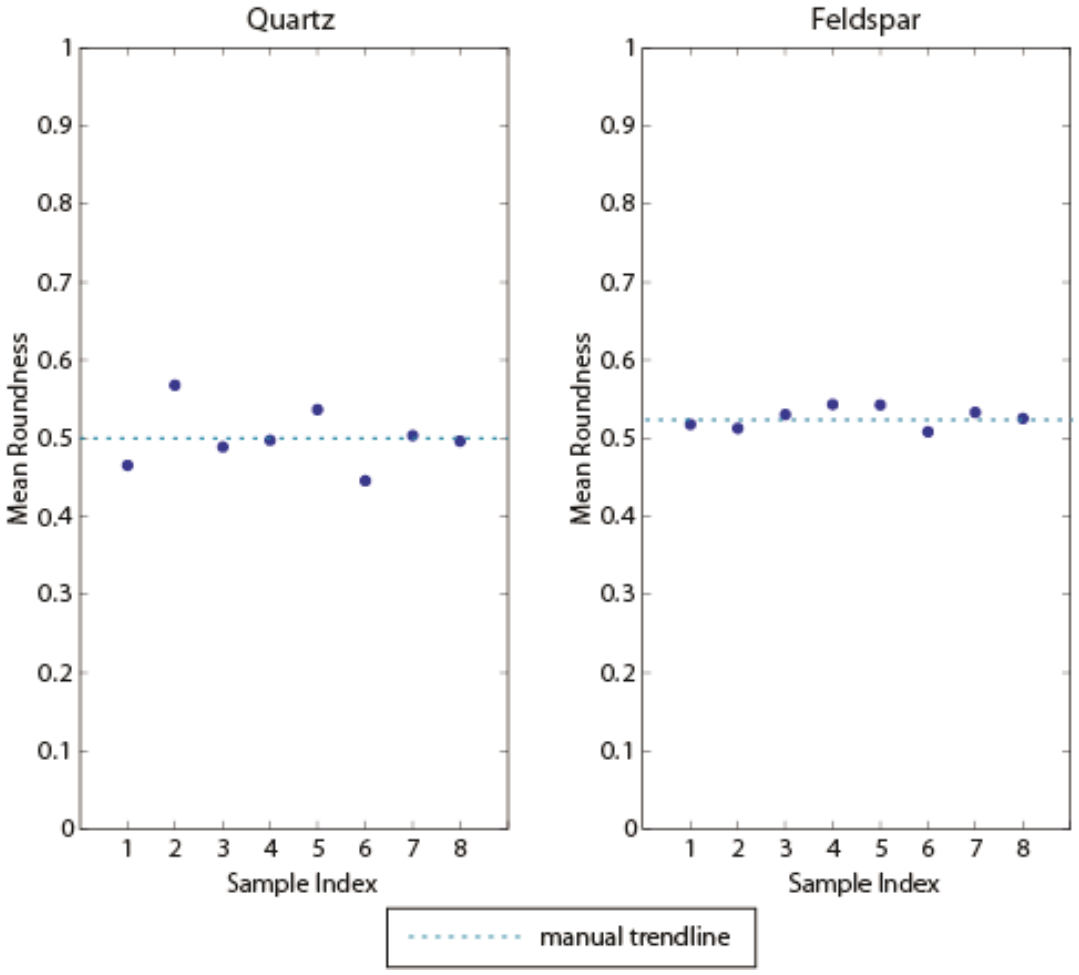

Fig. 38: Mean Roundness-values of 8 samples along Margin-Center-Profile.

Grain orientation

Figure 39 shows the mean long axis orientations (LAO), which have been determined from all eight thin sections. The red line represents the reference orientation with an orientation of 90° from the vertical direction. On the first view, quartz and feldspar grains of all samples are arranged not far from this reference foliation. Starting with quartz, the orientation angles of samples 1, 5, 6 and 8 slightly deviate from the reference foliation ranging around 88° in average. The remaining samples show orientation angles of about 106°. Regarding feldspar, samples 1, 2, 3, 5 and 6 closely range around the reference foliation with a mean orientation of about 92°, sample 4 has the largest orientation angle with 102° and the core-samples 7 and 8 show the smallest orientation angles with 76°.

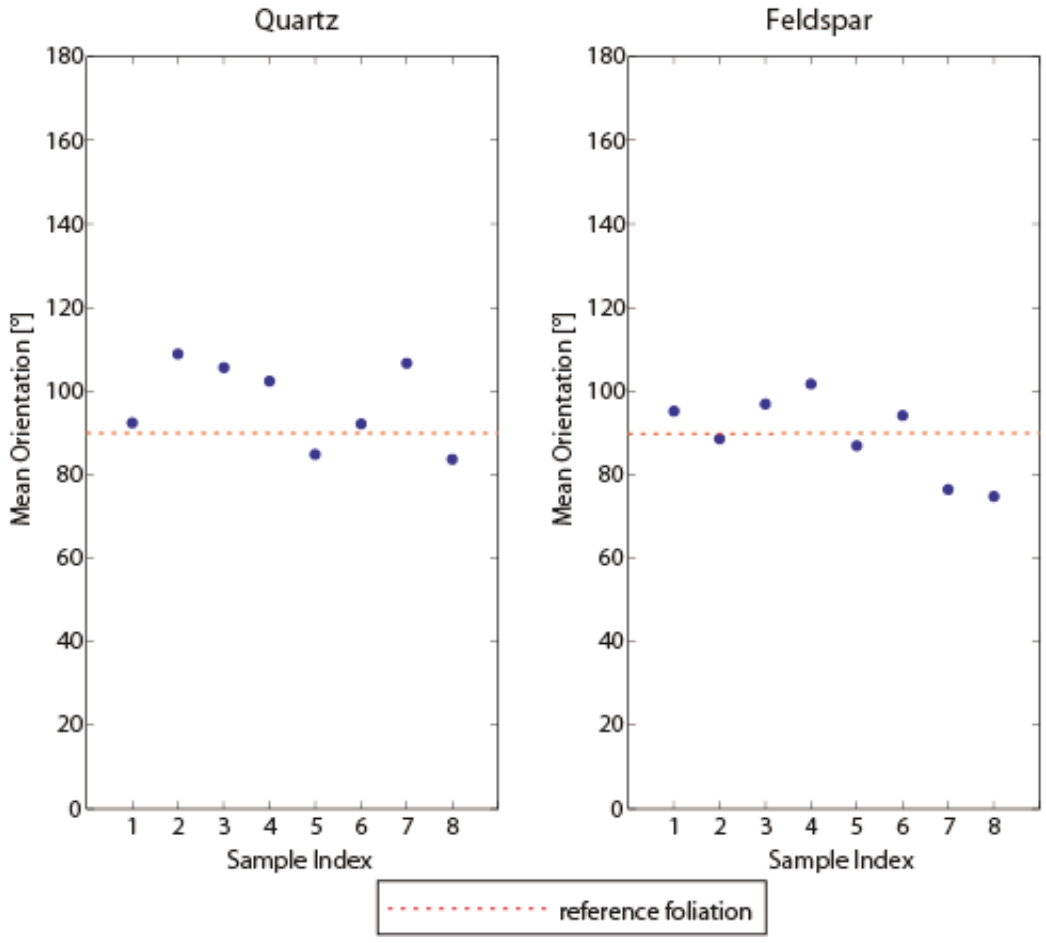

Fig. 39: Mean orientation (LAO)-values of 8 samples along Margin-Center-Profile.

The long axes orientation distributions are shown in overview map “LAO – Long axis orientation (rotated) of Quartz, Feldspar & Mica”. In case of quartz, marginal samples 1 (NE) and 3 (NW) and mantle-sample 6 (NE) show well defined LAOs with small standard deviations of ± 10°; samples 4, 7 and 8 (center) show moderate standard deviations of about ± 15°/± 20°. For samples 2 (margin, SE) and 5 (mantel, SE) high standard deviations of about ± 30° are determined, indicating an only weakly pronounced elongation direction of quartz grains within the rock.

Regarding feldspar, the long axes orientations of all samples are quite well defined with small to medium standard deviations between approximately ±10° and ± 20°, apart from mantle sample 7, which has an extremely wide standard deviation of about ± 45°.

The mica orientations are derived from a very small number of grains and thus, they are statistically unserviceable. However, they show equal long axis orientations compared to quartz and feldspar, verifying their determined mean LAO, except from sample 6, which shows a clear misorientation of approximately 60° between mica and quartz/feldspar LAOs. For the marginal samples 3 (NW) and 4 (SW) and the central samples 7 and 8, relatively high standard deviations of mica LAOs have been determined. The remaining samples show clear mean mica orientations with smaller standard deviations.

3.3 Crystallographic Preferred Orientation (CPO)

Within this chapter, the CPO plots of all 36 thin sections are described, pointing at their associated maxima positions within the stereographic projection. The FA-results and their associated localities within the Yalgoo Dome are shown in the overview map "CPO (Quartz)". It is structured into four subareas (Table 7).

Table 7: Subareas of the Yalgoo Dome representing different CPO patterns

1	*Center*	**a**: center of Yalgoo Dome **b**: center of small Dome (SE)
2	*Mantle*	**a**: north **b**: southeast
3	*Eastern margin*	**a,b**: northeast **c**: east **d**: southeast
4	*Western margin*	**a,b**: northwest **c**: west **d**: southwest

Area 1 – the center

Eight thin sections represent the core of the Yalgoo Dome (1a) and one thin section (155876) represents the central part of the small culminating dome in the southeast (1b). The latter comprises a CPO pattern with a clear point maximum in X-direction at about 90° from the vertical direction indicating prism<c> slip, and thus, the dominating crystallographic preferred orientation lies subparallel to the reference foliation and lineation. Slightly smaller accumulations of c-axis can also be seen at an oblique position between X and Z direction (combined slip systems) with a dip direction of approximately 130° and some axes scatter around Z at 180° (basal<a> slip). A very weak accumulation is located nearly parallel to Y indicating minor prism<a> slip.

The CPO patterns of area (1a) are not very similar to each other and most of them show different maxima positions. Thus, it is not easy to elaborate a general description. Thin sections 155827, 155831 and 155879 shows modifications of girdle patterns, yet they include distinct point maxima within the girdle: 155827 shows marginal point maxima subparallel to the Z-direction within an oblique girdle pattern striking at about 170° ; fewer c-axis scatter close to the X- and Y-direction. 155831 shows a slightly oblique crossed-girdle-type-I pattern striking at about 160° and including four point maxima. Two of them are on intermediate (rhomb<a> slip) position within the Z-plane with one maximum also close to the Y-direction

(prism<a> slip). The other two point maxima occur closer to the X than to the Z direction on marginal position, probably combining components of basal<a> and prism<c> slip. 155879 shows a weakly pronounced oblique single girdle at about 60° (several slip systems) with a dominant point maximum in intermediate rhomb<a> slip-position; this maximum lies close to the X-plane indicating a component of prism<c> slip.

The remaining core samples show marginal maxima and a remarkable minor number or even 'lack of' c-axes close to the Y-direction; only 155883 comprises axes in this direction. 155883 and 209689 form two marginal point maxima respectively in an oblique direction between Z and X (combined basal <a> and prism<c> slip): 155883 strikes about 140°, with a minor maximum on intermediate (rhomb<a> slip) to central position (prism<a> slip). 209689 shows elongated marginal point maxima striking between 0° and 40°. In contrast, 155880, 155884 and 155885 all show four point maxima in marginal position between Z and X direction within each quadrant (component of basal <a> and prism<c> slip). In case of 155880 and 155884, the 4 point maxima seem to be two stretched 'double-maxima'; for 155880 they range around the X-direction and for 155884 they range around the Z-direction. Both show opening angles of about 60°. The opening angles of sample 155885 are quite large with about 120° and thus, the point maxima trend more in the X-direction.

Area 2 – the mantle

The samples 155850 and 155842 represent the northern/northeastern mantle area 2a. 155850 shows clear marginal point maxima subparallel to the X-direction, indicating dominant prism<c> slip. 155842 shows one dominant marginal point maxima subparallel to the Z-direction indicating dominant basal<a> slip, and 3 smaller minor point maxima; two of them occur at marginal sites between Z and X, involving an additional component of prism<c> slip, and the minor third c-axes accumulation is located on an intermediate to central position.

The mantle-site 2b in the Southeast is represented by samples 155861, 155867 and 155869. 155861 and 155867 show elongated and marginal double-point maxima; again the Y-maximum is missing. In case of 155861, the maxima trend in Z-direction with a small opening angle of 30°. For 155867, the double maxima strike approximately 135°, with one component trending subparallel to X-direction (dominant prism<c> slip) and the other more minor component points in Z-direction (dominant basal<a> slip). 155869 is characterized by a slightly oblique girdle pattern trending in Z-direction, with dominant c-axes accumulations an marginal and intermediate position indicating both basal<a> and rhomb<a> slip. A small minor maxima occurs subparallel to Y.

Area 3 – Eastern Margin

The northeastern marginal area 3a is represented by the samples 155806, 155836, 210216a/b, 212730, 212731, which all show clear Z-maxima. The point maxima of 155836 are stretched and thus comprise a marginal site over 40° around the Z-direction; additionally, one part comprises also c-axes accumulations on intermediate to central position. The c-axes distribution of 155806, 212730 and 212731 are nearly girdle-like with dominant point maxima on marginal to intermediate position (basal/rhomb<a>) with a minor component subparallel Y (prism<a> slip). 210216a shows slightly oblique marginal point maxima striking about 160°; weaker pronounced c-axes accumulations occur on marginal site striking at about 30° and also subparallel to the Y-direction. The two marginal point maxima form an opening angle of about 50°. Sample 210216b also shows a slightly oblique pattern striking at about 20° and comprising an elongated point maximum on intermediate position with a dip direction of approximately 200°; minor components occur at marginal and central sites (basal/rhomb/prism<a> slip).

The subarea 3b is characterized by the three samples 155819, 155820 and 155822, with two of them comprising a dominant Y-maximum: 155819 shows a clear Y-maximum indicating dominant prism<a> slip and minor components close to the Z-direction on marginal sites. 155822 shows a clear single girdle within the Z-plane with a dominant maximum parallel Y and minor components on marginal and intermediate positions, indicating an activation of all slip systems in <a> direction, yet with the prism-plane as main slip plane. In contrast, sample 155820 shows only minor c-axes accumulations subparallel Y; it is dominated by a single point maximum on marginal to intermediate position (basal/rhomb<a> slip), slightly oblique from the Z direction, with a point-maximum-'tail' near the X-direction.

The western margin of the Yalgoo Dome (3c) is represented by the two samples 155838 and 155839, which both show dominant Z-maxima. The former shows clear marginal point maxima parallel Z with minor components on intermediate to central position. The latter is characterized by slightly oblique double-point-maxima on marginal sites with an opening angle about 30°; one pair strikes in Z-direction and the other pair strikes at 150°. A weakly pronounced c-axes maximum also occurs parallel Y.

The southwestern margin of the Yalgoo Dome (3d) is represented by the three samples 155857, 155870 and 155871 trending towards Z. The two latter samples have similarly looking CPO patterns with a remarkable lack of c-axes close to the Y direction; stretched marginal point maxima comprising sites over nearly 90° are dominant. For 155870, the pattern is oriented oblique at about 45° and thus comprises components parallel Z (basal<a> slip) , X (prism<c> slip) and between both; for 155871, the pattern ranges around the Z-direction, yet

weakly pronounced ‘tails’ occur close to the X-direction. Sample 155857 shows an oblique girdle-like pattern striking close to Z at approximately 30°, comprising dominant point maxima on marginal and intermediate position indicating basal<a> and rhomb<a> slip.

Area 4 – Western Margin

The northwestern marginal area (4a) close to the greenstone belt is represented by the four samples 210277, 210280, 210282 and 210284, whose CPO patterns differ from the northeastern samples. 210277 and 210282 show comparable maxima positions, with a clearly visible c-axes accumulation on marginal to intermediate position striking slightly oblique from the Z direction. Additionally, 210277 shows a relatively well pronounced maximum parallel to Y, which is just very weakly visible for 210282. Both samples also show highlyoblique marginal components striking close to the X-direction. For 210277, this X-component looks like an additional minor point maxima, whereas for 210282, it is just represented by ‘tails’ surrounding the main point maxima. 210280 is characterized by four marginal to intermediate point maxima within each quadrant, forming a large opening angle of about 70°. Thus, they are oriented oblique between the X and Z direction. The most dominant point maximum has a dip direction of about 320°. 210284 shows an oblique and bended girdle-pattern striking about 140° between X and Z direction, with minor marginal point maxima and a dominant maximum on intermediate position with an approximate dip direction of 180°.

Subarea 4b is also part of the northwestern marginal area, but located farer from the greenstone belt and closer to the mantle area. The two samples 210275 and 210276 show slightly oblique CPO patterns with dominant marginal point maxima close to the Z direction. 210275 strikes about 160° and shows a lack of c-axes subparallel Y. 210276 strikes about 30° and additionally it contains minor components subparallel X and Y.

The marginal site 4c (west) is represented by the sample 210292 and site 4d (southwest) is represented by sample 210297. The former is characterized by a displaced girdle-like pattern, comprising marginal to intermediate large point maxima covering a site over 60° around the Z direction (basal/rhomb<a> slip). Minor c-axes accumulations occur between X and Y direction with a dip direction ranging around 270°. The latter is characterized by a clear single point maximum on a slightly oblique intermediate position between Z and Y, with an approximate dip direction of 210°.

4 Discussion

4.1 Interpretation of microstructures and field data

The microscope observation of all thin sections comprise recrystallization structures reflecting upper greenschist (<400°C) to lower granulite (<800°C) thermal conditions; no real low-temperature signs could be found. Thus, all crustal parts of the archaic Yalgoo Dome were heated during deformation. Possibly, the thermal gradient of archaic crust was generally higher, related with higher temperatures of the ambient mantle, intense magmatic activity and higher radioactive heat production (Martin, 1986; Bickle, 1978). Maybe deformation started soon after the formation of the crust and thus, the timespan of cooling was short und the young felsic crust still heated. Another explanation for the high-temperature tectonics could be that the tectonic mechanism shaping the Yalgoo Dome produced heat. Nevertheless, it should be noted that this estimation of temperature conditions based on dynamic recrystallization structures is not clear evidence for thermal conditions, as the recrystallization mechanisms are also influenced by the water content, as described in chapter 2.1.2, even though the water content of archaic crust is assumed to be quite low (Korenaga, 2008).

Considering the spatial temperature-strain distribution (Fig. 24) that has been suggested in chapter 3.1, especially the central and southeastern mantle sites of the roundish Yalgoo-structure are characterized by very high temperature deformation (>500°C), partly melt-present-conditions, and low to moderate strain rates. Common chessboard pattern in these rock samples indicates that they were deformed in the thermal transition zone between the low-quartz field and high-quartz field (chapter 2.1.1). The temperatures of the low-high-quartz transition range from ~573 °C at 1 bar to ~825 °C at 10 kbar (Van Groos & Heege, 1973). This could be evidence for a local heating event affecting the central parts of the Yalgoo Dome additionally to its deformation, or the deformation itself heated the core-area. In contrast, the marginal areas comprise slightly lower temperature conditions (300-500°C) and higher strain rates; at the northwestern margin, mylonites occur, showing SC' shear bands, which indicated high-grade shearzones. This could indicate that the deformation event shaping the Yalgoo Dome led to strain accumulation at the contact zone between granitoids and greenstones. The shear senses determined close to the granitoid-greenstone-contacts of the Yalgoo Dome indicate vertical tectonic processes, comprising upward shearing of the granitoids and downward shearing of the greenstones (Fig. 23). Subvertical lineations also indicate dominant vertical tectonics (Foley, 1992). The foliations mostly strike subparallel to the greenstone belt (Fig. 22), underlining that the two petrological entities were simultaneously deformed. Extensional components like boudinage, which have been

found in the field, hint at an extensional regime accompanying the vertical tectonics. The spatial temperature-strain distribution and shear senses would suggest an up-doming mechanism.

Within the tonalitic core, the content of mafic minerals is higher, as the chemical composition of a tonalite is more basic and mafic compared to classic granite. Thus, on aeromagnetic images, not only the greenstone belt, yet also the core area are conspicuous (Fenwick, 2014). A higher content of mafic material is also suggested for the archaic lower crustal layer: Seismological studies of the archaic crust show that the lower crustal layer commonly is more reflective, which is explained by a higher content of mafic material and also by the transition of lower-grade granitic gneisses to higher-grade granulitic gneisses (Drummond, 1988 and references therein). Thus, the tonalitic core of the Yalgoo Dome might be a relic of a lower archaic crustal layer buried under thick greenstones, and hence it probably has ab initio been a higher-grade rock before it has been again deformed at high temperatures. One rock sample of the core represents Banded Iron Formations (BIF) of lower metamorphic grade, compared to the other core samples. BIF with a high content of mafic minerals typically occur as part of greenstone layers. This xenolith might be a relic of a greenstone-over-tonalite crustal sequence before the younger monzogranite intruded. A large dextral strike-slip fault in the core-area indicates that also horizontal shear zones affected some parts of the dome.

Most of the very-high-grade granitoid rocks, which possibly metamorphosed during melt-present deformation or during primary crystallization, additionally show moderate-temperature and solid-state deformation signs. Thus, it can be presumed that deformation of the rocks continued during cooling, or that a second deformation event at lower temperatures overprinted the dome structure.

4.2 Interpretation of the Grain-Size-Analysis

It should be noted, that different average grain sizes within the eight samples are not only depending on dynamic recrystallization and annealing processes leading to an overall grain-size reduction or coarsening; the final grain size also depends on the initial grain size within the particular protolith. Thus, it should be considered that the small grain sizes of marginal sample 2 might be related to its initial state as microgranite, and the large grain sizes of mantle sample 6 might be related to its initial state as pegmatitic vein.

However, the clear positive trend of grain sizes along a margin-core-profile is not assumed here to be totally accidental: The average grain size considerably increases along a margin-mantle & center-profile with EAD values between 300 µm to 1000 µm, indicating higher

temperatures within central sites of the dome compared with marginal sites. The standard deviations of EAD distributions are higher for mantle and especially core-samples, hinting at intensive dynamic recrystallization mechanisms leading to a grain size reduction on the one hand (SGR), and to coarsening on the other hand (GBM, GBAR). These mechanisms occur during high-temperature deformation exceeding 400 °C (Stipp et al., 2002; chapter 2.1.2). The weakly pronounced bimodale grain size distributions of sample 3 and 6 also point at dynamic recrystallization mechanisms and the competition between grain size reduction and coarsening. For both core-samples the area fraction of quartz exceeds the one of feldspar, confirming the role of coarsening and annealing effects at very high temperatures. However, this total area relationship between quartz and feldspar also depends on the chemical composition of a rock and the initial size of the quartz feldspar grains: The mean feldspar EAD of the sample representing the tonalitic core probably is ab initio lower, compared to the monzogranite-mantle-samples, as tonalites mainly contain plagioclase and rarely alkali feldspar. The latter tends to form larger crystals compared to plagioclase. Monzogranites have a higher content of alkali feldspar.

The frequency of very small feldspar grains is relatively low, compared with the frequency of larger grain sizes, especially in mantle- and core-sites. This possibly confirms that low-temperature brittle fracturing and cataclastic flow, which 'crush' grains, have not been common. Marginal samples 2 and 3 show a typical normal-distribution of EADs; all other frequency histograms differ from this ideal grain size distribution, confirming the influence of dynamic recrystallization. The shape of both quartz and feldspar EAD histograms are relatively equal, which could eventually pronounce an overall high-temperature distribution within the Yalgoo Dome, leading to dynamic recrystallization of both quartz and feldspar.

In case of annealing effects influencing the grain size distribution, a bell-shaped Crystal Size Distribution plot would be expected (Cashman & Ferry, 1988), as described in chapter 2.2.2. However, all the CSD plots are linear, just as the CSD plots described by Lexa (2003a), who explains this with the absence of annealing effects due to rapid cooling after deformation. However, this explanation is possibly not valid for the Yalgoo-Dome, as the presence of enlarged and polygonal quartz grains is probably connected with annealing, unless these grain shapes are relics of an initial magmatic fabric. Within the n_o/α plot shown in Lexa (2003a), all Yalgoo-sample values presented in figure 36 represent an extreme endmember in the low n_o / high α field: the n_o values of the plot presented in this thesis are a lot smaller - and the α values are a lot larger than those of Lexa's (2003a). As described in chapter 2.2.2, this extremely low n_o/α ratio represents very high temperatures and relatively low strain rates. This confirms the theory of a higher geothermal gradient in the Archean or a large thermal anomaly accompanying the formation of the Yalgoo Dome. The internal distribution of all eight Yalgoo-samples within the n_o/α plot of quartz shows, that mantle samples have

lower n_0/α ratios compared to the marginal samples. Considering the role of dynamic recrystallization, higher temperatures and lower strain rates are again suggested for central sample localities, whereas marginal sites comprise slightly lower temperatures and higher strain rates (Bell & Hickey, 1999). The different positons of marginal/mantle/core samples within the n_0/α plot could also be explained by different states of annealing and the trend to final textural equilibrium at the curve's center (Cashman & Ferry, 1988). A similar trend can be observed for feldspar, yet marginal to central samples are not as well sorted as the quartz-CSD values, which shows that quartz is more influenced by dynamic recrystallization than feldspar.

The mean values of Elongation and Roundness do not show a clear trend along a margin-center-profile. The grains are elongated, especially quartz, which is due to dynamic recrystallization and the influence of directional strain at high temperatures. The elongation of grains at all marginal sites is not higher compared to mantle- and core-sites, which could be connected with coarsening via GBAR during texture-annealing, reducing the grain surface free energy, which is lowest for round grains (chapter 2.1.2). Sample 1 and 6 show the highest elongation values for quartz and thus indicate a higher influence of strain; the elongation of sample 2 and 5 show the lowest elongation values and thus indicate a minor influence of strain or the influence of static recrystallization. Smaller variations of the grade of elongation could be caused by local strain and temperature differences. Thus, the strain distribution within the Yalgoo Dome might have been not homogeneously with higher strain rates only at the margin and lower strain rates in the center; high-strain sites also partly occur in more central parts of the Yalgoo Dome. This could be due to unequal strain partitioning into zones with different temperatures, mineral- and water-contents.

The mean long axis orientation is subparallel to the reference foliation for all samples, defining the individual foliation orientation. Higher standard deviations partly occur for quartz, feldspar and mica of marginal, mantle or core samples and do not reflect an overall trend along a margin-center profile within the Yalgoo Dome. Thus, they might also be influenced by different local conditions: lower strain intensities adjusting mineral grains, dynamic or static recrystallization mechanisms destroying a previous grain orientation, or maybe more than one deformation direction overprinted the granitoids and thus the grain elongation and an associated distinct grain orientation would be poorly defined. The misorientation between mica LAOs and quartz/feldspar LAOs of sample 155850 could indicate two different deformation events, and thus the inclined mean mica orientation could be a relic of an older foliation or maybe a sign of a younger deformation overprint.

4.3 Interpretation of Crystallographic Preferred Orientations

Regarding the high-temperature microstructures described so far, dominant X-maxima are expected for the CPO plots, as this c-axes position establishes with the onset of prism<c> slip during high grade metamorphic conditions at minimum 650°C (Passchier & Trouw, 1998; chapter 2.3.3). However, just two samples show dominant X-maxima: 155850 (mantle) and 155876 (core). These two samples have also been digitized and comprise the largest grain sizes of the eight samples of which a grain size analysis has been done; also in the n_o/α plot, these two samples represented the lowest n_o/α ratios, representing the highest temperatures and lowest strain rates. Some of the other core CPO patterns show larger opening angles indicating higher temperatures (Law, 2014 and references therein; chapter 2.3.3). In contrast, sample 155806 represents one of the highest n_o/α ratios within the n_o/α plot presented in chapter 3.2, and thus slightly lower temperatures and higher strain rates. This sample derives from a northeastern marginal site of the Yalgoo Dome, where all CPO patterns show clear dominant Z-maxima (300-400°C) with just weakly pronounced c-axes at Y-positions (400-650°C) (Passchier & Trouw, 1998; chapter 2.3.3). Thus, the approximate trend of increasing temperature towards the Yalgoo-core seems to be confirmed by the CPO data.

In general, the CPO patterns mostly show point maxima on different positions, yet they poorly show typical single girdles, which would develop at lower temperatures due to the activation of more than one slip system, caused by cohesion between grains (Lister, 1977) (Passchier & Trouw, 1998; chapter 2.3.3). Thus it can be concluded, that very low temperature deformation has not influenced the Yalgoo-Dome. In this context, the role of hydrolytic weakening should be considered, as water reduces cohesion along grain boundaries and hence enables the activation of single slip systems at distinct temperatures (Griggs, 1967; Blacic, 1975).

Nevertheless, despite high temperatures all over the Yalgoo-structure, the majority of all CPO's trends towards the Z-direction, yet contain components close to Y and X in form of "tails", additional weaker point maxima or an oblique position between Z- and X- reference axes. At this point, different factors that might have influenced the unexpected Yalgoo-CPO pattern are discussed.

Mechanisms influencing CPO data

CPO patterns are not only a function of temperature and additionally the whole deformation history, total strain and the presence of other minerals should be taken into account (Toy et al., 2008). The ideal c-axis fabrics shown above are mainly derived from experiments with monomineralic quartz aggregates. In shear zones, the CPO patterns mainly represent late-

stage deformation conditions and thus do not illustrate the whole deformation history. Nevertheless, the final c-axis distribution is also influenced by the non-random initial fabric (Brunel, 1980; Law, 1986*;* Toy et al., 2008). The established grain position and crystallographic orientation after a first deformation event may decide on the slip system being active during the next deformation event (Toy et al., 2008): a high-T fabric might be preserved if its associated prism<a> slip system would be reactivated during a low-T deformation, in case of very few grains with an appropriate orientation for basal<a> slip. This could be also possible the other way round. Moreover, the process of strain partitioning within a rock causing a domainial fabric should be considered (Peternell et al., 2010; Pauli et al., 1996). This heterogeneous deformation especially occurs in polymineralic rocks, like quartz-feldspar aggregates (Lister & Price, 1978). Thus, a mixture of many different fabrics represents the rock sample as a whole. For instance, oblique CPO patterns can evolve by combining one domain dominated by basal<a> slip (Zmax) and another domain dominated by prism<c> slip (Xmax). Furthermore, the CPO characteristic can also be influenced by deformation induced dynamic recrystallization of grains, which is explained in a chapter below. This mechanism may weaken the CPO via growth of new randomly orientated grains or it may strengthen the CPO via oriented grain growth or the removal of grains with a higher dislocation density and a certain orientation (Culshaw & Fyson, 1984; Passchier & Trouw, 1998, p.90). According to Carreras, J. et al. (1977), CPO patterns of mylonites are also influenced by folding processes. They explain that folding is a consequence of increasing strain and strain softening of the material related to a progressively stabilizing microfabric. There are two possibilities of fabric-modification via folding: 1) bulk-pseudo-passive rotation/ intracrystalline deformation leading to a rotation of the fabric around the Y axis of the reference frame and thus, the old pattern is weakened without modification of the microstructure. 2) the development of a strong new CPO fabric accumulating around the fold's axial plane (YZ plane) as consequence of directional grain elongation. Combining both types involving old and new fabric element, crossed girdles can evolve.

Considering these factors influencing the final CPO pattern, different explanations for the CPO patterns of the Yalgoo Dome are possible, comprising older and younger components. For instance, dominant Z maxima combined with weakly pronounced c-axes accumulations close to the Y and X direction could indicate that deformation started at higher temperatures leading to an arrangement of c-axis parallel X. During progressing cooling, deformation continued and thus, an arrangement of c-axes parallel Z established reflecting the latest stage of deformation. Another explanation could be the existence of more than one deformation event: firstly high-temperature-tectonics and subsequently a second deformation event like folding or shearing during low temperatures, finally leading to a rotation of the c-axes

towards the Z-direction. The asymmetry of nearly all CPO patterns and the partly stretched point maxima might additionally be influenced by shearing of the rock fabric.

The theory of a final low temperature event causing dominant Z-maxima is more probable compared to the inverse thermal history, as CPO pattern mainly reflect the latest stage of the deformation history, as mentioned above in this chapter. However, the opposite deformation history is not impossible: perhaps deformation of the granitoid rocks started at lower temperatures during initial states of vertical tectonics or during previous horizontal tectonics. After the low-temperature deformation and with increasing temperature during a heating event, possibly only a minor number of c-axes rotated towards an X-direction with the onset of prism<c> slip, as possibly just few grains had an adequate orientation for this high-temperature-slip system. Additionally, Grain Boundary Sliding (GBS) would be a dominant deformation mechanism during very high temperature deformation (Boullier & Gueguen, 1975), which would not at all influence previously established c-axes orientations and thus a low-T-pattern might be preserved.

Furthermore, strain partitioning, as described by Peternell et al. (2010), has probably also affected the CPO patterns of the Yalgoo Dome samples. Some samples represent the original host-granitoid gneiss, some represent younger veins and the chemical composition and mineral content is also not equal for all rock samples. Thus, the strain might be unequally allocated to quartz grains and other rock components. Another evidence for a domainial CPO fabric is the assumption of melt-present deformation in mantle and core sites of the dome structure, probably leading to strain partitioning into melt-rich zones. Having a look at some AVA-images, this process in indicated in form of different parts of the thin section tile comprising different dominating colors and hence different c-axes orientations (Fig. 40). This strain partitioning and unequal petrological compositions might be an explanation for the differing CPO patterns of the dome-core and the other unexpected CPO distributions.

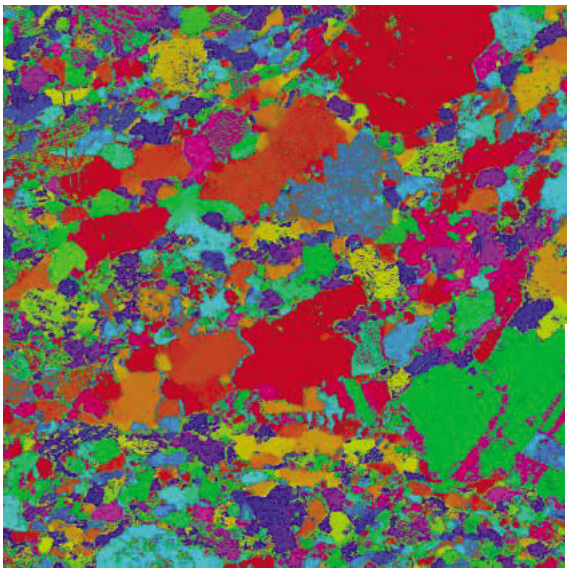

Fig. 40: Thin section AVA (5x5 mm) produce by the Fabric Analyser, showing the azimuth orientation of quartz c-axis; quartz ribbons comprise dominantly red colors and thus differ from the fine-grained parts, which show a remarkable component of blue, green, violet and minor red; different colors reflect different orientations.

4.4 Theory for the Yalgoo Dome evolution

Considering the microstructural information which has been discussed in chapter 4.1 to 4.3, the conclusion can be drawn that temperatures increase and strain rates decrease along a margin-mantle-core profile, considering peak-metamorphic conditions. The shear senses close to the marginal greenstone belt clearly indicate a granitoid-up/greenstone-down movement and thus indicate dominant vertical tectonics, as already proposed by Foley (1997). Additionally, the results of all three investigation methods (polarization-microscopy, Grain-Size-Analysis and Fabric Analyser techniques) comprise possible indicators for a younger lower-temperature deformation overprint affecting the dome structure.

These results can be well explained by the already established theory of diapirism and sagduction typically associated with archaic granitoid-greenstone-complexes, as discussed further below. In order to reveal the exact chronological deformation history of the Yalgoo Dome, further investigations are necessary. However, a rough evolution history is suggested here, based on the results of this thesis and the information gained from other research projects within the Murchison Domain, or from similar structures within other cratons:

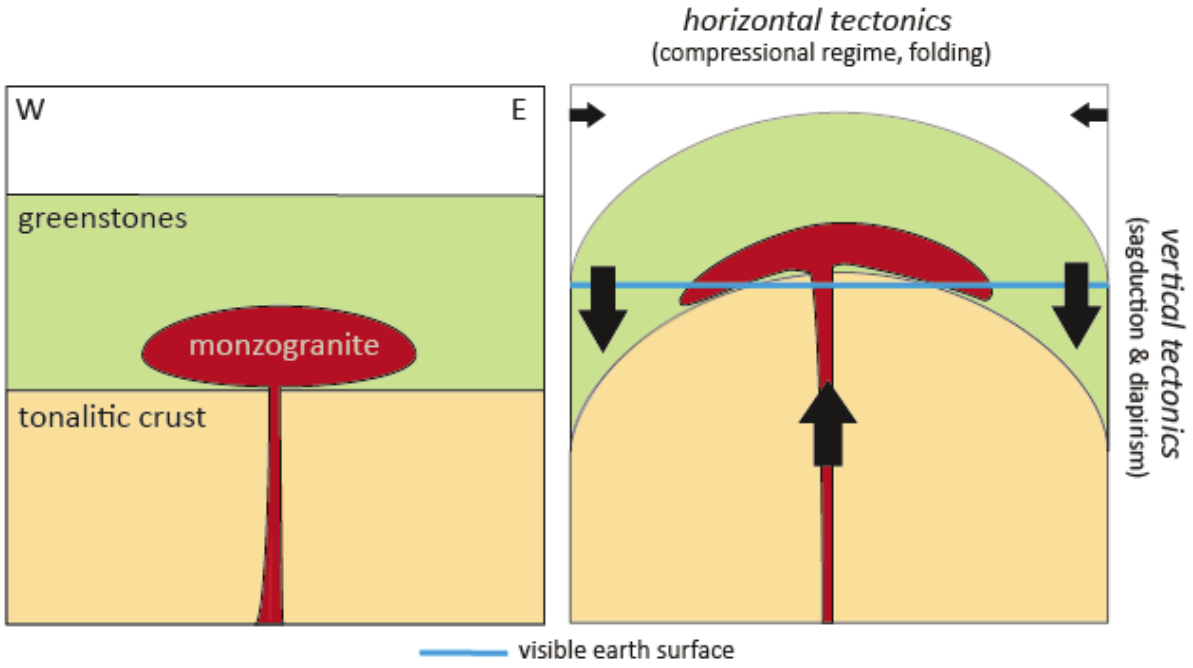

Fig. 41: Schematic profile showing the evolution models proposed for the Yalgoo Dome: dominant vertical tectonics (Foley, 1997) and possibly predating or postdating horizontal tectonics (Myers & Watkins, 1985; Fenwick,2014).

Younger monzogranite intruded into a 2.95 Ga old tonalite-greenstone crustal sequence at 2.65 Ga and hence during the latest stage of crustal reworking and mantle plume activity which has been proposed for the Youanmi Terrane (Ivanic et al., 2010; Ivanic et al., 2012). Syntectonic plutonism has been suggested for the Granite-Greenstone-Systems of the

Youanmi Terrane, to which the Yalgoo Dome belongs (Zibra, 2012), and thus, the monzogranite of the Yalgoo Dome might represent a syntectonic pluton. According to Ivanic et al. (2010), these heating events probably accompanied a period of crustal extension, which was postdated by collision and accretion tectonics. The intruding monzogranite has probably led to the first contact-metamorphic overprint of the greenstones. The archaic crust has been more tonalitic in contrast to the granitic crust of today, as the initial continental crust derived from partial melt of more mafic crustal rocks (chapter 1.1). The mechanisms of diapirism and sagduction followed (see chapter 1.1; Fig. 2), which were induced by gravity effects: less dense tonalitic crust raised and overlying denser greenstone layers sank. These simultaneous processes led to high-strain subvertical shear zones close to the contact areas of greenstones and granitoids. Combined advection into basins and domes probably led to a large thermal anomaly about 500°C (Thébaud & Rey, 2013), which would explain the presence of high-temperature metamorphic rocks within the whole Yalgoo Dome. The doming mechanism and accompanied crustal heating possibly led to partial melting of the central parts, where the heat accumulated, and to subsequent polydiapirism, which additionally involves the plutonic ascend of partial melt in the core, reinforcing the diapiric upwellig of a dome (Stephansson, 1975). Fenwick (2014) described the core of the Yalgoo Dome as a migmatite that possibly formed via fluid-induced partial melting of a tonalite-protolith, confirming the idea of polydiapirism. The results of this thesis also propose the highest temperatures for the dome-core. Extensional components like boudinage, which have been found in the field, would also accompany diapirism, affecting the up-doming and simultaneously extending part of the structure, as shown in figure 2. Spacious regional metamorphism combined with plutonism induced contact metamorphism overprinted the crust within the Yalgoo Dome, aggravating the differentiation between both metamorphic overprints in terms of chronological reconstruction of the deformation and thermal history. This 'regional contact metamorphism' is typical of Precambrian cratons (Okrusch & Matthes, 2009, p.394-395).

Eventually, folding during lower temperatures from the east and west overprinted the Yalgoo Dome after the doming process. The structure is located close to the suture zone between the Youanmi Terrane and the adjacent South-West Terrane (Fig. 3), for which collision tectonics are suggested (Dentith et al., 2000; Gee et al., 1986). This collision possibly caused a compressional regime from the west and east and hence folding in nearby areas could have been induced. The schematic section shown in figure 41 describes this theory of dominant vertical tectonics, accompanied by possibly subsequent horizontal tectonics. This second deformation event during low temperatures could explain the rotation of the c-axes towards the Z-direction. At least, one large scale fold within the core area is visible on an aeromagnetic map and the whole dome structures is elongated in the north-south direction and compressed along an east-west-profile. Moreover, smaller horizontal shear zones

transect the roundish Yalgoo Dome; one larger dextral transform fault in the core area is shown on figure 23. Thus, also shearing could have locally affected the crystallographic fabric. Perhaps, low-temperature horizontal tectonics predated the vertical geodynamics of the Yalgoo Dome and produced the initial CPO patterns with dominant Z-maxima, which are still visible as relic of an older deformation and were subsequently rotated or partly replaced by new weakly pronounced c-axes-orientations, as discussed in chapter 4.3.

The theory of Myers & Watkins (1985) involving solely fold interference shaping the Yalgoo Dome, would probably not lead to the temperature distributions with higher temperatures and lower strain rates in central areas and slightly lower temperatures and higher strain rates at marginal sites. Moreover, pure folding is not likely to cause these dominant high temperatures all over the Yalgoo Dome, mostly exceeding 500°C.

Other roundish, dome-like structures have been found in the Eastern Pilbara Craton. Van Kranendonk et al. (2004) also explained these geological phenomena with a combination of two types of diapirism: solid-state diapirism & magmatic diapirism. According to him, the former could be a consequence of ductile re-mobilization of the granitoid crust through its transposition to deeper crustal levels. Intensive basaltic volcanism would bury the felsic crust under denser mafic material leading to an inverted density profile and the rise of the lighter material. The magmatic diapirism implicates partial melting of the granitic crust that has been buried to higher depth, which is accompanied by beginning plutonism in the cores of granitic diapirs.

High temperature tectonics are typical of the Archean and probably led to the formation of the Yalgoo Dome. High-pressure tectonics leading to blueschist and eclogite facies have not been observed within the Yalgoo-structure and also not in the Yilgarn Craton, indicating that subduction played no role concerning the formation of these crustal parts (Gee et al., 1986). Nevertheless, Palin & White (2016) have shown that blueschist facies conditions existed during the Archean, yet archaic crust with relatively high Mg-contents and higher thermal gradients would not develop typical mineral assemblages indicating blueschist facies. Thus, the role of high-pressure tectonics should not be disposed for all archaic structures.

5 Conclusions

In summary, this thesis supports the theory of polydiapirism and sagduction shaping the Yalgoo Dome with its migmatic core and the surrounding narrow greenstone belt. These advection-mechanims of rising, less dense granitoids and sinking, denser greenstones produces subvertical shear zones at the granitoid-greenstone contact and would additionally provoke heating of the crust in the whole Yalgoo area (Thébaud & Rey, 2013), with heat accumulation in the tonalite core possibly leading to partial melting. The results of all analysis concerning grain shape, grain size and crystallographic preferred orientation reveal high temperature conditions between 400°C (upper greenschist facies) and possibly 800°C (lower granulite facies). The suggested temperature and strain distribution within the Yalgoo Dome indicates higher temperatures (> 500°C) and lower strain rates for the core area, with some samples from the core areas and the monzogranite mantle probably exceeding 650°C during peak metamorphic conditions. This can be concluded from increasing grain sizes towards the dome center, the occurrence of quartz - chessboard patterns in mainly central areas, intensified dynamic and static recrystallization microstructures, or from indicators for melt-present deformation, especially close to the tonalitic core of the Yalgoo Dome. The few crystallographic-preferred-orientation-patterns (CPOs) showing X-maxima and hence the activation of prism<c> slip at minimum 650°C, derive from samples of mantle and core areas. In contrast, marginal sites close to the greenstone belt are characterized by slightly lower temperatures (400-500°C) and higher strain rates. The presence of SC' shearbands close to the margin underlines the assumption of high-grade-shear zones nearby the greenstone belt. The determined shear senses in this granitoid-greenstone-contact-zone reveal dominant granitoid-up/greenstone-down kinematics, confirming the proposed simultaneously operating processes of diapirism and sagduction. However, the majority of CPO patterns shows dominant Z-maxima (basal<a> slip at about 300-400°C), and just minor c-axes accumulations in Y (>400°C) and X (>650°C) direction. As the CPO patterns mainly reflect the latest stage of the deformation history, these results could hint at a younger low-temperature deformation like folding overprinting the high-temperature-fabric and leading to the rotation of c-axes towards the Z direction.

Acknowledgment

At this point, I would like to express my gratitude to Dr. Mark Peternell of the Tectonophysics work group at the JGU Mainz, who always lent an ear to me when I came to him with many questions. Another 'thanks' goes to Ivan Zibra of the Geological Survey of Western Australia, who did the whole field work and primary assessments of the rock samples, on which my thesis is based. Moreover, I am indebted to Klemens Seelos, who took high-quality photos of chosen thin sections, which facilitated precise digitalization. Finally, I would like to thank all the other colleagues of the JGU Mainz, who tried to technically support my work. In this context, I particularly would like to mention Daniel Hammes, Jonas Köpping and Dr. Eric Salomon. Of course, I also appreciate the mental support by my family enabling my power of endurance.

Bibliography

Archibald, N.J. et al. (1978): The evolution of Archean greenstone terrains, Eastern Goldfields Province, Western Australia. Precambrian Res., vol. 6, 103-131.

Arculus, R.J. & Ruff, L.J. (1990): Genesis of Continental Crust: Evidence from Island Arcs, Granulites, and Exospheric Processes, Granulites and Crustal Evolution. NATO ASI Series, Springer, vol. 311, 7-23.

Barley, M.E. et al. (1989): Late Archean convergent margin tectonics and gold mineralization: A new look at the Norseman-Wiluna Belt, Western Australia. Geology, vol. 17 (9), 826-829.

Bell, T.H. & Hickey, K.A. (1999): Complex microstructures preserved in rocks with a simple matrix; significance for deformation and metamorphic processes. J. Metamorph. Geol., vol. 17 (5), 521-535.

Bickle, M.J. (1978): Heat Loss from the Earth: A constraint on Archean tectonics from the relation between geothermal gradients and the rate of plate production. Earth Planet. Sci. Lett., vol. 40, 301-315.

Blacic, J.D. (1975): Plastic-deformation mechanisms in quartz: the effect of water. Tectonophysics, vol. 27, 271-294.

Boullier, A.M. & Gueguen, Y. (1975): SP-Mylonites: origin of some mylonites by superplastic flow. Contrib. Mineral. Petrol., vol. 50 (2), 93-104.

Brunel, M. (1980): Quartz fabrics in shear zone mylonites: evidence for a major imprint due to late strain increments. Tectonophysics, vol. 64, T33-T44.

Campbell, I.H. & Hill, R.I. (1988): A two-stage model for the formation of the granite greenstone terrains of the Kalgoorlie-Norseman area, Western Australia. Earth Planet. Sci. Lett., vol. 90, 11-25.

Carreras, J. et al. (1977): The effects of folding on the c-axis fabrics of a quartz mylonite. Tectonophysics, vol. 39, 3-24.

Cashman, K.V. & Ferry, J.M. (1988): Crystal size distribution (CSD) in rocks and the kinetics and dynamics of crystallization, III., Metamorphic crystallization. Contrib. Mineral. Petrol., vol. 99, 401-415.

Champion, D.C. & Sheraton, J.W. (1997): Geochemistry and Nd isotope systematics of Archaean granites of the Eastern Goldfields, Yilgarn Craton, Australia: implications for crustal growth processes. Precambrian Res., vol. 83, 109-132.

Czarnota, K. et al. (2010): Geodynamics of the eastern Yilgarn Craton. Precambrian Res., vol. 183, 175–202.

Culshaw, N.G. & Fyson, W.K. (1984): Quartz ribbons in high grade granite gneiss: modifications of dynamically formed quartz c-axis preferred orientation by oriented grain growth. J. Struct. Geol., vol. 6 (6), 663-668.

Dentith, M.C. et al. (2000): Deep crustal structure in the southwestern Yilgarn Craton, Western Australia. Tectonophysics, vol. 325, 227–255.

Drummond, B.J. (1988): A review of crust/ upper mantle structure in the Precambrian areas of Australia and implications for Precambrian crustal evolution. Precambrian Res., vol. 40/41, 101-116.

Fenwick, M.J. (2014): Structural Evolution of the Yalgoo Dome, Yilgarn Craton, Western Australia: A Core Perspective. Bachelor Thesis, Geological Survey of Western Australia, Record 16, 93p.

Foley, B.J. (1997): Reassessment of Archaean tectonics in the Yalgoo District, Murchison Province, Western Australia. Geological Society of Australia - Abstracts, vol. 46, 23.

Gee, R.D. (1979): Structure and tectonic style of the Western Australian Shield. Tectonophysics, vol. 58, 327-369.

Gee, R.D. et al (1986): Relation between Archean high-grade gneiss and granite-greenstone terrain in Western Australia. Precambrian Res., vol. 33, 87-102.

Gleason, G.C. & Tullis, J. (1993): The role of dynamic recrystallization in the development of lattice preferred orientations in experimentally deformed quartz aggregates. J. Struct. Geol., vol. 15 (9/10), 1145-1168.

Griggs, D. (1967): Hydrolitic Weakening of Quartz and Other Silicates. Geophys. J. R. Astr. Soc., vol. 14, 19-31.

Herzberg, C. et al. (2010): Thermal history of the Earth and its petrological expression, Earth Planet. Sci. Lett., vol. 292, 79-88.

Higgins, M.D. (2006): Quantitative textural Measurements in Igneous and Metamorphic Petrology. Cambridge University Press.

Hirth, G. & Tullis, J. (1992): Dislocation creep regimes in quartz aggregates. J. Struct. Geol., vol. 14 (2), 145-159.

Ivanic, T.J. et al. (2010): Age and significance of voluminous mafic–ultramafic magmatic events in the Murchison Domain, Yilgarn Craton. Aust. J. Earth Sci., vol. 57 (5), 597-614.

Ivanic, T.J. et al. (2012): Zircon Lu–Hf isotopes and granite geochemistry of the Murchison Domain of the Yilgarn Craton: Evidence for reworking of Eoarchean crust during Meso-Neoarchean plume-driven magmatism. Lithos, vol. 148, 112–127.

Johnson, S.P. (2013): The birth of supercontinents and the Proterozoic assembly of Western Australia. Geological Survey of Western Australia, 78p.

Johnson, T.E. et al. (2014): Delamination and recycling of Archaean crust caused by gravitational instabilities. Nature Geosci., vol. 7, 47-52.

Kamber, B.S. (2015): The evolving nature of terrestrial crust from the Hadean, through the Archaean, into the Proterozoic. Precambrian Res., vol. 258, 48–82.

Korenaga, J. (2006): Archean Geodynamics and the Thermal Evolution of Earth. Geoph. Monog. Series, AGU Publications, vol. 164, 7-32.

Korenaga, J. (2008): Plate tectonics, flood basalts and the evolution of Earth's oceans. Terra Nova, vol. 20 (6), 419–439.

Korenaga, J. (2013): Initiation and Evolution of Plate Tectonics on Earth: Theories and Observations. Annu. Rev. Earth Planet. Sci., vol. 41, 117-51.

Kruhl, J.H. (1996): Prism- and basal-plane parallel subgrain boundaries in quartz: a microstructural geothermobarometer. J. Metamorph. Geol., vol. 14, 581-589.

Kruhl, J.H. (1998): Reply: Prism- and basal-plane parallel subgrain boundaries in quartz: a microstructural geothermobarometer. J. Metamorph. Petrol., vol. 16, 142-146.

Kusky, T.M. & Polat, A. (1999): Growth of granite–greenstone terranes at convergent margins, and stabilization of Archean cratons. Tectonophysics, vol. 305, 43–73.

Law, R.D. (1986): Relationships between strain and quartz crystallographic fabrics in the Roche Maurice quartzites of Plougastel, western Brittany. J. Struct. Geol., vol. 8 (5), 493-515.

Law, R.D. (2014): Deformation thermometry based on quartz c-axis fabrics and recrystallization microstructures: A review. J. Struct. Geol., vol. 66, 129-161.

Lexa, O. (2003a): Numerical Approaches in Structural and Microstructural Analyses. PhD thesis, Charles University, Prague.

Lexa, O. (2003b): PolyLX Toolbox for MATLAB - Reference Manual. Charles University, Prague, 2.0 edition.

Lister, G.S. & Hobbs, B.E. (1980): The simulation o! fabric development during plastic deformation and its application to quartzite: the influence of deformation history. J. Struct. Geol., vol. 2 (3), 355- 370.

Lister, G.S. & Price, G.P. (1978): Fabric development in a quartz-feldspar mylonite. Tectonophysics, vol. 49, 37-78.

Lloyd, G.E. & Freeman, B. (1991): SEM electron channelling analysis of dynamic recrystallization in a quartz grain. J. Struct. Geol., vol. 13. (8), 945-953.

Mainprice, D. et al. (1986): Dominant c-slip in naturally deformed quartz: Implications for dramatic plastic softening at high temperature. Geology, vol. 14, 819-822.

Marsh, B.D. (1988): Crystal size distribution (CSD) in rocks and the kinetics and dynamics of crystallization, I. Theory. Contrib. Mineral. Petrol., vol. 99, 277-291.

Martin, H. (1986): Effect of steeper Archean geothermal gradient on geochemistry of subduction-zone magmas. Geology, vol. 14 (9), 753-756.

Moyen, J.-F. & Martin, H. (2012): Forty years of TTG research. Lithos, vol. 148, 312–336.

Myers, J.S. (1990): Precambrian tectonic evolution of part of Gondwana, southwestern Australia. Geology, *vol. 18 (6), p. 537-540.*

Myers, J.S. (1993): Precambrian Tectonic History of the West Australian Craton and Adjacent Orogens. Annu. Rev. Earth Planet. Sci., vol. 21, 453-485.

Myers, J.S. & Watkins, K.P. (1985): Origin of granite-greenstone patterns, Yilgarn Block, Western Australia. Geology, vol. 13 (11), 778-780.

Okrusch, M. & Matthes, S. (2009):Mineralogie: Eine Einführung in die spezielle Mineralogie, Petrologie und Lagerstättenkunde. Springer, 8. Auflage.

Palin, R.M. & White, R. (2016): Emergence of blueschists on Earth linked to secular changes in oceanic crust composition. Nature Geosci., vol. 9, *60-64.*

Passchier, C.W. & Trouw, R.A.J. (1998): Microtectonics. Springer, 2.0 edition.

Pauli, C. et al. (1996): Fabric domains in quartz mylonites: localized three dimensional analysis of microstructure and texture. J. Struct. Geol., vol. 18 (10), 1183-1203.

Peternell, M. et al. (2009): A new approach to crystallographic orientation measurement for apatite fission track analysis: Effects of crystal morphology and implications for automation. Chem. Geol., vol. 265, 527–539.

Peternell, M. et al. (2010): Evaluating quartz crystallographic preferred orientations and the role of deformation partitioning using EBSD and fabric analyser techniques. J. Struct. Geol., vol. 32, 803-817.

Peterson, T.D. (1996): A refined technique for measuring crystal size distributions in thin section. Contrib. Mineral. Petrol., vol. 124, 395–405.

Pidgeon, R.T. & Wilde, S.A. (1990): The distribution of 3.0 Ga and 2.7 Ga volcanic episodes in the Yilgarn Craton of Western Australia. Precambrian Res., vol. 48, 309-325.

Roberts, N.M.W. et al. (2015): Continent Formation through Time. Geol. Soc. London Spec. Publ., vol. 389, 1–16.

Schmid, S.M. & Casey, M. (1986): Complete fabric analysis of some commonly observed quartz c-axis patterns. Geoph. Monog. Series, AGU Publications, vol. 36, 263-286.

Stein, M. & Hofmann, A.W. (1994): Mantle plumes and episodic crustal growth. Nature, vol. 372, 63-68.

Stephansson, O. (1975): Polydiapirism of granitic rocks in the Svecofennian of central Sweden. Precambrian Res., vol. 2, 189-214.

Stipp, M. et al. (2002): The eastern Tonale fault zone: a 'natural laboratory' for crystal plastic deformation of quartz over a temperature range from 250 to 700°C. J. Struct. Geol., vol. 24, 1861-1884.

Stipp, M. & Kunze, K. (2008): Dynamic recrystallization near the brittle-plastic transition in naturally and experimentally deformed quartz aggregates. Tectonophysics, vol. 448, 77-97.

Stipp, M. & Tullis, J. (2003): The recrystallized grain size piezometer for quartz. Geophys. Res. Lett., vol. 30 (21), 2088.

Swager, C.P. (1997): Tectono-stratigraphy of late Archaean greenstone terranes in the southern Eastern Goldfields, Western Australia. Precambrian Res., vol. 83, 11-42.

Thébaud, N. & Rey, P.F. (2013): Archean gravity-driven tectonics on hot and flooded continents: Controls on long-lived mineralised hydrothermal systems away from continental margins. Precambrian Res., vol. 229, 93–104.

Toy, V.G. et al. (2008): Quartz fabrics in the Alpine Fault mylonites: Influence of pre-existing preferred orientations on fabric development during progressive uplift. J. Struct. Geol., vol. 30, 602-621.

Tribe, I.R. & D'Lemos, R.S. (1996): Significance of a hiatus in down-temperature fabric development within syn-tectonic quartz diorite complexes, Channel Islands, UK. J. Geol. Soc., vol. 153, 127-138.

Tullis, J. (1977): Preferred orientation of quartz produced by slip during plane strain. Tectonophysics, vol. 39, 87-102.

Tullis, J. & Yund, R.A. (1985): Dynamic recrystallization of feldspar: A mechanism for ductile shear zone formation. Geology, vol. 13, 238-241.

Urai, J.L. et al. (1986): Dynamic Recrystallization of minerals, Mineral and rock deformation: laboratory studies. Geoph. Monog. Series, AGU Publications, vol. 36, 161-199.

Van Groos, A. F. K. & Heege, J. P. T. (1973): The High-Low Quartz Transition up to 10 Kilobars Pressure. J. Geol., vol. 81 (6), 717–724.

Van Kranendonk, M.J. et al. (2004): Critical tests of vertical vs. horizontal tectonic models for the Archaean East Pilbara Granite–Greenstone Terrane, Pilbara Craton, Western Australia. Precambrian Res., vol. 13, 173–211.

Van Kranendonk, M.J. et al. (2013): Long-lived, autochthonous development of the Archean Murchison Domain, and implications for Yilgarn Craton tectonics. Precambrian Res., vol. 229, 49–92.

Van Kranendonk, M.J. et al. (2015): Making it thick: a volcanic plateau origin of Palaeoarchean continental lithosphere of the Pilbara and Kaapvaal cratons. Geol. Soc. London Spec. Publ., vol. 389, 83–111.

Vernon, R.H. (2004): A Practical Guide to Rock Microstructure. Cambridge University Press.

Watkins, K.P. et al. (1991): Crustal evolution of Archaean granitoids in the Murchison Province, Western Australia. Precambrian Res., vol. 50, 311-336.

Wilde, S.A. et al. (2001): Evidence from detrital zircons for the existence of continental crust and oceanson the Earth 4.4 Gyr ago. Nature, vol. 409, 175-178.

Wilson, C.J.L. et al. (2003): The application of an automated fabric analyzer system to the textural evolution of folded ice layers in shear zones. Ann. Glaciol., vol. 37.

Wirth, R. & Voll, G. (1987): cellular intergrowth between quartz and sodium-rich plagioclase (myrmekite) – an analogue of discontinuous precipitation in metal alloys. J. Mater. Sci., vol. 22 (6), 1913-1918.

Zibra, I. et al. (2012): Shearing of magma along a high-grade shear zone: Evolution of microstructures during the transition from magmatic to solid-state flow. J. Struct. Geol., vol. 37, 150-160.

Zibra, I. et al. (2013): On shearing, magmatism and regional deformation in Neoarchean granite-greenstone systems: Insights from the Yilgarn Craton. J. Struct. Geol., vol. xxx, 1-15.

Appendix

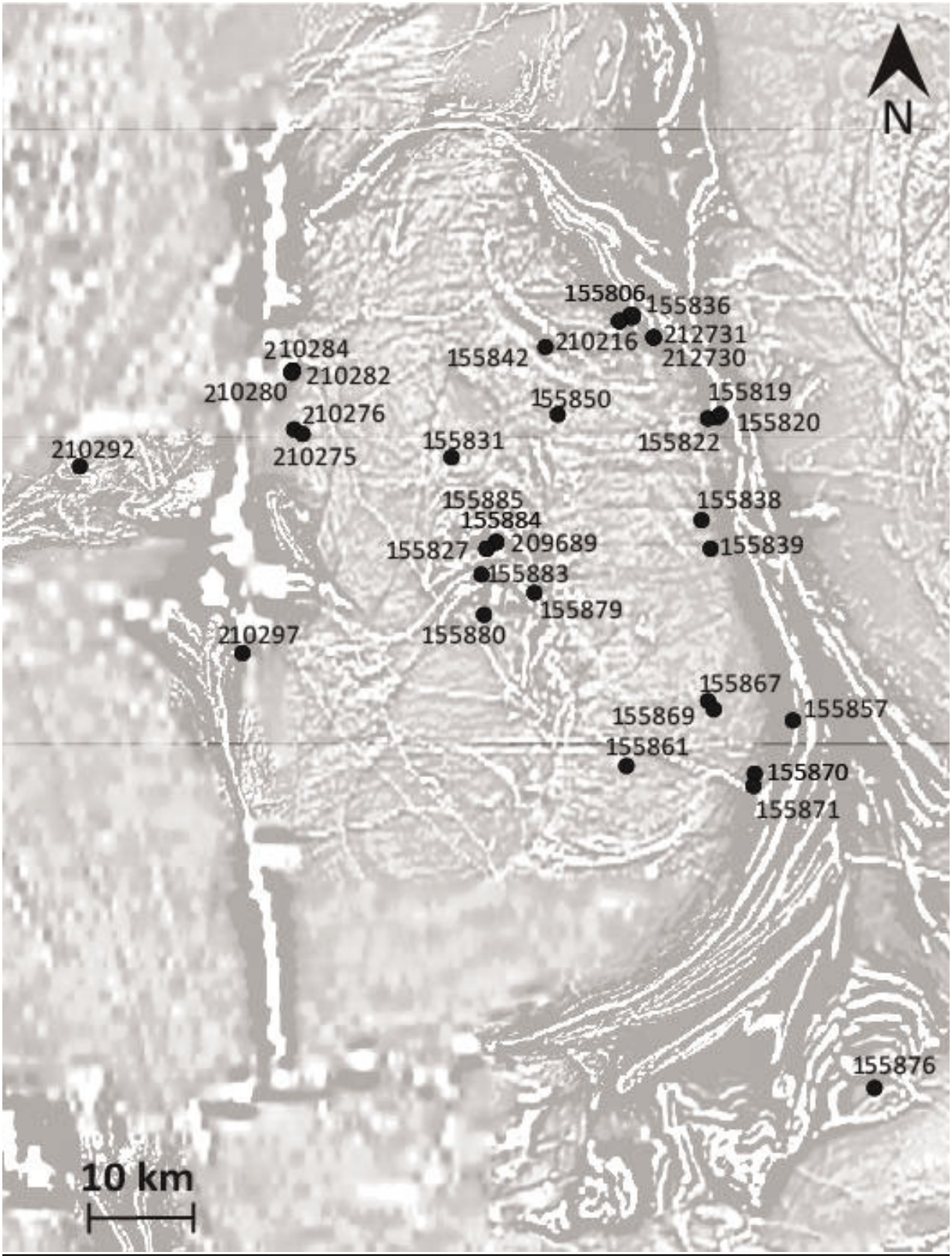

Fig. A1: Sample point locations within the Yalgoo Dome.

Table A1: Temperature and strain categories determined for all samples by thin section microscopy

Thin Section		Peak Metamorphic facies		Strain intensity
155806		Mid AF		high
155819		Lower-mid AF		high
155820		Upper AF-lower GF		low
155822		Lower-mid AF		high
155827		Upper AF-lower GF		low
155831		Mid AF		moderate
155836		Mid AF		moderate
155838		Upper AF		low
155839		Mid AF		low
155842		Upper AF-lower GF		moderate
155850		Upper AF-lower GF		high
155857		Mid AF		high
155861		Upper AF		moderate
155867		Mid-upper AF		moderate
155869		Upper AF-lower GF		low
155870		mid-upper AF		moderate
155871		Mid AF		low
155876		Upper AF-lowerGF		moderate
155879		Upper AF		low
155880		GF (magmatic)		undeformed
155883		Low-mid AF		moderate
155884		Upper AF-lowerGF		moderate
155885		Upper AF-lowerGF		low
209689		Upper AF		moderate
210216a		Mid AF		high
210216b		Mid AF		moderate
210275		Low-mid AF		moderate
210276		low-mid (epidote) AF		high
210277		Mid AF		moderate
210280		Mid AF		very high
210282		Upper gF-lower AF		low
210284		Low-mid AF		very high
210292		Mid AF		moderate
212297		Mid AF		high
212730		Low-mid AF		high
212731		Low-mid AF		high

medium-high T
high T
very high T

low strain
moderate strain
high strain

Table A2: Rotations applied to CPOs & digitized shapefiles in Matlab

Thin Section	Rotation [°] around 0°/90° (Y) axis *by Mona Schiller*	Rotation [°] around 0°/90° (Y) axis *by Ivan Zibra*	Rotation [°] around 0°/0° (Z) axis *by Ivan Zibra*	Rotation [°] around 90°/0° (X) axis *by Ivan Zibra*
155806	**12**			
155819	-4			30
155820	40			
155822	55			
155827	**-35**	70	20	
155831	-30	0		
155836	-30	50		
155850	**5**			
155861	10	0		
155867	**55**	90		
155869			90	
155870	20 (stereo32) **-70 (Matlab)**	25		
155876	**-23**	0		
155879	45	90	48	20
155880	-23	10		
155884	-10	20		
155885	20			
210216b	20			
210275	-47			
210276	60			
210277	15	20		
210280	-15	20		
210282	-45			
210284			20	
210292	-30	-45		
210297	17	0		
212730	-10	14		
212731	-10	11		

- green colored thin sections: CPO - reference foliation parallel short side of section
- all other samples in table: CPO - reference foliation parallel to the long side of section
- grey colored rotations around Y axis suggested by Ivan Zibra were not performed
- **bold** thin sections were digitized and analyzed with Matlab

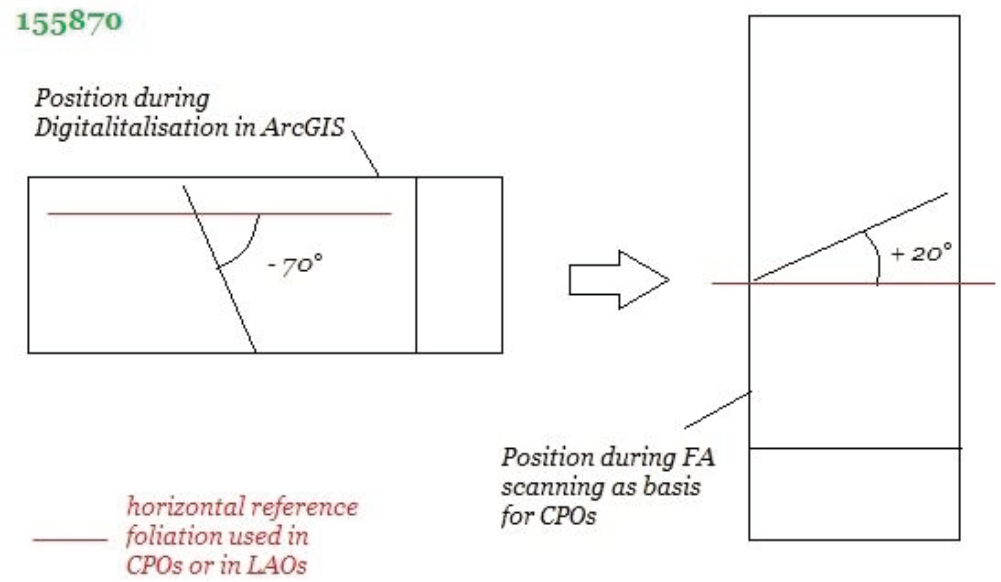

Fig. A2: Two different rotation angles for thin section 155870; left: rotation for Matlab results, right: rotation for CPO data

Table A3a: Mean values and standard deviations for different characteristics of eight digitized samples, derived from a polyLX Grain-Size-Analysis

	155806		**155827**		**155850**	
Phase	**Q**	**F**	**Q**	**F**	**Q**	**F**
Quantity	208	279	203	362	207	198
Area [*10^5 µm^2]						
Mean	0,963	2,899	4,644	4,347	8,001	8,327
Std	1,764	6,559	5,300	6,444	14,030	10,188
Fraction [%]	19,350	78,158	37,253	62,181	48,653	48,434
EAD [µm]						
Mean	273,461	433,982	655,096	607,094	758,389	876,409
Std	219,109	425,882	403,720	430,646	667,660	541,907
Length [µm]						
Mean	421,273	606,816	969,478	833,698	1237,829	1258,451
Std	351,801	586,309	660,711	571,212	1227,023	803,332
AxialRatio						
Mean	1,968	1,641	1,712	1,660	1,939	1,699
Std	1,258	0,448	0,698	1,270	0,850	0,542
Elongation						
Mean	2,563	2,088	2,230	2,152	2,583	2,159
Std	1,683	0,642	1,126	2,083	1,182	0,756
Roundness						
Mean	0,465	0,518	0,504	0,533	0,446	0,508
Std	0,160	0,138	0,146	0,148	0,155	0,142
Circularity						
Mean	0,514	0,549	0,545	0,563	0,477	0,546
Std	0,153	0,123	0,141	0,128	0,153	0,130
Orientation [°]						
Mean	83,918	84,154	110,413	93,799	87,806	89,158
Std	36,300	38,551	48,995	48,289	29,180	33,673
Prose_MD	80,33	83,20	141,62	111,40	87,13	89,11
Rotation	12	12	-35	-35	5	5
Prose_MD_rot	92,33	95,20	106,65	76,40	92,13	94,11
CSD						
α	171,438	300,646	315,409	305,767	494,786	510,432
n_0 [*10^{-11} mm^{-4}]	6,39	2,34	1,097	2,133	0,233	0,259

Table A3b: Mean values and standard deviations for different characteristics of eight digitized samples, derived from a polyLX Grain-Size-Analysis

	155867		**155870**		**155876**	
Phase	**Q**	**F**	**Q**	**F**	**Q**	**F**
Quantity	143	304	239	319	127	274
Area [*10^5 µm^2]						
Mean	1,680	3,836	0,887	1,352	11,067	4,979
Std	2,136	4,837	1,832	2,057	14,795	8,484
Fraction [%]	16,600	80,587	32,259	65,649	50,565	49,087
EAD [µm]						
Mean	394,414	604,770	278,949	361,401	956,401	631,548
Std	242,378	350,900	187,751	204,167	705,870	485,814
Length [µm]						
Mean	560,850	841,452	515,992	379,049	1452,982	905,410
Std	371,235	525,667	293,607	259,665	1188,368	743,866
AxialRatio						
Mean	1,607	1,539	1,548	1,592	1,728	1,631
Std	0,539	0,372	0,885	0,458	0,789	0,646
Elongation						
Mean	2,034	1,956	1,959	2,115	2,313	2,123
Std	0,834	0,515	1,492	0,689	1,356	1,044
Roundness						
Mean	0,537	0,543	0,568	0,513	0,496	0,526
Std	0,139	0,126	0,139	0,136	0,153	0,142
Circularity						
Mean	0,576	0,568	0,603	0,533	0,515	0,553
Std	0,133	0,116	0,132	0,119	0,152	0,139
Orientation [°]						
Mean	75,125	72,076	89,538	105,755	101,201	93,621
Std	52,264	52,771	57,856	58,012	39,503	38,839
Prose_MD	29,81	31,87	178,87	158,56	106,60	97,74
Rotation	55	55	-70	-70	-23	-23
Prose_MD_rot	84,81	86,87	108,87	88,56	83,60	74,74
CSD						
α	238,915	299,135	179,015	195,664	631,247	361,334
n_0 [*10^{-11} mm^{-4}]	1,870	2,966	7,187	12,722	0,115	0,846

Table A3c: Mean values and standard deviations for different characteristics of eight digitized samples, derived from a polyLX Grain-Size-Analysis

	210277		**210297**	
Phase	**Q**	**F**	**Q**	**F**
Quantity	146	373	171	339
Area [*10^5 µm^2]				
Mean	1,914	2,403	1,051	5,243
Std	1,809	5,119	1,185	36,596
Fraction [%]	23,513	75,422	9,134	90,321
EAD [µm]				
Mean	442,239	463,921	305,698	445,556
Std	220,164	301,693	201,534	685,876
Length [µm]				
Mean	673,388	663,502	453,550	610,226
Std	399,702	471,765	307,808	934,785
AxialRatio				
Mean	1,786	1,621	1,781	1,700
Std	0,579	0,526	0,636	0,866
Elongation				
Mean	2,288	2,076	2,228	2,080
Std	0,874	0,746	0,791	1,391
Roundness				
Mean	0,489	0,530	0,497	0,543
Std	0,152	0,149	0,155	0,146
Circularity				
Mean	0,534	0,564	0,555	0,600
Std	0,140	0,136	0,146	0,127
Orientation [°]				
Mean	88,614	83,824	90,026	85,256
Std	35,676	42,013	41,823	37,959
Prose_MD	90,61	81,88	85,33	84,67
Rotation	15	15	17	17
Prose_MD_rot	105,61	96,88	102,33	101,67
CSD				
α	219,466	215,592	211,669	327,784
n_0 [*10^{-11} mm^{-4}]	3,226	9,513	2,183	1,197

Matlab Script

```
% imread shapefile
clear all, close all, clc
filepath='\\fs02\mschille$\Dokumente\BA\Plots\';
datacell=cell(8,1);

datacell{1,1} = shpread;   % 155806
datacell{2,1} = shpread;   % 155827
datacell{3,1} = shpread;   % 155850
datacell{4,1} = shpread;   % 155867
datacell{5,1} = shpread;   % 155870
datacell{6,1} = shpread;   % 155876
datacell{7,1} = shpread;   % 210277
datacell{8,1} = shpread;   % 210297

% print initial overview-statistics of all 8 samples
% rotation of index i from 1 to 8
%{
data=datacell{i,1};
    totalarea=garea(data); txtwrite(totalarea,'Total Area Fraction.txt')
    dsc_area=describe(data); txtwrite(dsc_area,'Area.txt')
    dsc_length=describe(data); txtwrite(dsc_length,'Length.txt')
    dsc_orient=describe(data); txtwrite(dsc_orient,'Orientation.txt')
    dsc_axialratio=describe(data); txtwrite(dsc_axialratio,'AxialRatio.txt')
    dsc_elong=describe(data); txtwrite(dsc_elong,'Elongation.txt')
    dsc_round=describe(data); txtwrite(dsc_round,'Roundness.txt')
    dsc_circ=describe(data); txtwrite(dsc_circ,'Circularity.txt')
    dsc_EAD=describe(data); txtwrite(dsc_EAD,'Equal Area Diameter.txt')
%}
% call "Auswertung.m" script
Auswertung_mit_Plots

% Analysis and Plots of digitized thin sections
for i=1:8
    index=num2str(i);data=datacell{i,1};

%% Area fraction
f=figure;
for i=1:8
    data=datacell{i,1};
    areaQ_sum=sum(get(data('Q'),'Area'));
    areaF_sum=sum(get(data('F'),'Area'));
    area_ratio=(areaQ_sum)/(areaF_sum);

    plot(i,area_ratio,'.');
    axis([0 9 0 1.2]), Ticks = 0:1:9; set(gca, 'XTick', Ticks);
```

```
    title('Ratio of area fractions')
    xlabel('Sample Index'), ylabel('areaQ/areaF')

    if i==8
        break
    elseif i<8
        hold on
    end
end
print(f,'-depsc',strcat(filepath,'AreaQF_Ratio.eps')), close(gcf)

%% EAD
% Quartz
    EAD_Q = get(data('Q'),'EAD'); EADm_Q = mean(EAD_Q); std_EAD_Q = std(EAD_Q);
% subplot_Q
    Mean_x=[EADm_Q EADm_Q]; Mean_y=[0 70];
    f=figure; subplot(2,1,1);phist(EAD_Q), hold on, plot(Mean_x,Mean_y,'r')
    axis([0 3000 0 70]), xlabel('EAD of Quartz grains [microns]'), ylabel('%')
    hold off
% Feldspar
    EAD_F = get(data('F'),'EAD'); EADm_F = mean(EAD_F); std_EAD_F = std(EAD_F);
% subplot_F
    Mean_x=[EADm_F EADm_F];
    subplot(2,1,2); phist(EAD_F), hold on, plot(Mean_x,Mean_y,'r')
    axis([0 3000 0 70]), xlabel('EAD of Feldspar grains [microns]'), ylabel('%')
    hold off
    print(f,'-depsc',strcat(filepath,'Hist_EAD',index,'.eps')), close(gcf)

%% Long Axial Orientation (LAO) - rotated
% Rotations in [°], derived from foliation visible in thin sections
% pos~clockwise, neg~counterclockwise
    R=[12 -35 5 55 -70 -23 15 17];
% Quartz
    [~,~,lao_Q,sao_Q] = aorten(data('Q'));
    lao_Q_rot = lao_Q + R(i);
% subplot_Q
    f=figure; subplot(3,1,1); prose(lao_Q_rot), xlabel('Quartz')
% Feldspar
    [~,~,lao_F,sao_F] = aorten(data('F'));
    lao_F_rot = lao_F + R(i);
% subplot_F
    subplot(3,1,2); prose(lao_F_rot), xlabel('Feldspar')
% Mica
    [~,~,lao_M,sao_M] = aorten(data('M'));
    lao_M_rot = lao_M + R(i);
% subplot_M
    subplot(3,1,3); prose(lao_M_rot), xlabel('Mica')
```

```
    print(f,'-depsc',strcat(filepath,'Rose_LAO_rot',index,'.eps')), close(gcf)
end

% Extra Plots: Sample-Index versus Mean-value of each of 8 thin sections to be able
to compare the samples from the margin to the center
clear all, close all, clc
filepath='\\fs02\mschille$\Dokumente\BA\Plots\Profile\Rand-Zentrum\';
datacell=cell(8,1);

% repeated data-import, now ordered(Margin->Center)
% Margin (monzogranite mantle close to greenstone belt)
datacell{1,1} = shpread;    % 155806(NE)
datacell{2,1} = shpread;    % 155870(SE)
datacell{3,1} = shpread;    % 210277(NW)
datacell{4,1} = shpread;    % 210297(W)
% between (monzogranite mantle)
datacell{5,1} = shpread;    % 155867(SE)
datacell{6,1} = shpread;    % 155850(N)
% Center (magmatic, tonalite core)
datacell{7,1} = shpread;    % 155827
datacell{8,1} = shpread;    % 155876(S)


%% EAD
% EAD_Q
f=figure;
for i=1:8
    data=datacell{i,1};
    EADm_Q=mean(get(data('Q'),'EAD'));
    subplot(1,2,1); plot(i,EADm_Q,'.')
    axis([0 9 0 1100]); Ticks = 0:1:9; set(gca,'XTick',Ticks);
    title('Mean EAD of 8 Samples (Quartz)')
    xlabel('Sample Index'), ylabel('Mean EAD [microns]')
    if i==8
        break
    elseif i<8
        hold on
    end
end
% EAD_F
for i=1:8
    data=datacell{i,1};
    EADm_F=mean(get(data('F'),'EAD'));
    subplot(1,2,2); plot(i,EADm_F,'.')
    axis([0 9 0 1100]); Ticks = 0:1:9; set(gca,'XTick',Ticks);
    title('Mean EAD of 8 Samples (Feldspar)')
```

```
    xlabel('Sample Index'), ylabel('Mean EAD [microns]')
    if i==8
        break
    elseif i<8
        hold on
    end
end
print(f,'-depsc',strcat(filepath,'Mean_EAD.eps')), close(gcf)

%% Elongation
% Elong_Q
f=figure;
for i=1:8
    data=datacell{i,1};
    elongm_Q=mean(get(data('Q'),'Elongation'));
    subplot(1,2,1); plot(i,elongm_Q,'.')
    axis([0 9 1 3]); Ticks = 0:1:9; set(gca,'XTick',Ticks);
    title('Mean Elongation of 8 Samples (Quartz)')
    xlabel('Sample Index'), ylabel('Mean Elongation')
    if i==8
        break
    elseif i<8
        hold on
    end
end
% Elong_F
for i=1:8
    data=datacell{i,1};
    elongm_F=mean(get(data('F'),'Elongation'));
    subplot(1,2,2); plot(i,elongm_F,'.')
    axis([0 9 1 3]); Ticks = 0:1:9; set(gca,'XTick',Ticks);
    title('Mean Elongation of 8 Samples (Feldspar)')
    xlabel('Sample Index'), ylabel('Mean Elongation')
    if i==8
        break
    elseif i<8
        hold on
    end
end
print(f,'-depsc',strcat(filepath,'Mean_Elong.eps')), close(gcf)

%% Roundness
% Round_Q
f=figure;
for i=1:8
    data=datacell{i,1};
```

```
    roundm_Q=mean(get(data('Q'),'Roundness'));
    subplot(1,2,1); plot(i,roundm_Q,'.')
    axis([0 9 0 1]); Ticks = 0:1:9; set(gca,'XTick',Ticks);
    title('Mean Roundness of 8 Samples (Quartz)')
    xlabel('Sample Index'), ylabel('Mean Roundness')
    if i==8
        break
    elseif i<8
        hold on
    end
end
% Round_F
for i=1:8
    data=datacell{i,1};
    roundm_F=mean(get(data('F'),'Roundness'));
    subplot(1,2,2); plot(i,roundm_F,'.')
    axis([0 9 0 1]); Ticks = 0:1:9; set(gca,'XTick',Ticks);
    title('Mean Roundness of 8 Samples (Feldspar)')
    xlabel('Sample Index'), ylabel('Mean Roundness')
    if i==8
        break
    elseif i<8
        hold on
    end
end
print(f,'-depsc',strcat(filepath,'Mean_Round.eps')), close(gcf)

%% Orientation(rotated)

% md= mean direction, calculated via Lexa's prose-function, based on the
  results of the LAO-calculation via the aorten-function
% Rotations in [°], derived from foliation in thin sections
% pos~clockwise, neg~counterclockwise
R=[12 -70 15 17 55 5 -35 -23];
md_rot = zeros(8,2);
Index=1:8
% LAO_Q
for i=1:8
    data=datacell{i,1};
    [~,~,lao_Q,sao_Q] = aorten(data('Q'));
    lao_Q_rot = lao_Q + R(i);
        [md_Q_rot] = prose(lao_Q_rot); close(gcf);
            md_Q_rot = md_Q_rot(1);
                md_rot(i,1)= md_Q_rot;
    if i==8
        break
```

```
    end
end
% LAO_F
for i=1:8
    data=datacell{i,1};
    [~,~,lao_F,sao_F] = aorten(data('F'));
    lao_F_rot = lao_F + R(i);
        [md_F_rot] = prose(lao_F_rot); close(gcf);
            md_F_rot = md_F_rot(1);
                md_rot(i,2)= md_F_rot;
    if i==8
        break
    end
end

f=figure;
subplot(1,2,1); plot(Index,md_rot(:,1),'.')
axis([0 9 0 180]); Ticks = 0:1:9; set(gca, 'XTick', Ticks);
title('MD_prose(Quartz)'), xlabel('Sample Index'), ylabel('Mean Orientation [°]')
subplot(1,2,2); plot(Index,md_rot(:,2),'.')
axis([0 9 0 180]); Ticks = 0:1:9; set(gca, 'XTick', Ticks);
title('MD_prose (Feldspar)'), xlabel('Sample Index'), ylabel('Mean Orientation
[°]')

txtwrite(md_rot,'MD_rot.txt');
print(f,'-depsc',strcat(filepath,'MD_rot.eps'))
close(gcf)

%% CSD (alpha = slope, growth rate multiplied by time: G*t, n0 = intercept,
nucleation density [µm])
% tomm=0.001 converting result into µm, S=1.269 as scale factor related with
sphere-like objects
% chosing all phases as input, then chose one special phase from list, in order to
better estimate the grain number/Area
% --> Peterson, 1996
% define CSD matrix, in which alpha and n0 values can be saved
CSD_alpha = zeros(8,2);
CSD_n0 = zeros(8,2);
for i=1:8
    data=datacell{i,1};
    % Quartz
    [alpha_Q,n0_Q] = pcsd(data,'tomm=0.001','S=1.269');close(gcf)
    % Feldspar
    [alpha_F,n0_F] = pcsd(data,'tomm=0.001','S=1.269');close(gcf)
    % CSD-Matrix mit alpha- & n0- Werten auffüllen
    CSD_alpha(i,1)= alpha_Q; CSD_alpha(i,2)= alpha_F;
```

```
    CSD_n0(i,1)= n0_Q; CSD_n0(i,2)= n0_F;
    if i==8
        break
    elseif i<8
        hold on
    end
end
txtwrite(CSD_alpha,'CSD_alpha.txt'); txtwrite(CSD_n0,'CSD_no.txt');

% plotten alpha/index & n0/index
index=1:8;
f=figure;
% Quartz
% alpha
    subplot(2,2,1); plot(index,CSD_alpha(:,1),'.')
    axis([0 9 0 650]); Ticks = 0:1:9; set(gca,'XTick',Ticks);
    title('Alpha (8 Qtz-Samples)')
    xlabel('Sample Index'), ylabel('alpha')
% n0
    subplot(2,2,2); plot(index,CSD_n0(:,1),'.')
    axis([0 9 0 15e-11]); Ticks = 0:1:9; set(gca,'XTick',Ticks);
    title('n0 (8 Qtz-Samples)')
    xlabel('Sample Index'), ylabel('n0')
% Feldspar
% alpha
    subplot(2,2,3); plot(index,CSD_alpha(:,2),'.')
    axis([0 9 0 650]); Ticks = 0:1:9; set(gca,'XTick',Ticks);
    title('Alpha (8 Fsp-Samples)')
    xlabel('Sample Index'), ylabel('alpha')
% n0
    subplot(2,2,4); plot(index,CSD_n0(:,2),'.')
    axis([0 9 0 15e-11]); Ticks = 0:1:9; set(gca,'XTick',Ticks);
    title('n0 (8 Fsp-Samples)')
    xlabel('Sample Index'), ylabel('n0')
print(f,'-depsc',strcat(filepath,'alpha&n0_new.eps')), close(gcf)

% plotting n0/alpha (-> Lexa, 2003)
f=figure;
% Quartz
    subplot(1,2,1); plot(CSD_alpha(:,1),CSD_n0(:,1),'.')
    axis([0 800 0 14e-11 ]), title('CSD of Quartz'), xlabel('alpha=Gt'),
ylabel('n0')
    % Feldspar
    subplot(1,2,2); plot(CSD_alpha(:,2),CSD_n0(:,2),'.')
    axis([0 800 0 14e-11]), title('CSD of Feldspar'), xlabel('alpha=Gt'),
ylabel('n0') print(f,'-depsc',strcat(filepath,'CSD.eps')), close(gcf)
```

RECORD 2016/5

MICROSTRUCTURAL EVOLUTION OF THE YALGOO DOME (WESTERN AUSTRALIA)

Schiller

This Record is published in digital format (PDF) and is available as a free download from the DMP website at <www.dmp.wa.gov.au/GSWApublications>.

Further details of geological products produced by the Geological Survey of Western Australia can be obtained by contacting:

Information Centre
Department of Mines and Petroleum
100 Plain Street
EAST PERTH WESTERN AUSTRALIA 6004
Phone: +61 8 9222 3459 Fax: +61 8 9222 3444
www.dmp.wa.gov.au/GSWApublications